

**MOF-DERIVED METAL CHALCOGENIDE
NANOSTRUCTURED MATERIALS AS
ELECTROCATALYSTS FOR WATER SPLITTING
IN ELECTROCHEMICAL ENERGY CONVERSION**

By

Nachiketa Sahu

CHEM11201804016

**National Institute of Science Education and Research (NISER),
Jatani, Khurda, Odisha-752050**

*A thesis submitted to the
Board of Studies in Chemical Sciences*

*In partial fulfillment of
requirements for the Degree of*

**DOCTOR OF PHILOSOPHY
of
HOMI BHABHA NATIONAL INSTITUTE**



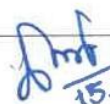
July, 2023

Homi Bhabha National Institute¹

Recommendations of the Viva Voce Committee

As members of the Viva Voce Committee, we certify that we have read the dissertation prepared by Nachiketa Sahu entitled "MOF-derived metal chalcogenide nanostructured materials as electrocatalysts for water splitting in electrochemical energy conversion" and recommend that it may be accepted as fulfilling the thesis requirement for the award of Degree of Doctor of Philosophy.

Chairman - Name & Signature with date Prof. A. Srinivasan


15.11.23

Guide / Convener - Name & Signature with date Dr. Jogendra Nath Behera

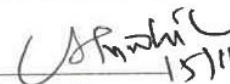

15-11-2023

Co-guide - Name & Signature with date (if any)

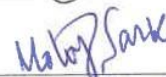
Examiner - Name & Signature with date Prof. Paritosh Mohanty


15-11-2023

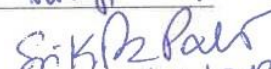
Member 1- Name & Signature with date Dr. Chandra Shekhar Purohit


15/11/23

Member 2- Name & Signature with date Dr. Moloy Sarkar


15.11.23

Member 3- Name & Signature with date Dr. Srikanta Patra


15/11/2023

Final approval and acceptance of this thesis is contingent upon the candidate's submission of the final copies of the thesis to HBNI.

I/We hereby certify that I/we have read this thesis prepared under my/our direction and recommend that it may be accepted as fulfilling the thesis requirement.

Date: 15-11-2023

Place: NISER Signature

Co-guide (if any)


Signature

Guide

¹ This page is to be included only for final submission after successful completion of viva voce.

STATEMENT BY AUTHOR

This dissertation has been submitted in partial fulfillment of requirements for an advanced degree at Homi Bhabha National Institute (HBNI) and is deposited in the library to be made available to borrowers under rules of the HBNI.

Brief quotations from this dissertation are allowable without special permission, provided that accurate acknowledgement of source is made. Requests for permission for extended quotation from or reproduction of this manuscript in whole or in part may be granted by the Competent Authority of HBNI when in his or her judgment the proposed use of the material is in the interests of scholarship. In all other instances, however, permission must be obtained from the author.

Nachiketa Sahu

Name & Signature of the student

DECLARATION

I, hereby declare that the investigation presented in the thesis has been carried out by me. The work is original and has not been submitted earlier as a whole or in part for a degree / diploma at this or any other Institution / University.

Nachiketa Sahu

Name & Signature of the student

LIST OF PUBLICATIONS

Published

1. Metal–organic framework (MOF) derived flower-shaped CoSe₂ nanoplates as a superior bifunctional electrocatalyst for both oxygen and hydrogen evolution reactions, **Nachiketa Sahu**, Jiban K. Das, J. N. Behera, *Sustainable Energy & Fuels*, 2021, **5**, 4992–5000.
2. NiSe₂ nanoparticles encapsulated in N-doped carbon matrix derived from a one-dimensional Ni-MOF: an efficient and sustained electrocatalyst for hydrogen evolution reaction, **Nachiketa Sahu**, Jiban K. Das, J. N. Behera, *Inorg. Chem.*, 2022, **61**, 2835–2845.
3. Metal–organic framework (MOF)-derived plate-shaped CoS_{1.097} nanoparticles for an improved hydrogen evolution reaction, **Nachiketa Sahu**, Jiban K. Das, J. N. Behera, *Dalton Trans.*, 2022, **51**, 10272–10278.
4. MOF-Derived Co₃S₄ nanoparticles embedded in nitrogen-doped carbon for electrochemical oxygen production, **Nachiketa Sahu**, J. N. Behera, *ACS Appl. Nano Mater.*, 2023, **6**, 7686-7693.
5. Prussian blue analogue (PBA) derived cobalt telluride nano-granules: an efficient catalyst for energy conversion and storage, Rajat K. Tripathy, Abhisek Padhy, **Nachiketa Sahu**, J. N. Behera, *Sustainable Energy & Fuels*, 2022, **6**, 4146-4152.
6. A phase-engineered nickel sulfide and phosphide (NiS-Ni₂P) heterostructure for enhanced hydrogen evolution performance supported with DFT analysis, Jiban K. Das, **Nachiketa Sahu**, Pratap Mane, Brahmananda Chakraborty, J. N. Behera, *Sustainable Energy & Fuels*, 2023,**7**, 4110-4119.

CONFERENCES

1. **Presented** a virtual **poster** at **Catalysis science and technology 10th anniversary** symposium 2021 organized by RSC during November 16 - 17, 2021.
2. **Participated and presented a poster** at the **ACS CRSI poster session** of 27th CRSI-National Symposium Chemistry organized by IISER, Kolkata during **September 26 – 29, 2021.**
3. **Participated and presented a virtual poster** on **Recent Advances in Catalysis Science and Engineering (RACSE)** at 27th International Conference of International Academy of Physical Sciences organized by NIT Jamshedpur during **October 26 - 28, 2021.**

Nachiketa Sahu

Name & Signature of the student

**Dedicated to
(My Family)**

ACKNOWLEDGEMENTS

I would like to thank **my supervisor Dr. Jogendra Nath Behera**, for his unwavering support, encouragement, patience and freedom provided for free thinking.

I am thankful to **Prof. Hirendra Nath Ghosh** (Director-NISER), **Prof. Sudhakar Panda** (Former Director-NISER), for the laboratory facilities and financial support.

I thank my Doctoral committee members, **Prof. A. Srinivasan, Dr. C. S. Purohit, Dr. Moloy Sarkar, Dr. Srikanta Patra** and all the faculty members in SCS.

I warmly thank our collaborator, **Dr. Brahmananda Chakraborty** (BARC).

I would like to thank all my past and present lab members, Dr. Ranjay K. Tiwari, Dr. Aneeya K. Samantara, Dr. Jiban K. Das, Dr. Rajat K. Tripathy, Dr. Malaya K. Sahoo, Dr. Abhisek Padhy, Manisha, Kismat, Litun, Ankita, Pratik, Prayash, Satya, Ashutosh and Ashish for their continuous support and valuable discussion.

I thank all my friends for their scientific discussions and moral support.

Above all, I want to express my gratitude to my beloved family members for their support and care during this difficult but wonderful journey.

Nachiketa Sahu

CONTENTS

Sl. No.	Titles	Page No.
1	Recommendations of the Viva Voce Committee	i
2	Statement by Author	ii
3	Declaration	iii
4	List of Publication	iv
5	Conferences	v
6	Dedication	vi
7	Acknowledgements	vii
8	Contents	viii
9	Motivation and Objective	ix
10	Synopsis	x
11	List of Schemes	xvii
12	List of Figures	xviii
13	List of Tables	xxi
14	List of Abbreviation	xxii
15	Chapter 1	1-34
16	Chapter 2	35-60
17	Chapter 3	61-89
18	Chapter 4	90-118
19	Chapter 5	119-148
20	Summary and Future Scope	149-150

MOTIVATION AND OBJECTIVE

As the environment deteriorates and the energy problem deepens, experts are looking for clean energy solutions that maintain a carbon-free atmosphere in contrast to conventional fossil fuels. The water splitting system with electrocatalysis provides an improved pathway for the synthesis of energy fuels like hydrogen. Electrocatalytic water splitting is a safe technology where the half-cell anodic and cathodic processes represent the oxygen evolution reaction (OER) and hydrogen evolution reaction (HER), respectively. The multiple steps involved in the electron coupling or decoupling process cause the water-splitting reaction to operate very slowly. Therefore, it is essential to employ promising electrocatalysts in order to decrease the needed overpotential and overcome all of these kinetic barriers in the electrolytic medium. IrO₂ and RuO₂ are commonly employed for oxygen evolution, whereas Pt-based electrocatalysts are now the best materials for hydrogen evolution. However, due to their high cost and restricted availability, these precious metals have limited uses. Therefore, it is necessary to decrease the usage of well-known noble metals and to create inexpensive, durable electrocatalysts that may operate catalytically just as effectively as valuable metals. Metal-organic frameworks, or MOFs, are regarded as a good sacrificial template for creating different kinds of functional materials for electrochemical energy conversion applications. These considerations drive my research attempt to create effective chalcogenide-based electroactive materials derived from MOFs that can serve as a good replacement for electrocatalysts based on noble metals for oxygen and hydrogen evolution reactions.

SYNOPSIS

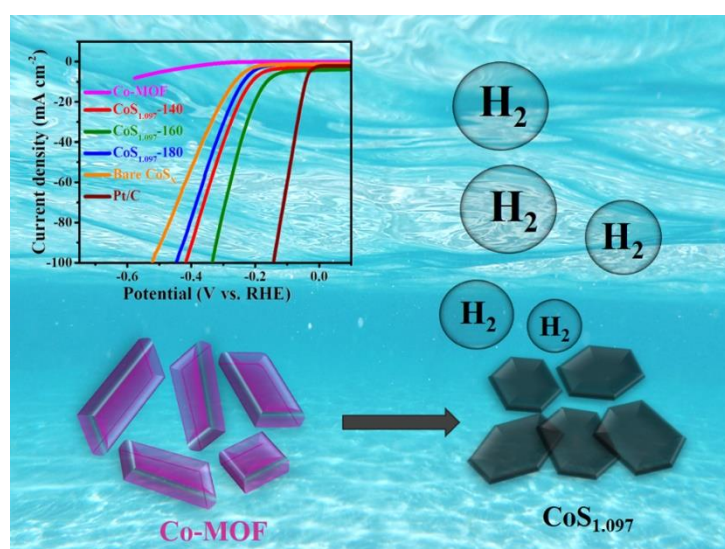
This present thesis involves the use of metal-organic framework (MOF)-derived metal chalcogenide materials for electrochemical energy conversion applications. The thesis composed of five chapters. **Chapter 1:** Includes the introduction part where the motivation for the search of alternative electrocatalyst towards electrochemical energy conversion application is explained. Additionally, the basic characterization techniques of the freshly prepared electrocatalyst and the basic electrochemical parameters for energy conversion application are also explained. **Chapter 2:** Illustrates the detailed study on MOF-derived $\text{CoS}_{1.097}$ nanoparticles as an efficient electrocatalyst for hydrogen evolution reaction. **Chapter 3:** Demonstrates designing of MOF-derived Co_3S_4 nanoparticles embedded in N-doped carbon and its electrochemical application towards oxygen evolution reaction. **Chapter 4:** Represents the synthesis of MOF-derived flower-like CoSe_2 nanoplates and its bifunctional activity towards oxygen and hydrogen evolution reactions. **Chapter 5:** Deals with the synthesis of MOF-derived NiSe_2 nanoparticles encapsulated in nitrogen-doped carbon matrix and its electrochemical performance for hydrogen evolution reaction.

Chapter 1: Introduction

The increasing energy crisis and environmental pollution motivate researchers towards alternative clean energy techniques that maintain a carbon-free environment compared to traditional fossil fuels. Electrocatalytic water splitting system offers a better pathway for producing energy fuels such as hydrogen and oxygen with naught carbon emission as the byproducts. This chapter throws light on the electrochemical energy conversion process, that basically consists of the two half-cell reactions. One is cathodic hydrogen evolution reaction (HER) and other one is anodic oxygen evolution reaction (OER).

However, the main obstacle in the conversion of water to O_2 and H_2 is the additional potential (overpotential) required to surpass the kinetic barrier for the splitting of water molecule. Therefore, it is desirable to develop cost-effective, durable and efficient electrocatalyst that can effectively catalyze HER and OER with a lower value of overpotential. The fundamental working principles, the mechanism of the respective half-cell reactions, advantages of several non-precious metal-based materials as electrocatalysts to carry out HER and OER over the precious ones are highlighted in this chapter. Additionally, the benefit of using metal-organic framework (MOF) as a suitable precursor and the importance of heteroatom doping in the carbon moiety in order to improve conductivity and durability, various MOF-derived synthetic routes through which the electrocatalyst can be synthesized, and common electrochemical parameters used for the water splitting process are discussed in this chapter.

Chapter 2: Metal-organic framework (MOF)-derived plate-shaped $CoS_{1.097}$ nanoparticles for an improved hydrogen evolution reaction



Graphical abstract

In this work, we have successfully synthesized $CoS_{1.097}$ nanoparticles starting with a Co-MOF precursor by following a solvothermal route for the sulfurization process by

taking sulfur powder as the sulfur source. The variation of sulfurization temperature played a significant role in regulating the morphology and optimizing the catalytic activity of the derived products (Temperature - 140, 160, 180 °C). The HER results suggest that the optimized $\text{CoS}_{1.097}$ -160 with uniform hexagonal plate-shaped morphology required a low overpotential of 163 mV to achieve 10 mA cm^{-2} current density and small Tafel slope of 53 mV dec^{-1} indicating suitable kinetics for HER. Additionally, 25 h of constant durability test in acidic media indicates the practical applicability of the material. This study demonstrates a temperature-dependent strategy for the synthesis of efficient $\text{CoS}_{1.097}$ nanoparticles as a suitable replacement for the noble metal-based electrocatalyst for electrochemical hydrogen production.

Chapter 3: MOF-derived Co_3S_4 nanoparticles embedded in nitrogen-doped carbon for electrochemical oxygen production

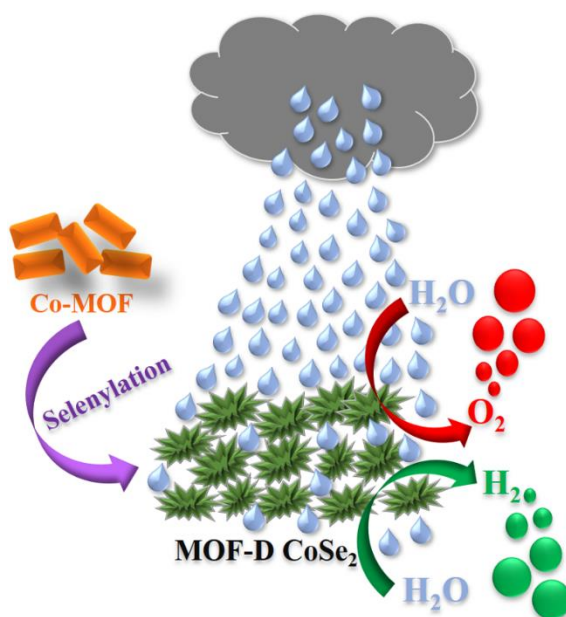


Graphical abstract

Herein, Co_3S_4 nanoparticles embedded in nitrogen doped carbon was synthesized by taking a Co-MOF precursor containing N and S heteroatoms in its ligands. A high temperature annealing treatment (700 °C) in an inert atmosphere was employed by

varying the reaction time of the annealing process (Time- 2 h, 3 h, 4 h). The alteration of reaction time had a significant impact in optimizing the surface area of the derived products. The N-doped carbon moiety regulates the electronic environment triggering the catalytic activity. The carbon embedment of the Co_3S_4 nanoparticles restrict corrosion and agglomeration during long-term electrolysis. The optimized Co_3S_4 -3h required a lower overpotential of 285 mV to deliver 10 mA cm^{-2} current density and showed excellent durability of 14 h under harsh alkaline electrolytic condition of 1.0 M KOH reflecting its practical applicability. This sacrificial annealing approach opens a new window for the synthesis of efficient cobalt sulfide (Co_3S_4) nanoparticles as a suitable replacement of the noble metal-based electrocatalyst for electrochemical oxygen production.

Chapter 4: Metal–organic framework (MOF) derived flower-shaped CoSe_2 nanoplates as a superior bifunctional electrocatalyst for both oxygen and hydrogen evolution reactions

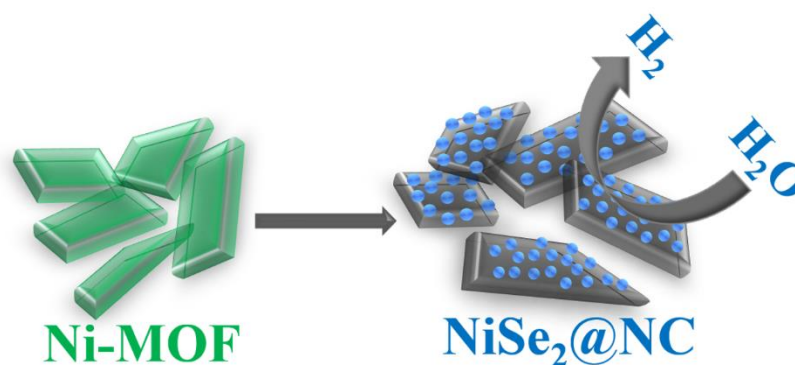


Graphical Abstract

In the present work, we have successfully synthesized flower like CoSe_2 nanoplates termed as MOF-D CoSe_2 from a Co-MOF precursor. The synthetic approach includes

a facile solvothermal step by taking selenium powder as a source of selenium. For a comparison study bare CoSe_2 was also synthesized in a non-MOF-derived strategy and its catalytic activity towards HER and OER were compared with MOF-D CoSe_2 . The flower-like morphology corresponds to a larger electrochemically active surface area with sufficient active sites beneficial for both HER and OER. The MOF-D CoSe_2 required 320 mV and 195 mV overpotential to acquire 10 mA cm^{-2} current density for OER and HER respectively. The catalyst was also remarkably stable in both alkaline and acidic media indicating its practical applicability. This work provides a feasible and cost-effective way to develop CoSe_2 electrocatalyst with substantial activity towards both OER and HER.

Chapter 5: NiSe_2 nanoparticles encapsulated in N-Doped carbon matrix derived from a one-dimensional Ni-MOF: an efficient and sustained electrocatalyst for hydrogen evolution reaction



Graphical Abstract

In the current chapter, NiSe_2 nanoparticles encapsulated in N-doped carbon was successfully synthesized and tested as a promising catalyst for electrochemical hydrogen evolution reaction. Firstly, the Ni-MOF was synthesized by a solvothermal approach followed by a two-step high-temperature pyrolysis treatment. In the first pyrolysis treatment, the variation of temperature (400-800 °C) results in the formation

of Ni-T@NC nanoparticles. Afterwards, by using selenium powder it was further subjected to high temperature treatment (300 °C) to develop NiSe₂-T@NC nanoparticles. The annealing treatment under an inert atmosphere increases the specific surface area and exposes the active sites due to the carbonization of the Ni-MOF precursor. The N-doped carbon matrix tunes the electronic and chemical environment of the NiSe₂ nanoparticles that not only enhances the conductivity but also increases the stability. The optimized NiSe₂-600@NC demands only 196 mV overpotential to reach 10 mA cm⁻² current density as well as robust durability of 24 h in an acidic electrolytic condition indicating its practical applicability. The synthetic approach and catalytic performance make the NiSe₂-600@NC a suitable alternative for noble metal-based electrocatalyst for hydrogen generation.

Synopsis conclusion

In summary, various MOF-derived metal chalcogenide-based electrocatalysts have been synthesized and their electrocatalytic activity towards oxygen and hydrogen evolution reactions are explored. Chapter 1 covers the rationale for the search for an alternative electrocatalyst for the implementation of electrochemical energy conversion, the basic techniques for characterizing the newly developed electrocatalyst, and the fundamental electrochemical parameters related to electrochemical energy conversion. The comprehensive investigation of MOF-derived plate-shaped CoS_{1.097} nanoparticles as an effective electrocatalyst for the hydrogen evolution reaction in acidic conditions is illustrated in chapter 2. The effect of temperature variation over the material's morphology and catalytic activity is also examined. In Chapter 3, a Co-MOF precursor was used to create Co₃S₄ nanoparticles embedded in nitrogen-doped carbon by a time-variation strategy, which were then evaluated as an effective electrocatalyst for oxygen production. The N-doped carbon moiety modulates the electronic

environment triggering the electrocatalytic activity for oxygen evolution reaction. Further, a viable and cost-effective solvothermal approach was employed to develop CoSe₂ nanoplates starting with a Co-MOF precursor exhibiting substantial activity towards both oxygen and hydrogen evolution in chapter 4. In chapter 5, the effective synthesis and testing of NiSe₂ nanoparticles encapsulated in N-doped carbon as a potential catalyst for electrochemical hydrogen evolution reaction is reported. It's interesting to note that temperature-alteration factor was crucial in optimizing the catalytic activity of the various derived products. Furthermore, the N-doped carbon matrix offers strong stability under acidic electrolytic conditions in addition to increasing conductivity.

LIST OF SCHEMES

Scheme No.	Caption	Page No.
Scheme 2.1	Schematic representation for the Synthesis of MOF-derived $\text{CoS}_{1.097}$ ($\text{CoS}_{1.097-160}$)	43
Scheme 3.1	Schematic representation for the Preparation of MOF-derived Co_3S_4 ($\text{Co}_3\text{S}_4-3\text{h}$)	69
Scheme 4.1	Schematic representation for the Synthesis of MOF-derived CoSe_2 (MOF-D CoSe_2)	98
Scheme 5.1	Schematic representation for the synthesis of MOF-derived NiSe_2 ($\text{NiSe}_2-600@\text{NC}$)	128

LIST OF FIGURES

Figure No.	Caption	Page No.
Figure 1.1	Electrolytic cell showing water splitting process	3
Figure 1.2	Polarization curves for HER and OER	4
Figure 1.3	Three-electrode measurement se-tup for HER and OER	6
Figure 1.4	Mechanism of hydrogen evolution reaction (HER)	7
Figure 1.5	Mechanism of oxygen evolution reaction (OER)	8
Figure 1.6	LSV plot showing onset potential and overpotential	10
Figure 1.7	Tafel plot of the electrocatalyst	12
Figure 1.8	CV in non-Faradaic potential window and corresponding double-layer capacitance (C_{dl})	13
Figure 1.9	EIS plot or Nyquist plot showing charge transfer resistance	14
Figure 1.10	Long-term stability plot	15
Figure 1.11	Volcano plot for metal-containing catalyst for HER	18
Figure 1.12	Periodic table highlighting HER/OER active non-precious metals	19
Figure 2.1	Crystal structures of Co-MOF (a-d)	44
Figure 2.2	PXRD data of Co-MOF (a), $\text{CoS}_{1.097}$ -T products (b), and bare CoS_x (c)	45
Figure 2.3	SEM analysis of Co-MOF	46
Figure 2.4	SEM images of $\text{CoS}_{1.097}$ -160 at different magnifications (a and b) and elemental mapping of $\text{CoS}_{1.097}$ -160 (c–e)	46
Figure 2.5	SEM images of $\text{CoS}_{1.097}$ -140 (a, b) and $\text{CoS}_{1.097}$ -180 at different magnifications (c, d)	47
Figure 2.6	TEM of $\text{CoS}_{1.097}$ -160 at different magnifications (a, b), HRTEM of $\text{CoS}_{1.097}$ -160 (c, d), inset in (b) is the SAED pattern	48
Figure 2.7	Full scan XPS spectra (a) and deconvoluted XPS spectra of Co 2p (b) and S 2p (c)	49
Figure 2.8	Polarization curves of $\text{CoS}_{1.097}$ -T products, Pt/C and bare CoS_x before and after iR compensation	50

Figure No.	Caption	Page No.
Figure 2.9	LSVs (a), comparison of overpotential of CoS _{1.097} -T products (b), corresponding Tafel slopes (c), EIS comparison (d), inset in (d) is the equivalent circuit diagram	51
Figure 2.10	CV of CoS _{1.097} -160 (a), estimated C _{dl} (b), stability plot of CoS _{1.097} -160 (c), LSVs of CoS _{1.097} -160 before and after 1000 CV cycles (d), inset in (c) is the SEM image of the electrocatalyst after the durability test	52
Figure 2.11	CVs of CoS _{1.097} -140 (a), CoS _{1.097} -180 (b), and bare CoS _x (c)	53
Figure 2.12	PXRD of CoS _{1.097} -160 after the stability test	54
Figure 3.1	Crystal structure (a), and PXRD of Co-MOF (b)	70
Figure 3.2	PXRD (a), and Raman spectra of Co ₃ S ₄ -T products (b)	71
Figure 3.3	SEM image of Co-MOF	71
Figure 3.4	SEM analysis of Co ₃ S ₄ -3h (a, b)	72
Figure 3.5	SEM images of Co ₃ S ₄ -2h (a, b) and Co ₃ S ₄ -4h (c, d)	72
Figure 3.6	TEM (a), HRTEM (b) and EDS elemental mapping images of Co ₃ S ₄ -3h (d)	73
Figure 3.7	BET analysis of Co ₃ S ₄ -T products (a-c)	74
Figure 3.8	Full scan XPS survey spectra of Co ₃ S ₄ -3h (a), deconvoluted XPS spectra of Co 2p (b), S 2p (c), C 1s (d), and N 1s (e)	75
Figure 3.9	LSVs before and after <i>iR</i> compensation (a-e)	77
Figure 3.10	LSVs (a), overpotential comparison of Co ₃ S ₄ -T products (b), Tafel slopes (c), EIS plot (d), inset in (d) is the equivalent circuit diagram	78
Figure 3.11	CVs of Co ₃ S ₄ -T products (a-c)	79
Figure 3.12	C _{dl} of Co ₃ S ₄ -T products (a), stability of Co ₃ S ₄ -3h (b)	80
Figure 3.13	PXRD (a), SEM (b), and TEM of Co ₃ S ₄ -3h after the stability test (c)	81
Figure 4.1	Crystal structure (a) and PXRD of Co-MOF (b)	99
Figure 4.2	PXRD of MOF-D CoSe ₂	99
Figure 4.3	SEM images of Co-MOF (a, b)	100
Figure 4.4	FESEM images of MOF-D CoSe ₂ (a-d)	101

Figure No.	Caption	Page No.
Figure 4.5	TEM (a, b) and HRTEM (c, d) images of MOF-D CoSe ₂ , inset in (d) is the SAED pattern	101
Figure 4.6	XPS survey spectra of MOF-D CoSe ₂ (a), deconvoluted XPS spectra of Co 2p (b), Se 3d (c)	103
Figure 4.7	BET analysis of Co-MOF (a), and MOF-D CoSe ₂ (b)	103
Figure 4.8	OER LSV plot (a), Tafel plot (b), EIS data (c), stability (c), CV (e), and C _{dl} of MOF-D CoSe ₂ (f)	105
Figure 4.9	OER LSVs before and after <i>iR</i> correction (a-d)	106
Figure 4.10	PXRD (a) and FESEM image of MOF-D CoSe ₂ after OER stability test (b)	107
Figure 4.11	HER LSV plot (a), Tafel plot (b), EIS data (c), stability (c), CV (e), and C _{dl} of MOF-D CoSe ₂ (f)	108
Figure 4.12	HER LSVs before and after <i>iR</i> correction (a-c)	109
Figure 4.13	PXRD (a) and FESEM image of MOF-D CoSe ₂ after HER stability test (b)	110
Figure 5.1	Crystal structures (a-d), and PXRD of Ni-MOF (b)	129
Figure 5.2	PXRD of Ni-T@NCs (a) and NiSe ₂ -T@NCs (b)	130
Figure 5.3	Raman spectra of Ni-600@NC (a) and NiSe ₂ -600@NC (b)	131
Figure 5.4	SEM images of Ni-MOF (a, b), Ni-600@NC (c, d), NiSe ₂ -600@NC (e, f)	132
Figure 5.5	SEM images of NiSe ₂ -400@NC (a, b), NiSe ₂ -500@NC (c, d), NiSe ₂ -700@NC (e, f), NiSe ₂ -800@NC (g, h)	132
Figure 5.6	TEM (a, b), HRTEM (c, d) images of NiSe ₂ -600@NCs, Inset in (c) is the SAED pattern	133
Figure 5.7	Full-scan XPS of NiSe ₂ -600@NC (a), deconvoluted XPS spectra of Ni 2p (b), Se 3d (c), C 1s (d), N 1s (e)	134
Figure 5.8	BET analysis of Ni-MOF (a) and NiSe ₂ -T@NCs (b-f)	135
Figure 5.9	LSVs before and after <i>iR</i> correction (a-f)	136
Figure 5.10	HER LSVs (a), overpotential comparison (b), Tafel slopes (c), EIS comparison (d), C _{dl} comparison of NiSe ₂ -T@NCs (e), stability of NiSe ₂ -600@NC (f)	136
Figure 5.11	CVs of NiSe ₂ -T@NCs (a-e)	137
Figure 5.12	PXRD (a) and FESEM image NiSe ₂ -600@NC after HER durability test (b)	140

LIST OF TABLES

Table No.	Caption	Page No.
Table 2.1	HER comparison of cobalt sulfide-based electrocatalysts with CoS _{1.097-160}	55
Table 3.1	OER performance comparison of Co ₃ S ₄ -3h with previous reports	83
Table 4.1	Comparison of OER activity of MOF-D CoSe ₂ with similar reported materials	111
Table 4.2	HER activity comparison of MOF-D CoSe ₂ with previous reports	112
Table 5.1	Comparison of HER activity of NiSe ₂ -600@NC with some of the reported electrocatalysts	141

LIST OF ABBREVIATION

1D	One dimensional
3D	Three-dimensional
MOF	Metal-organic framework
HER	Hydrogen evolution reaction
OER	Oxygen evolution reaction
LSV	Linear sweep voltammetry
R_s	Solution resistance
R_{ct}	Charge transfer resistance
C_{dl}	Double-layer capacitance
CPE	Constant phase elements
ECSA	Electrochemically active surface area
CP	Chronopotentiometry
WE	Working electrode
GCE	Glassy carbon electrode
CV	Cyclic voltammetry
CE	Counter electrode
RE	Reference electrode
EIS	Electro chemical impedance spectroscopy
CVD	Chemical vapor deposition
CNT	Carbon nanotubes
XPS	X-ray photoelectron spectroscopy
PXRD	Powder X-ray diffraction
FESEM	Field emission scanning electron microscope
TEM	Transmission electron microscope

HRTEM	High resolution transmission electron microscopy
EDS	Energy dispersive X-ray spectroscopy
SAED	Selected area electron diffraction
TMCs	Transition metal chalcogenides
rGO	Reduced graphene oxide
DMF	Dimethylformamide
h	Hour
min	Minute
RHE	Reversible hydrogen electrode
CC	Carbon cloth
ZIF	Zeolitic Imidazolate Framework
MIL	Materials Institute Lavoisier
mL	Milliliter
mg	Milligram

CHAPTER – 1

A brief introduction to electrochemical energy conversion process through water splitting

- 1.1** Introduction
- 1.2** Electrochemical water splitting reaction
 - 1.2.1** Different categories of water splitting reaction
 - 1.2.2** Construction of electrochemical cell
- 1.3** Mechanism associated with water splitting reaction
 - 1.3.1** Mechanism involved in hydrogen evolution reaction (HER)
 - 1.3.2** Mechanism involved in oxygen evolution reaction (OER)
- 1.4** Fundamental parameters associated with water splitting reaction
 - 1.4.1** Overpotential
 - 1.4.2** Tafel slope
 - 1.4.3** Electrochemical active surface area (ECSA)
 - 1.4.4** Electrochemical impedance spectroscopy (EIS)
 - 1.4.5** Stability
 - 1.4.6** Determination of Faradaic efficiency
- 1.5** Various electroactive materials for water splitting
 - 1.5.1** Noble metal containing materials for water splitting
 - 1.5.2** Non-precious metal-based materials for water electrolysis
 - 1.5.3** Metal oxides for water splitting reaction
 - 1.5.4** Metal phosphides for water electrolysis
 - 1.5.5** Metal chalcogenides for electrochemical water splitting
- 1.6** Metal-organic frameworks (MOFs)
 - 1.6.1** MOF-derived materials for electrocatalysis
 - 1.6.2** Different synthetic routes for MOF-derived materials
 - 1.6.3** MOF-derived metal chalcogenides for HER/OER
- 1.7** References

1.1 Introduction

The escalating energy problem and environmental damage brought on by burning conventional fossil fuels have generated significant interest in renewable energy sources for the generation of clean, green energy. The substantial dependency on fossil fuels promotes unavoidable greenhouse gas production, leading to global warming.^{1,2} Among different renewable energies, nuclear energy has an adverse effect with disastrous risk, whereas solar and wind energies have limited usage due to their intermittent nature. Hydrogen energy (H_2) is considered a suitable alternative to traditional fossil fuels due to its high energy density and zero carbon content. However, the production of hydrogen is mainly from steam methane reforming or biomass gasification, which again accelerates the release of greenhouse gases. Therefore, a different, effective, and clean method of H_2 generation is required to solve these problems. Water electrolysis is considered a clean and efficient strategy to generate hydrogen in a carbon-free manner.³⁻⁶ In general, water is electrolyzed in a conventional electrolytic cell, which composed of two half-cell reactions, the cathodic hydrogen evolution reaction (HER) and the anodic oxygen evolution reaction (OER). Theoretically, for the splitting of water molecule to respective hydrogen (H_2) and oxygen (O_2) 1.23 V is required known as thermodynamic potential of water splitting.^{7,8} However, similar to other chemical reactions, the additional energy required beyond that of the thermodynamic potential to overcome the energy barrier associated with electrochemical water splitting is known as the overpotential (difference between the thermodynamic potential and the experimental potential).⁹ In general, noble metal-based catalysts exhibit excellent catalytic activity when it comes to splitting of water involving HER and OER. Particularly, Pt-based electrocatalysts are regarded as the most efficient catalysts for HER, whereas oxides of Ir and Ru are the state-of-the-art

catalysts for OER. However, limited availability and expensive price restrict their widespread use for water splitting. As a consequence, development of non-noble metal-based electrocatalysts with significant catalytic activity for HER and OER is required in light of all these restrictions.^{10,11}

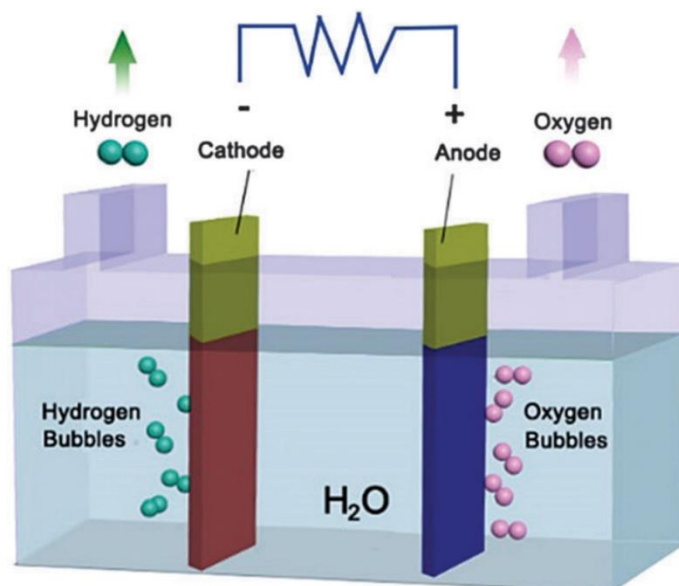
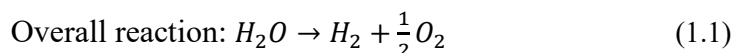


Figure 1.1: Electrolytic cell showing water splitting process.

1.2 Electrochemical water splitting reaction

Water splitting is a term frequently used to refer to electrolysis. An electrolyser is a type of cell where the water-splitting reaction occurs. By applying an external voltage to the electrode in an aqueous electrolyte medium, electrolysis converts water molecules into hydrogen and oxygen. It generally involves two half-cell reactions: one is the hydrogen evolution reaction at the catalyst-modified cathode electrode, and the other is the oxygen evolution reaction at the catalyst-coated anode electrode surface. This process generates molecular hydrogen and oxygen gas in an eco-friendly and carbon-free way.^{12,13} The water splitting reaction in an electrolytic cell can be visualize in **Figure 1.1**.¹⁴



1.2.1 Different categories of water splitting reaction

Relying on the type of electrolyte used (electrolytic medium) and the presence of active ions, water splitting can be categorised into two major types: oxygen evolution reactions (OER) and hydrogen evolution reactions (HER). When it comes to acidic medium, H^+ ions serve as the active ions, whereas OH^- ions are considered to be the active ions in alkaline medium. During water splitting, oxygen bubbles generated at the anode whereas hydrogen bubbles appeared at the cathode side.^{15–17} The water splitting reaction along with the polarization curves for cathodic HER and anodic OER are shown in **Figure 1.2**.⁸ Following is a presentation of the water splitting reaction in both acidic and alkaline medium:

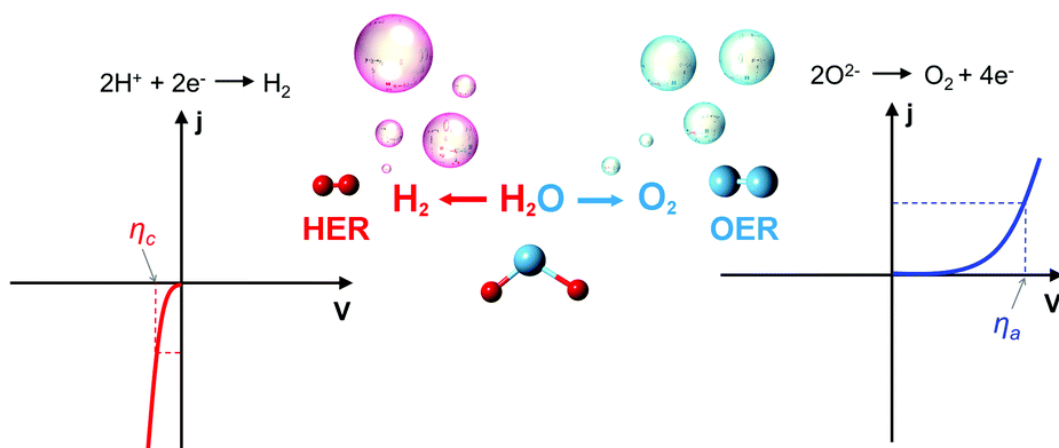
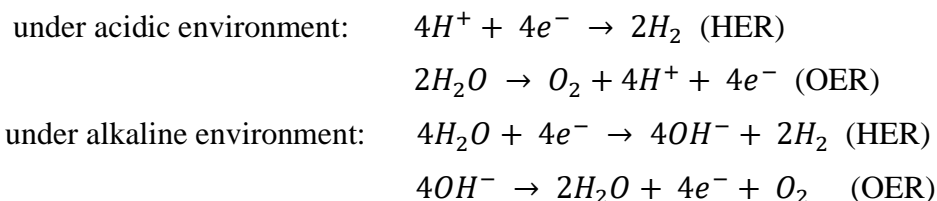


Figure 1.2: Polarization curves for hydrogen evolution reaction and oxygen evolution reaction.

In general, the energy released during the process of creating water is equal to the energy needed to break down the molecules of water in order to evolve hydrogen and

oxygen. Gibbs free energy is used to compute it under the ordinary circumstances of standard pressure and temperature.

$$\Delta G^0 = -nFE^0 \quad (1.2)$$

Here, ΔG^0 = the change in standard Gibb's free energy.

n = total number of electrons involved during the electrolysis process.

F = Faraday Constant (96485 C)

At typical conditions of temperature (25 °C) and pressure (1 atm), the thermodynamic potential needed to split water into H₂ and O₂ molecules is 1.23 V. However, in reality the slow reaction kinetics of water electrolysis necessitate additional potential than the thermodynamic potential for complete dissociation of water into molecular hydrogen and oxygen.^{9,18} In water splitting reactions, the onset potential is regarded as the potential at which the electrolysis process first begins, and the overpotential serves as the additional potential needed compared to the thermodynamic potential for water electrolysis.¹⁹

1.2.2 Construction of electrochemical cell

The electrolysis process takes place in the electrochemical cell, which is a three-electrode arrangement. The working electrode (WE) for this type of electrochemical cell is a catalyst-modified glassy carbon electrode (GCE), the counter electrode (CE) is bare platinum wire or graphite rod, and the reference electrode (RE) is either aqueous silver/silver chloride (Ag/AgCl) or mercury/mercury oxide (Hg/HgO). The typical arrangement of a three-electrode measurement set-up is depicted in **Figure 1.3**.

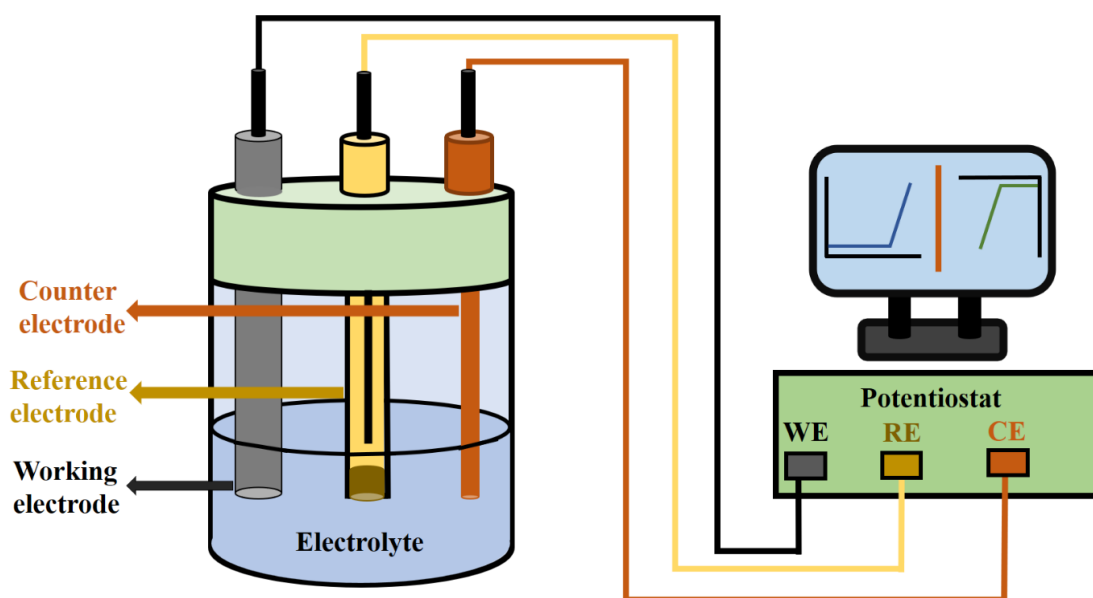


Figure 1.3: Three-electrode electrochemical set-up for HER and OER process.

An appropriate amount of the as-prepared catalyst is combined with a solvent such as ethanol and a binder like Nafion, and the mixture is ultrasonically blended to create a homogeneous catalyst slurry, which is then drop-casted onto the surface of the GCE. The method of electrode preparation directly depends on the type of electrocatalyst used. Despite the fact that the relevant electrodes are submerged in the aqueous electrolytes for water splitting, some potential has to be provided to start the electrolysis process. Using the well-known Nernst equation, the as-obtained potential values for the respective evolution of hydrogen and oxygen molecules are calibrated into the reversible hydrogen electrode (RHE) scale as follows:

For Ag/AgCl reference electrode:

$$E_{RHE} = E_{Ag/AgCl} + E^0_{Ag/AgCl} + 0.059 p^H$$

In case of Hg/HgO reference electrode,

$$E_{RHE} = E_{Hg/HgO} + E^0_{Hg/HgO} + 0.059 p^H$$

1.3 Mechanism associated with water-splitting reaction

The two categories of the water electrolysis process that yields H_2 and O_2 are HER and OER, respectively. The actual reaction mechanism associated with HER and OER in both acidic and alkaline mediums are elucidated.

1.3.1 Mechanism involved in hydrogen evolution reaction (HER)

The electrolyzer's cathodic half-reaction, known as the hydrogen evolution reaction, generally occurs when protons are reduced into molecular hydrogen after being adsorbed on the catalyst surface. This cathodic half-cell reaction uses a mechanism that relies on pH value of water (either alkaline or acidic) and follows a two-electron transfer pathway for production of H_2 from water. In general, HER adopts two steps in an acidic environment, either Volmer-Heyrovsky or Volmer-Tafel. In the Volmer step, the H^+ ion forms an adsorbed hydrogen atom known as H_{ads} by adhering to the electrocatalyst's surface. If the reaction proceeds to the Heyrovsky step after the Volmer stage, another electron-coupled hydronium ion (H^+) will mix with the adsorbed hydrogen to produce molecular hydrogen. While in the Tafel step, a hydrogen molecule is created by the combination of two adsorbed hydrogen atoms.

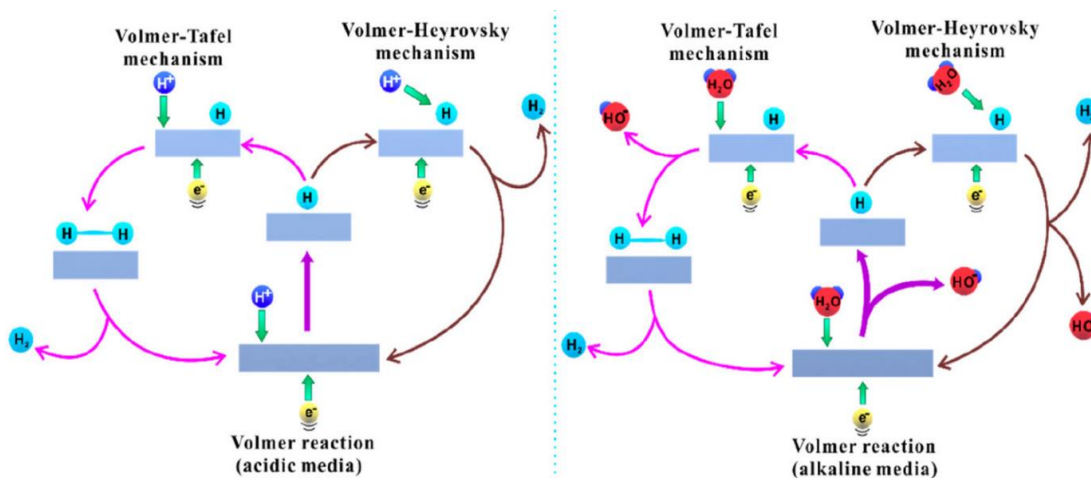


Figure 1.4: Mechanism associated with HER in acidic and alkaline environments.

Initially electron-coupled water molecules in alkaline media release the ions such as hydroxide and hydronium. The hydronium ion (H^+) forms an adsorbed hydrogen (H_{ads}) species when it gets adsorbed onto the surface of the electrocatalyst. In the Heyrovsky step, the hydrogen atom that has been adsorbed (H_{ads}) interacts with a different water molecule that has an electron pair to produce hydrogen molecule. Whereas, two H_{ads} atoms combine to form the H_2 molecule in the Tafel step.^{20,21} **Figure 1.4** represents mechanism of HER in both acidic and alkaline media.¹⁰

1.3.2 Mechanism involved in oxygen evolution reaction (OER)

At the anodic portion of the electrolyser, water oxidizes to produce O_2 molecules. The creation of several transitory species (oxide, hydroxide, and peroxide) follows a four-electron transfer pathway to finish the oxygen evolution process.

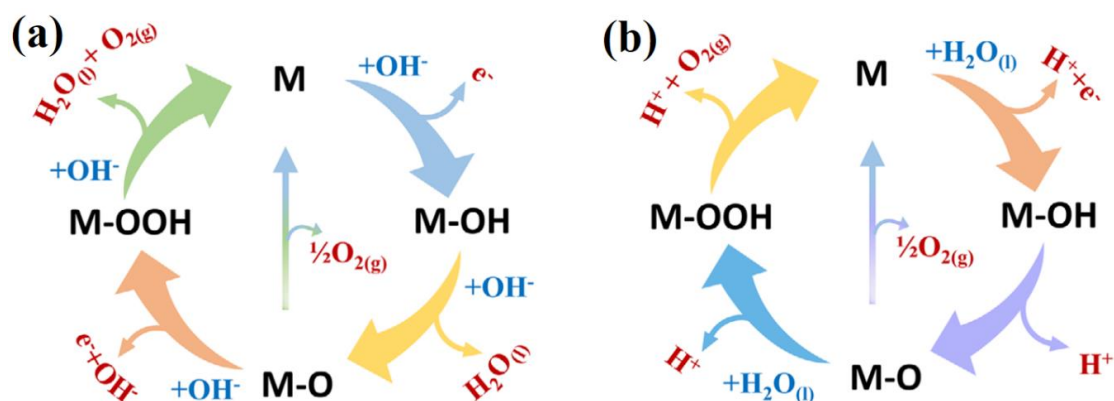


Figure 1.5: Mechanism associated with OER in alkaline (a) and acidic (b) environments.

The water oxidation process demands 1.23 V potential thermodynamically, but because of these steps, the kinetics associated with the process are sluggish and need a larger potential than the thermodynamic one. The electrolytic solution's abundantly available OH^- ions in an alkaline media cause them to adsorb on the catalytic surface and create a hydroxo species. The attack of a second OH^- ion then removes one proton from these hydroxo species, creating an oxo species. The oxo species again combines with another

hydroxide ion creating a peroxy species. Finally, another hydroxide ion attacks the peroxy species and releases molecular oxygen and water. Therefore, it may be concluded that an O₂ molecule is created using four hydroxide molecules and four electrons.^{8,22}

The water molecule splits into a proton, an electron, and a hydroxide ion in an acidic solution. This hydroxide ion forms a hydroxy species after being adsorbed on the catalyst surface, and a hydrogen ion is released from it to produce an oxide species. Another water molecule creates a hydroxide ion and a peroxy species by releasing a proton and an electron. Finally, this peroxy species produces a hydronium ion and molecular oxygen. This procedure makes it evident that two molecules of water are used to create molecular O₂ along with four electrons and protons, in an acidic medium. The OER catalytic activity of the electroactive material is entirely due to the production and breakdown of the M-O and M-OOH bonds.^{23,24} **Figure 1.5** displays the OER mechanism in both acidic and alkaline conditions.²⁵

1.4 Fundamental parameters associated with water splitting reaction

Overpotential, Tafel slope (demonstrates kinetics of the desired reaction), Nyquist plot (deals with charge transfer dynamics involved in the catalytic process), electrochemical active surface area (ECSA) with number of active sites (responsible for catalytic conversion of water to H₂ and O₂), Faradaic efficiency, long-term stability test (chronopotentiometry), and cyclic stability are some of the electrochemical parameters crucial to understand the water splitting process. These metrics can also be used to infer the actual reaction mechanism involved in the catalytic process.

1.4.1 Overpotential

According to thermodynamics, it needs 0.0 V for HER at the cathodic counterpart and 1.23 V for OER at the anodic counterpart. The practical use of water electrolysis, however, indicates that additional potential is needed to get over the kinetic barrier involved with these processes (HER and OER).^{10,26}

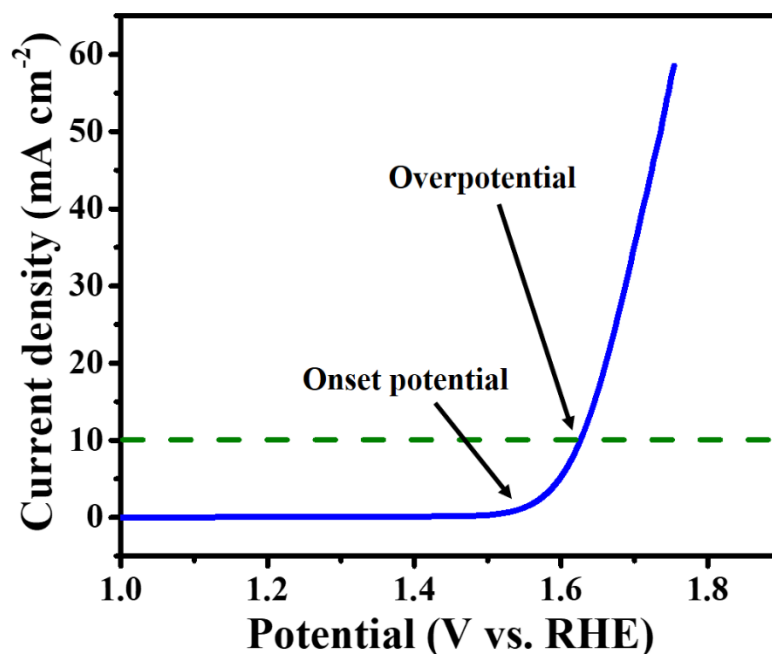


Figure 1.6: LSV plot representing onset potential and overpotential.

Overpotential is the term used to describe this additional potential compared to thermodynamic potential. Thus, researchers from all around the world are primarily interested in synthesizing efficient electrocatalysts with reduced overpotential values. In accordance with the three main variables that widen the discrepancy between experimental and thermodynamic potential, there are three categories of overpotential: (i) overpotentials associated with activation, (ii) overpotentials associated with concentration, and (iii) overpotentials associated with ohmic drop.^{18,27} An appropriate electrocatalyst can be used to reduce the activation overpotential, which is a natural characteristic of the electrode material. Constant stirring of the electrolyte solution

eliminates the concentration overpotential caused by the slower rate of charge carrier diffusion at the electrode/electrolyte interface. Similar to this, an iR correction can remove the overpotential brought on by the ohmic drop. This ohmic drop (iR) adjustment can be done by multiplying the current with the solution resistance as determined by linear sweep voltammetry and electrochemical impedance spectroscopy, respectively. The intrinsic catalytic activity of the electrocatalyst towards HER/OER is then determined by further deducting this iR value from the empirically observed potential.²⁸⁻³⁰ The needed potential to reach a current density of 10 mA cm^{-2} illustrates the effectiveness of the catalyst while the overpotential is a relative number. This 10 mA cm^{-2} current density is considered to be same as 12.3% efficiency of a solar water splitting device over 1 sun illumination.^{31,32} Therefore, the higher the efficiency of the electrocatalyst, the lower the overpotential value needed to attain this current density.

Figure 1.6 represents a LSV polarization curve for OER.

1.4.2 Tafel slope

The surface dynamics and response processes that take place throughout the HER/OER process are depicted by the Tafel slope value. An electrocatalyst's decreased Tafel slope value, which raises cathodic and anodic current density at a lower overpotential, demonstrates the higher efficiency of HER or OER catalysts.^{33,34} The Tafel slope is typically calculated from the fitted linear section of the Tafel plot. The Tafel plot is displayed as a profile of logarithm of the current density (J) versus overpotential (V). While the link between $\log(J)$ and overpotential (V) is established by the following equation,

$$\eta = a + b \log(J) \quad (1.3)$$

The Tafel constants a , Tafel slope b , the overpotential (η), and the current density (J) are all used in the equation above.^{35,36} Furthermore, the exchange current density value is determined from the extrapolation of Tafel plot that intersects the X-axis at a certain point. The presence of more active sites on the catalyst surface is suggested by a higher value for exchange current density.³⁷ A fitted linear area of the Tafel plot is shown in **Figure 1.7**. In a simple manner, we can say that for a series of compound the one having the lowest value of Tafel slope is considered to be a better catalyst with suitable kinetics for water splitting (HER and OER).

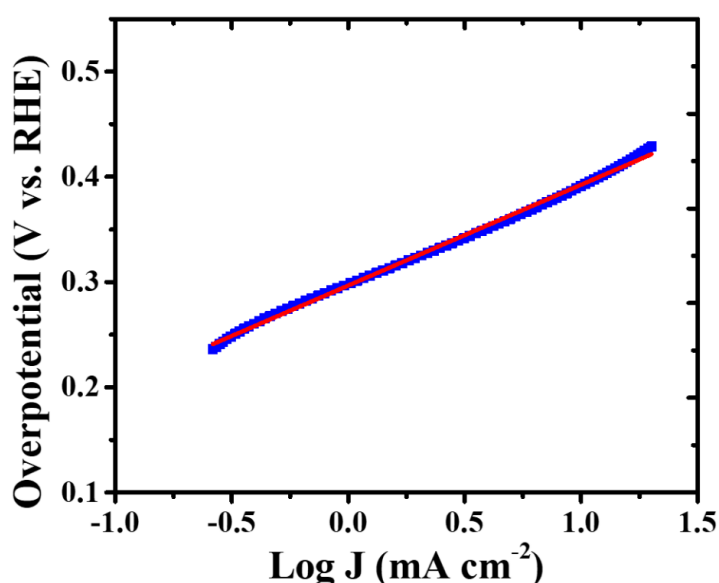


Figure 1.7: Tafel plot of the electrocatalyst.

1.4.3 Electrochemical active surface area (ECSA)

ECSA gives us a sense of the catalyst's electrochemically active surface area, unlike the specific surface area obtained through BET measurement. The ECSA value can be calculated by examining the double-layer capacitance (C_{dl}) from a non-Faradaic region of a cyclic voltammetry curve.^{38,39} The ECSA value is strongly influenced by the very porous and rough surface of the electrocatalyst. The only factor used to determine the double-layer capacitance is the charge accumulation process that corresponds to a

charge of layers at the electrode/electrolyte interface without any redox reaction. In general, first the double-layer capacitance (C_{dl}) was calculated using the cyclic voltammetry (CV) method with various scan rates in a specific non-Faradaic potential window. By plotting the half of the difference of cathodic and anodic current densities ($\Delta J = J_a - J_c$) versus different scan rates a straight line is obtained, whose slope is equal to the double-layer capacitance of the electrocatalyst.⁴⁰⁻⁴² ECSA has a linear relation with the double layer capacitance, more is the value of C_{dl} more will be the electrochemically active surface area available for the catalytic conversion of water in to H_2 and O_2 .⁴³ **Figure 1.8** shows the CV in non-Faradaic potential window and its corresponding C_{dl} .

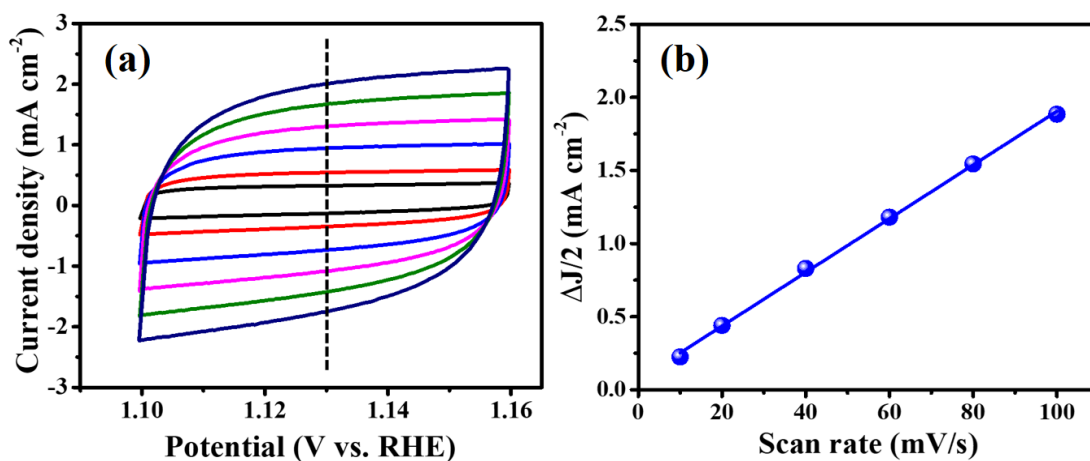


Figure 1.8: CV in non-Faradaic potential window (a) and evaluation of C_{dl} from various scan rates (b).

1.4.4 Electrochemical impedance spectroscopy (EIS)

By using Nyquist plot analysis through EIS measurements, it is possible to examine an electrocatalyst's solution resistance, charge transfer resistance, and mass transfer activity. The Nyquist plot compares an imaginary axis (Z'') to a real axis (Z') to examine the charge transfer dynamics associated with the material. By changing the AC frequency from a higher to a lower value at a specific potential and amplitude, this Nyquist diagram can be produced.^{44,45} Impedance is a type of resistance that can either

follows or defies Ohm's law. In addition to providing information about various electronic components involved in the electrochemical reactions, each point on the Nyquist plot represents a certain frequency and illustrates double-layer capacitance, solution resistance, and charge transfer resistance. Solution resistance is the sum of the contact resistance between the electrode and active material interface, the resistance of the electrolytic ions, and the inherent resistance of the electrode itself. In general, R_s offers the corresponding series resistance ($Z' = R_s, Z'' = 0$) at the higher frequency region of the Nyquist plot by intercepting the real axis (Z'). Additionally, the radius of the arc/semicircle from the Nyquist plot is used to calculate the value of R_{ct} (charge transfer resistance). The lower the diameter of the arc in the Nyquist plot, lower is the charge transfer resistance indicating faster rate of electron transfer in the associated material.^{46–}

⁴⁹ According to **Figure 1.9**, the one having lowest value of R_{ct} is considered to be a better catalyst with suitable catalytic activity.⁵⁰ The results obtained from the EIS plot fitted in to a corresponding equivalent circuit. The inset in **Figure 1.9** represents circuit diagram where R_s is the solution resistance, R_{ct} is the charge transfer resistance, and CPE is the constant phase element.

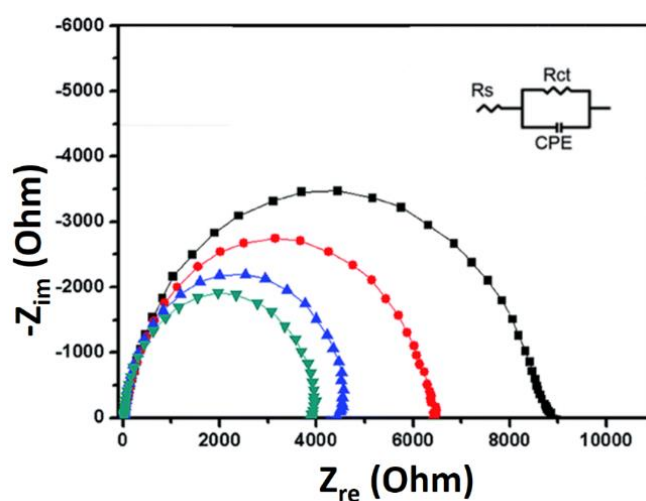


Figure 1.9: Nyquist plot or EIS plot showing the charge-transfer resistance.

1.4.5 Stability (Durability)

Stability is one of the key parameters to examine the practical applicability of the as-prepared electrocatalyst. There are several methods for evaluating the durability of the material such as chronopotentiometry, chronoamperometry, and repetitive cyclic voltammetry. In case of chronopotentiometry technique the change in overpotential is generally investigated with the progress of time at a constant current density (10 mA cm^{-2}). This is a plot between the potential versus time by keeping the current density constant. A small increase in overpotential after several hours of constant electrolysis indicates significant stability of the used electrocatalyst. Chronoamperometry technique evaluates the electrocatalyst's long-term stability performance at a specific potential by recording the deviation in current density with progression of time. After the chronoamperometry test the lesser is the decrease in current density value at that specific potential better is the electrocatalyst for the desired application. In a similar fashion, the cyclic voltammetry method compares the change in overpotential of the electrocatalyst before and after several repetitive CVs in a potential window including the onset potential region. An electrocatalyst is considered to be stable if there is small increase in overpotential after multiple CVs.⁵¹⁻⁵³ **Figure 1.10** indicates long-term stability test at a constant current density of 10 mA cm^{-2} .⁵⁴

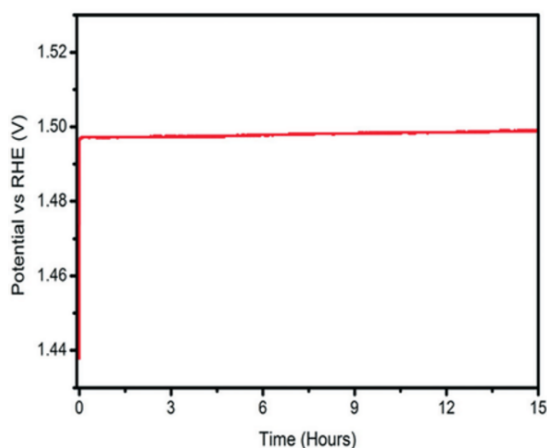


Figure 1.10 long-term stability plot of the electrocatalyst.

1.4.6 Determination of Faradaic efficiency

The term "Faradaic efficiency" refers to a critical parameter that determines the efficiency of an electrochemical process related to the Faraday's law of electrolysis. In the case of hydrogen or oxygen evolution reaction, the Faradaic efficiency analyzes the quantity of hydrogen or oxygen molecules actually found with the anticipated quantity.^{55,56} Faradaic efficiency is valued using the following equation;

$$\text{Faradaic Efficiency} = \frac{I_R \times n_D}{I_D \times n_R \times N_{CL}} \quad (1.4)$$

In the equation above, the ring and disc currents are denoted as I_R and I_D , respectively. n_D and n_R are used to represent countable electrons during the entire electrochemical analysis (includes ORR and OER). The collection efficiency of the electrochemical setup is represented by N_{CL} .

1.5 Various electroactive materials for water splitting

The electrocatalytic evolution of renewable hydrogen and oxygen molecules is significantly influenced by the various precious and non-precious metals. Noble metals like palladium (Pd) and platinum (Pt), as well as some other precious metal-based oxides like ruthenium oxide (RuO_2) and iridium oxide (IrO_2), are the preferred catalysts for the electrocatalysis process. In addition to this precious metal-based catalyst, a number of additional non-precious metal-based electrocatalysts are employed to mitigate the high cost associated with the noble metal-based catalysts. Nowadays, effective electrocatalysts for HER and OER with non-noble metals have been developed via a range of innovative synthetic techniques. Their catalytic activities are studied and compared with that of electrocatalysts based on noble metals.

1.5.1 Noble metal containing materials for water splitting

Theoretical studies show that molecular hydrogen and oxygen gases can be generated from water electrolysis by operating the two and four-electron reaction mechanisms at thermodynamic potentials of 0 V and 1.23 V (versus RHE). A significant value of overpotential is necessary for the electrocatalytic process for splitting the water. In general, noble metals such as platinum (Pt), palladium (Pd), ruthenium oxide (RuO₂), and iridium oxide (IrO₂) reduce the value of extra potential (overpotential). Platinum (Pt) is the benchmark catalyst for the HER process, because a smaller amount of additional potential is required for reaching the state of art current density of 10 mA cm⁻² (the typical current density value). Similar to this, in order to boost the catalytic activity of oxygen evolution in the supporting electrolytes, both ruthenium oxide (RuO₂) and iridium oxide (IrO₂) are regarded as the primary electrocatalysts. However, its expensive price, low abundance, and poor electrochemical stability limit its wide range of useful applications. As a result, scientists are working hard to create electrocatalysts devoid of noble metals that can function electrochemically better than catalysts based on noble metals. Other than their superior electrochemical performance, non-noble metal-based catalysts have an advantage over noble metal-based catalysts in terms of cost and durability.^{8,10} In light of these benefits, non-noble metal-based electroactive materials in their pure and carbon-based forms are desirable options for electrocatalytic applications. The volcano plot for various metal containing catalysts is presented in **Figure 1.11**.⁵⁷

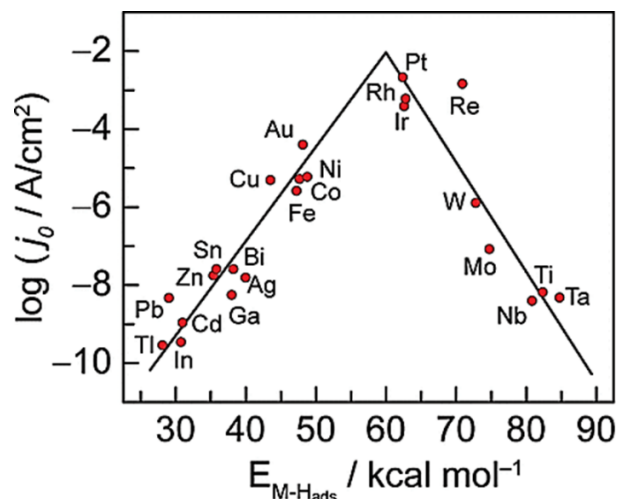


Figure 1.11: Volcano plot for metal-containing catalysts for hydrogen evolution.

1.5.2 Non-precious metal-based materials for water electrolysis

The expensive price tag and poor durability of the noble metal-based electrocatalysts prevent their widespread industrial use. In recent years several non-noble metals containing electrocatalysts of V, Co, Ni, Fe, Cu, Mo and W have been explored in the field of electrochemical water splitting.^{58,59} **Figure 1.12** highlights the non-precious metals basically used for developing efficient electrocatalysts for HER and OER. With regard to their intrinsic catalytic activity, transition metal oxides, phosphides, and carbides stand out among several non-precious transition metal-containing electrocatalysts as the prime candidates for HER and OER.^{60–62} Due to their intrinsic catalytic activity, morphological tunability, favourable bandgap and electronic structure, transition metal chalcogenides (TMCs) in particular have received a lot of interest.⁶³ The electrocatalysts should be able to guarantee quick electron and mass transport as well as plentiful regions for surface reactions in order to efficiently catalyze these electrochemical reactions. Complex nanoarchitectures, on the other hand, hinder the catalytic activity, resulting in substandard electrochemical performance for HER and OER.

The figure shows a standard periodic table with a blue rectangular highlight around the transition metal block. The highlighted elements are Vanadium (V), Chromium (Cr), Manganese (Mn), Iron (Fe), Cobalt (Co), Nickel (Ni), Copper (Cu), Zinc (Zn), Molybdenum (Mo), Tungsten (W), Rhenium (Re), Osmium (Os), Iridium (Ir), Platinum (Pt), Gold (Au), and Silver (Ag). These elements are known for their activity in the Hydrogen Evolution Reaction (HER) and Oxygen Evolution Reaction (OER).

Figure 1.12: Periodic table highlighting HER/OER active non-precious metals.

1.5.3 Metal oxides for water splitting reaction

Due to their semiconducting properties, metal oxides are seen as a strong competitor for the HER/OER process. The benefits of a changing oxidation state and strong electrical conductivity make non-precious metal oxides a desirable option for the energy sector.⁶⁴ The noble metal oxides of ruthenium (RuO_2) and iridium (IrO_2) are used as standard electrode materials to improve electrocatalytic performances basically in the oxygen evolution process (OER).⁸ However, its high price and limited supply promotes the search for noble metal-free electrocatalysts having acceptable catalytic performance. Surprisingly, metal oxides of Co, Ni, Fe, and Mn were extensively studied and suggested as excellent anode materials for general water splitting. Chen et al. designed microwave-assisted Co_3O_4 nanoflakes and tested it as efficient OER electrocatalyst that demand an overpotential of 380 mV to acquire 10 mA cm^{-2} current density.⁶⁵ Similarly, Meng et al. studied the structure-property relationship of different phases of MnO_2 and investigated the effect of different crystallographic structures on the catalytic performance of OER.⁶⁶ Shi and co-workers developed spinel-phase

NiCo₂O₄ nanoneedles and explored their catalytic activity towards OER, which required an overpotential of 323 mV to achieve 10 mA cm⁻² current density.⁶⁷ Though a wide range of research has been explored in the field of transition metal oxides, they still suffer from poor electrical conductivity, sub-standard stability in acidic media, weak adsorption capacity, which leads to an increase in the value of the overpotential during water electrolysis.⁶⁸

1.5.4 Metal phosphides for water electrolysis

Recently, nanostructured transition metal phosphides (TMPs) have become a new class of water splitting catalysts owing to their low cost and reactivity. In particular, it has been observed that a number of nanostructured phosphides of cobalt, nickel, iron and molybdenum, explored as efficient electrocatalyst for HER and OER with acceptable overpotentials.^{69,70} Bulk TMPs, however, exhibit sluggish conductivity, comparatively higher overpotential, and slower charge transfer kinetics than modern electrocatalysts for OER and HER. The problems with TMPs that can affect the catalytic activity for water splitting (HER and OER) have been addressed in a number of ways. Through the use of sulfur doping, Wu et al. created Ni₂P and examined its catalytic activity toward both HER and OER. The S-doped Ni₂P demanded 290 mV and 331 mV of overpotential to attain 10 mA cm⁻² current density for HER and OER, respectively.⁷¹ Liu et al. developed porous Mn-doped cobalt phosphide having a nanosheet like architecture and examined its OER activity in alkaline environment of 1.0 M KOH. The as-synthesized Mn doped CoP catalyst needed an overpotential of 288 mV to achieve the pre-defined current density of 10 mA cm⁻².⁷² Although, several progresses have been made in the field of TMPs more issues to be addressed regarding conductivity and poor chemical stability.⁷³

1.5.5 Metal chalcogenides for electrochemical water splitting

Researchers have recently become quite interested in transition metal chalcogenides (TMCs) due to their excellent designability in morphology and various electronic structure, as well as their comparatively good intrinsic electrocatalytic water splitting activity. TMCs have distinct chemical and physical properties that can be greatly improved by adjusting the electrical parameters or tuning the morphology in nanoscale dimension.^{18,74} Ge et al. synthesized NiS₂ nanosheets and explored their cathodic hydrogen evolution ability in an acidic medium (0.5 M H₂SO₄). The as-synthesized electrocatalyst required a low overpotential of 213 mV to show 10 mA cm⁻² current density.⁷⁵ In view of preparing a cobalt-based efficient HER electrocatalyst, Lin et al. synthesized two distinct metallic phases of CoSe (tetragonal and hexagonal) and compared their catalytic activity for electrochemical HER in an acidic medium. Interestingly, the tetragonal CoSe dominates over the hexagonal phase both in terms of activity as well as conductivity. The tetragonal CoSe needed 175 mV overpotential in order to achieve 10 mA cm⁻² current density, which is much lower as compared to the overpotential of hexagonal CoSe (352 mV).⁷⁶ Bulk chalcogenides still have some drawbacks, though, because they aggregate easily and have fewer electrochemical active sites, which raises the overpotential during electrochemical reactions. To get around these constraints, a number of approaches have been designed to alter the bulk chalcogenides' surface chemical structure, improving their stability and speeding up their charge transport for greater catalytic performance. A traditional method for avoiding corrosion and the accumulation of electroactive material during prolonged electrolysis is the embedding of a carbon moiety. Another approach that is beneficial in terms of conductivity and chemical stability is the insertion of the heteroatom-doped carbon (N-doped carbon).^{77,78} Keeping in mind such limitations, Sivanantham et al.

designed a series of core-shell cobalt-based chalcogenide nanoarchitectures; sulfide, selenide, telluride (Co₉S₈@NC, CoSe@NC and CoTe@NC) and compared their catalytic performance for OER. In all the cases, the inner chalcogenide core is protected by outer nanocarbon part. Among all, the Co₉S₈@NC emerged as a better catalyst for OER requiring only 288 mV overpotential to deliver the state of the art 10 mA cm⁻² current density.⁷⁹ Nevertheless, more focus needs to be implemented on designing of efficient chalcogenide-based electrocatalysts that can create a bridge between the morphology and catalytic activity towards HER and OER.

1.6 Metal-organic frameworks (MOFs)

Metal-organic frameworks (MOFs), a new family of materials with crystalline structure, extraordinary porosity, structural flexibility, and adjustable functionality, are created by joining metal ions or clusters with organic linkers. A lot of work has been put towards creating MOFs as functional materials for a variety of uses, including gas separation, drug delivery, catalysis, gas storage, and sensing.⁸⁰⁻⁸² The choice of a suitable MOF for a given application becomes the most crucial factor in doing the intended work with proper result. In the area of energy storage and conversion, MOF-based materials, which involves pristine MOFs, MOF composites, and MOF-derived materials, have become the major subject of current research.⁸³

1.6.1 MOF-derived materials for electrocatalysis

The insufficient electrical conductivity and stability under working conditions of numerous MOFs severely limit their potential for use in the energy sector, including electrochemical energy conversion.⁸⁴ As a result, researchers are focusing on developing a variety of functional materials with impressive performance for HER and OER utilizing MOF as a sacrificial template. Pure MOFs and MOF composites can be

transformed into various nanoarchitectures including metal compounds nanoparticles, metal nanoparticles/carbon composites, and MOF-derived carbon by carefully regulating the chemical or thermal processes.⁸⁵⁻⁸⁷ The MOF-derived approach is significant in a number of ways, including (i) revealing the active sites contained in the porous structure of MOFs; (ii) facilitating the well-dispersion of metal species in carbon-based materials; (iii) increasing the material's redox activity; and (iv) accelerating mass transport during the electrocatalytic process.⁸⁷⁻⁸⁹ The synthesis of effective functional electrode materials for electrochemical energy conversion applications involving HER and OER is greatly facilitated by the MOF-derived technique. The compositional and structural characteristics of MOF precursors as well as the conversion conditions, such as synthesis temperature and atmospheres, have an impact on the conversion processes and mechanisms from MOF precursors to the appropriate MOF-derived carbon, metal compounds, and their composites. Pristine MOFs can be designed and used as excellent sacrificial templates in order to synthesize MOF-derived nanomaterials with desired structural and compositional properties by carefully choosing metal nodes and organic ligands, precisely controlling experimental conditions, and post-synthetic modification.^{90,91} However, the lack of the appropriate MOF template imposes significant restrictions on the current research field except some of the well-known mono ligand-based MOFs (ZIF-67, MIL-101).^{92,93}

1.6.2 Different synthetic routes for MOF-derived materials

It is possible to create effective MOF-derived materials with good catalytic performance for HER and OER using a variety of synthetic methods. The most popular methods for altering MOF after its synthesis are pyrolysis and solvothermal treatment. One method is pyrolysis, which involves subjecting the MOF precursor to an elevated temperature thermal treatment while maintaining an inert atmosphere for the required

period of time. The metal component of the MOF precursor is transformed into metal nanoparticles or metal compound nanoparticles during pyrolysis, while the organic ligand component is carbonized to add further carbon support. The heteroatoms included in the MOF's organic ligands enable the formation of heteroatom-doped carbon, which has favourable electrical conductivity. Other sources (selenium powder, sulfur powder) are also used during the pyrolysis process for the creation of specific metal compound nanoparticles (sulfides, selenides), starting with a MOF precursor.^{39,94,95} In pyrolysis, the MOF precursor is typically taken in a porcelain boat, then placed in the middle of a tube furnace and heated under an inert atmosphere (Ar/N₂) for a specific period of time. In the pyrolysis process, changing the reaction parameters (reaction time and temperature) results in a variety of morphologies that have an impact on the target material's catalytic activity.^{85,86} As a result, adjusting reaction time and temperature is crucial for maximizing the catalytic activity of the electrocatalyst. Similarly, in case of solvothermal synthesis, suitable chemicals are employed as sources for generating particular metal compound nanoparticles (metal sulfides, selenides, tellurides, phosphides), in addition to the MOF. The pristine MOF's uniform distribution of metal nodes and organic ligands provides a platform for the creation of porous functional nanomaterials with high surface areas. In solvothermal synthetic route, metal doping is another approach for creating effective materials with strong electrical conductivity and kinetics that can reduce the energy barrier associated with the water splitting reaction.^{91,96}

1.6.3 MOF-derived metal chalcogenides for HER/OER

Metal-organic frameworks (MOFs) are considered to be a great starting material for building hollow, porous structures because of their varied composition and adjustable structure.^{87,88} In reality, using a specific chemical conversion technique, MOFs may

effectively drive the manufacturing of various electrocatalysts with preserved morphology and derived composition.⁹² Researchers frequently use MOF-derived synthetic approaches to overcome the problems with bulk metal chalcogenides (e.g., low conductivity, easy aggregation during ongoing electrolysis, and limited electrochemically active sites). The heteroatom-doped carbon network generated from the ligands raises the conductivity and offers significant stability during prolonged electrolysis, whereas the porous nanostructure made from the MOFs increases the number of catalytic active sites.^{97,98} Li et al. synthesized core-shell nitrogen-doped graphene embedded NiSe₂ nanoparticles starting with a Ni-MOF that required 201 mV overpotential at 10 mA cm⁻² current density for HER and excellent stability of 18 hours in an acidic electrolytic condition.⁹⁹ The synthesis of heterostructures with abundant heterointerfaces is a fine strategy to improve the catalytic activity of the electrocatalyst for HER and OER. In a similar way, Yang and co-workers fabricated MOF-derived hollow CoS_x@MoS₂ microcubes and tested it as a bifunctional electrocatalyst for both HER and OER. The as-prepared CoS_x@MoS₂ required 239 mV overpotential for HER (acidic media) and 347 mV overpotential for OER (alkaline media) to achieve 10 mA cm⁻² current density.⁹⁶ By adopting a high-temperature annealing strategy in an Ar atmosphere, Liu et al. designed CoSe₂ microspheres having hollow interiors starting with a Co-MOF, that required 330 mV overpotential to obtain 10 mA cm⁻² current density for OER.¹⁰⁰ For any electrocatalytic reaction, the electron transfer dynamics play an important role in affecting the overall conductivity. Considering conductivity as a key parameter for the energy conversion process, Sun et al. synthesized Co_xS_y electrocatalyst by in-situ sulfurization of a MOF, taking reduce graphene oxide (rGO) as an additional carbonaceous source. The synthesized Co_xS_y demanded 188 mV overpotential in order to acquire 10 mA cm⁻² current density for the hydrogen evolution

reaction.¹⁰¹ Although numerous initiatives have been taken to make MOF-derived chalcogenides an acceptable substitute for noble metal-based electrocatalysts for HER and OER,^{102–104} more attention needs to be paid to attaining comparably superior activity with longer chemical stability.

1.7 References

- 1 N. Kumar, K. Naveen, M. Kumar, T. C. Nagaiah, R. Sakla, A. Ghosh, V. Siruguri, S. Sadhukhan, S. Kanungo and A. K. Paul, *ACS Appl. Energy Mater.*, 2021, **4**, 1323–1334.
- 2 S. Ghosh and R. N. Basu, *Nanoscale*, 2018, **10**, 11241–11280.
- 3 J. O. M. Bockris, *Int. J. Hydrogen Energy*, 2002, **27**, 731–740.
- 4 B. H. R. Suryanto, Y. Wang, R. K. Hocking, W. Adamson and C. Zhao, *Nat. Commun.*, 2019, **10**, 1–10.
- 5 P. Hota, A. Das and D. K. Maiti, *Int. J. Hydrogen Energy*, 2023, **48**, 523–541.
- 6 S. Wang, A. Lu and C. J. Zhong, *Nano Converg.*, 2021, **8**, 1–23.
- 7 S. Liu, M. Li, C. Wang, P. Jiang, L. Hu and Q. Chen, *ACS Sustain. Chem. Eng.*, 2018, **6**, 9137–9144.
- 8 N. T. Suen, S. F. Hung, Q. Quan, N. Zhang, Y. J. Xu and H. M. Chen, *Chem. Soc. Rev.*, 2017, **46**, 337–365.
- 9 M. Chatenet, B. G. Pollet, D. R. Dekel, F. Dionigi, J. Deseure, P. Millet, R. D. Braatz, M. Z. Bazant, M. Eikerling, I. Staffell, P. Balcombe, Y. Shao-Horn and H. Schäfer, *Chem. Soc. Rev.*, 2022, **51**, 4583–4762.
- 10 J. Zhu, L. Hu, P. Zhao, L. Y. S. Lee and K. Y. Wong, *Chem. Rev.*, 2020, **120**, 851–918.

- 11 J. Song, C. Wei, Z. F. Huang, C. Liu, L. Zeng, X. Wang and Z. J. Xu, *Chem. Soc. Rev.*, 2020, **49**, 2196–2214.
- 12 Q. Wang, C. S. Cha, J. Lu and L. Zhuang, *Phys. Chem. Chem. Phys.*, 2009, **11**, 679–687.
- 13 A. Raveendran, M. Chandran and R. Dhanusuraman, *RSC Adv.*, 2023, **13**, 3843–3876.
- 14 X. Zou and Y. Zhang, *Chem. Soc. Rev.*, 2015, **44**, 5148–5180.
- 15 H. Yang, M. Driess and P. W. Menezes, *Adv. Energy Mater.*, 2021, **11**, 2102074.
- 16 M. Plevová, J. Hnát and K. Bouzek, *J. Power Sources*, 2021, **507**, 230072.
- 17 Y. Han, X. Yue, Y. Jin, X. Huang and P. K. Shen, *J. Mater. Chem. A*, 2016, **4**, 3673–3677.
- 18 S. Anantharaj, S. R. Ede, K. Sakthikumar, K. Karthick, S. Mishra and S. Kundu, *ACS Catal.*, 2016, **6**, 8069–8097.
- 19 H. Sun, X. Xu, H. Kim, W. C. Jung, W. Zhou and Z. Shao, *Energy Environ. Mater.*, 2023, 1–21.
- 20 M. Zeng and Y. Li, *J. Mater. Chem. A*, 2015, **3**, 14942–14962.
- 21 W. Luo, Y. Wang and C. Cheng, *Mater. Today Phys.*, 2020, **15**, 100274.
- 22 X. Xie, L. Du, L. Yan, S. Park, Y. Qiu, J. Sokolowski, W. Wang and Y. Shao, *Adv. Funct. Mater.*, 2022, **32**, 2110036.
- 23 A. M. R. Ramírez, S. Heidari, A. Vergara, M. V. Aguilera, P. Preuss, M. B. Camarada and A. Fischer, *ACS Mater. Au*, 2023, **3**, 177–200.
- 24 Z. Yan, H. Liu, Z. Hao, M. Yu, X. Chen and J. Chen, *Chem. Sci.*, 2020, **11**,

10614–10625.

- 25 N. Ismail, F. Qin, C. Fang, D. Liu, B. Liu, X. Liu, Z. Wu, Z. Chen and W. Chen, *Aggregate*, 2021, **2**, 1–22.
- 26 W. Zhang, L. Cui and J. Liu, *J. Alloys Compd.*, 2020, **821**, 153542.
- 27 J. H. Kim, K. Kawashima, B. R. Wygant, O. Mabayoje, Y. Liu, J. H. Wang and C. B. Mullins, *ACS Appl. Energy Mater.*, 2018, **1**, 5145–5150.
- 28 Y. Shi and B. Zhang, *Chem. Soc. Rev.*, 2016, **45**, 1529–1541.
- 29 M. K. Sahoo, A. K. Samantara and J. N. Behera, *Inorg. Chem.*, 2020, **59**, 12252–12262.
- 30 J. K. Das, A. K. Samantara, A. K. Nayak, D. Pradhan and J. N. Behera, *Dalton Trans.*, 2018, **47**, 13792–13799.
- 31 J. D. Benck, T. R. Hellstern, J. Kibsgaard, P. Chakthranont and T. F. Jaramillo, *ACS Catal.*, 2014, **4**, 3957–3971.
- 32 Q. Gao, W. Zhang, Z. Shi, L. Yang and Y. Tang, *Adv. Mater.*, 2019, **31**, 1–35.
- 33 Y. Pan, Y. Chen, Y. Lin, P. Cui, K. Sun, Y. Liu and C. Liu, *J. Mater. Chem. A*, 2016, **4**, 14675–14686.
- 34 Y. C. Zhang, C. Han, J. Gao, L. Pan, J. Wu, X. D. Zhu and J. J. Zou, *ACS Catal.*, 2021, **11**, 12485–12509.
- 35 Y. Wang, Z. Zhang, X. Liu, F. Ding, P. Zou, X. Wang, Q. Zhao and H. Rao, *ACS Sustain. Chem. Eng.*, 2018, **6**, 12511–12521.
- 36 Y. Lu, Y. Deng, S. Lu, Y. Liu, J. Lang, X. Cao and H. Gu, *Nanoscale*, 2019, **11**, 21259–21265.

- 37 L. Ma, X. Shen, H. Zhou, G. Zhu, Z. Ji and K. Chen, *J. Mater. Chem. A*, 2015, **3**, 5337–5343.
- 38 Y. R. Hong, S. Mhin, K. M. Kim, W. S. Han, H. Choi, G. Ali, K. Y. Chung, H. J. Lee, S. I. Moon, S. Dutta, S. Sun, Y. G. Jung, T. Song and H. S. Han, *J. Mater. Chem. A*, 2019, **7**, 3592–3602.
- 39 Z. Huang, J. Liu, Z. Xiao, H. Fu, W. Fan, B. Xu, B. Dong, D. Liu, F. Dai and D. Sun, *Nanoscale*, 2018, **10**, 22758–22765.
- 40 S. Jung, C. C. L. McCrory, I. M. Ferrer, J. C. Peters and T. F. Jaramillo, *J. Mater. Chem. A*, 2016, **4**, 3068–3076.
- 41 F. Song and X. Hu, *Nat. Commun.*, 2014, **5**, 4474.
- 42 X. Wang, F. Li, W. Li, W. Gao, Y. Tang and R. Li, *J. Mater. Chem. A*, 2017, **5**, 17982–17989.
- 43 H. Lu, Y. Zhang, Y. Huang, C. Zhang and T. Liu, *ACS Appl. Mater. Interfaces*, 2019, **11**, 3372–3381.
- 44 Y. Guo, C. Zhang, J. Zhang, K. Dastafkan, K. Wang, C. Zhao and Z. Shi, *ACS Sustain. Chem. Eng.*, 2021, **9**, 2047–2056.
- 45 Q. Wang, G. C. Xu, D. J. Liu, H. Ding and L. Zhang, *Int. J. Hydrogen Energy*, 2023, **48**, 12712–12722.
- 46 H. Ding, G. Xu, L. Zhang, B. Wei, J. Hei and L. Chen, *J. Colloid Interface Sci.*, 2020, **566**, 296–303.
- 47 A. Karmakar, R. Jayan, A. Das, A. Kallloorikal, M. M. Islam and S. Kundu, *ACS Appl. Mater. Interfaces*, 2023, **15**, 26928–26938.
- 48 R. Biswas, P. Thakur, I. Ahmed, T. Rom, M. S. Ali, R. A. Patil, B. Kumar, S.

- Som, D. Chopra, A. K. Paul, Y. R. Ma and K. K. Haldar, *Energy and Fuels*, 2023, **37**, 604–613.
- 49 M. Ghaemmaghami, Y. Yamini, E. Saievar-Iranizad and A. Bayat, *Sustain. Energy Fuels*, 2020, **4**, 1150–1156.
- 50 Y. Yang, K. Ri, A. Mei, L. Liu, M. Hu, T. Liu, X. Li and H. Han, *J. Mater. Chem. A*, 2015, **3**, 9103–9107.
- 51 Z. F. Huang, J. Song, K. Li, M. Tahir, Y. T. Wang, L. Pan, L. Wang, X. Zhang and J. J. Zou, *J. Am. Chem. Soc.*, 2016, **138**, 1359–1365.
- 52 S. Ju, Y. Liu, H. Chen, F. Tan, A. Yuan, X. Li and G. Zhu, *ACS Appl. Energy Mater.*, 2019, **2**, 4439–4449.
- 53 H. Liang, D. Jiang, S. Wei, X. Cao, T. Chen, B. Huo, Z. Peng, C. Li and J. Liu, *J. Mater. Chem. A*, 2018, **6**, 16235–16245.
- 54 A. Tahira, Z. H. Ibupoto, M. Vagin, U. Aftab, M. I. Abro, M. Willander and O. Nur, *Catal. Sci. Technol.*, 2019, **9**, 2879–2887.
- 55 J. Masud, A. T. Swesi, W. P. R. Liyanage and M. Nath, *ACS Appl. Mater. Interfaces*, 2016, **8**, 17292–17302.
- 56 A. T. Swesi, J. Masud and M. Nath, *Energy Environ. Sci.*, 2016, **9**, 1771–1782.
- 57 H. Tabassum, A. Mahmood, B. Zhu, Z. Liang, R. Zhong, S. Guo and R. Zou, *Energy Environ. Sci.*, 2019, **12**, 2924–2956.
- 58 J. Verma and S. Goel, *Int. J. Hydrogen Energy*, 2022, **47**, 38964–38982.
- 59 R. Y. Fan, J. Y. Xie, N. Yu, Y. M. Chai and B. Dong, *Int. J. Hydrogen Energy*, 2022, **47**, 10547–10572.
- 60 A. Parra-Puerto, K. L. Ng, K. Fahy, A. E. Goode, M. P. Ryan and A. Kucernak,

- ACS Catal.*, 2019, **9**, 11515–11529.
- 61 Y. Zhang, Q. Fu, B. Song and P. Xu, *Accounts Mater. Res.*, 2022, **3**, 1088–1100.
- 62 J. Jiang, Q. Liu, C. Zeng and L. Ai, *J. Mater. Chem. A*, 2017, **5**, 16929–16935.
- 63 J. Yin, J. Jin, H. Lin, Z. Yin, J. Li, M. Lu, L. Guo, P. Xi, Y. Tang and C. H. Yan, *Adv. Sci.*, 2020, **7**, 1903070.
- 64 L. Zhang, Q. Fan, K. Li, S. Zhang and X. Ma, *Sustain. Energy Fuels*, 2020, **4**, 5417–5432.
- 65 S. Chen, Y. Zhao, B. Sun, Z. Ao, X. Xie, Y. Wei and G. Wang, *ACS Appl. Mater. Interfaces*, 2015, **7**, 3306–3313.
- 66 Y. Meng, W. Song, H. Huang, Z. Ren, S. Y. Chen and S. L. Suib, *J. Am. Chem. Soc.*, 2014, **136**, 11452–11464.
- 67 H. Shi and G. Zhao, *J. Phys. Chem. C*, 2014, **118**, 25939–25946.
- 68 W. Xiong, H. Yin, T. Wu and H. Li, *Chem. - A Eur. J.*, 2023, **29**, e202202872.
- 69 C. G. Read, J. F. Callejas, C. F. Holder and R. E. Schaak, *ACS Appl. Mater. Interfaces*, 2016, **8**, 12798–12803.
- 70 Q. Kang, M. Li, J. Shi, Q. Lu and F. Gao, *ACS Appl. Mater. Interfaces*, 2020, **12**, 19447–19456.
- 71 Y. Wu, X. Chen, L. Su, Q. Wang and S. Ren, *New J. Chem.*, 2022, 6738–6741.
- 72 Y. Liu, N. Ran, R. Ge, J. Liu, W. Li, Y. Chen, L. Feng and R. Che, *Chem. Eng. J.*, 2021, **425**, 131642.
- 73 L. Yan, B. Zhang, S. Wu and J. Yu, *J. Mater. Chem. A*, 2020, **8**, 14234–14242.
- 74 B. Dutta, Y. Wu, J. Chen, J. Wang, J. He, M. Sharafeldin, P. Kerns, L. Jin, A.

- M. Dongare, J. Rusling and S. L. Suib, *ACS Catal.*, 2019, **9**, 456–465.
- 75 Y. Ge, S. P. Gao, P. Dong, R. Baines, P. M. Ajayan, M. Ye and J. Shen, *Nanoscale*, 2017, **9**, 5538–5544.
- 76 Z. Lin, C. Wang, Z. Wang, Q. Liu, C. Le, B. Lin and S. Chen, *Electrochim. Acta*, 2019, **294**, 142–147.
- 77 S. Gao, X. Wei, H. Fan, L. Li, K. Geng and J. Wang, *Nano Energy*, 2015, **13**, 518–526.
- 78 B. K. Kang, S. Y. Im, J. Lee, S. H. Kwag, S. Bin Kwon, S. N. Tiruneh, M. J. Kim, J. H. Kim, W. S. Yang, B. Lim and D. H. Yoon, *Nano Res.*, 2019, **12**, 1605–1611.
- 79 A. Sivanantham, S. Hyun, M. Son and S. Shanmugam, *Electrochim. Acta*, 2019, **312**, 234–241.
- 80 Y. Sakamaki, M. Tsuji, Z. Heidrick, O. Watson, J. Durchman, C. Salmon, S. R. Burgin and M. Hassan Beyzavi, *J. Chem. Educ.*, 2020, **97**, 1109–1116.
- 81 L. Chen, X. Zhang, X. Cheng, Z. Xie, Q. Kuang and L. Zheng, *Nanoscale Adv.*, 2020, **2**, 2628–2647.
- 82 H. Wang, Q. L. Zhu, R. Zou and Q. Xu, *Chem*, 2017, **2**, 52–80.
- 83 T. Qiu, Z. Liang, W. Guo, H. Tabassum, S. Gao and R. Zou, *ACS Energy Lett.*, 2020, **5**, 520–532.
- 84 Y. Peng, S. Sanati, A. Morsali and H. García, *Angew. Chemie - Int. Ed.*, 2023, **62**, e202214707.
- 85 H. F. Wang, L. Chen, H. Pang, S. Kaskel and Q. Xu, *Chem. Soc. Rev.*, 2020, **49**, 1414–1448.
- 86 X. Qin, D. Kim and Y. Piao, *Carbon Energy*, 2021, **3**, 66–100.

- 87 Z. Liang, R. Zhao, T. Qiu, R. Zou and Q. Xu, *EnergyChem*, 2019, **1**, 100001.
- 88 Z. Abbas, N. Hussain, I. Ahmed and S. M. Mobin, *Inorg. Chem.*, 2023, **62**, 8835–8845.
- 89 Q. Wang, Y. Song, D. Sun and L. Zhang, *ACS Omega*, 2021, **6**, 11077–11082.
- 90 E. Vijayakumar, S. Ramakrishnan, C. Sathiskumar, D. J. Yoo, J. Balamurugan, H. S. Noh, D. Kwon, Y. H. Kim and H. Lee, *Chem. Eng. J.*, 2022, **428**, 131115.
- 91 K. Srinivas, Y. Chen, X. Wang, B. Wang, M. Karpuraranjith, W. Wang, Z. Su, W. Zhang and D. Yang, *ACS Sustain. Chem. Eng.*, 2021, **9**, 1920–1931.
- 92 X. Luo, Q. Zhou, S. Du, J. Li, J. Zhong, X. Deng and Y. Liu, *ACS Appl. Mater. Interfaces*, 2018, **10**, 22291–22302.
- 93 Y. Cheng, J. Guo, Y. Huang, Z. Liao and Z. Xiang, *Nano Energy*, 2017, **35**, 115–120.
- 94 Y. Guo, J. Tang, H. Qian, Z. Wang and Y. Yamauchi, *Chem. Mater.*, 2017, **29**, 5566–5573.
- 95 M. Zhang, Q. Dai, H. Zheng, M. Chen and L. Dai, *Adv. Mater.*, 2018, **30**, 1–10.
- 96 L. Yang, L. Zhang, G. Xu, X. Ma, W. Wang, H. Song and D. Jia, *ACS Sustain. Chem. Eng.*, 2018, **6**, 12961–12968.
- 97 Z. Huang, S. Yuan, T. Zhang, B. Cai, B. Xu, X. Lu, L. Fan, F. Dai and D. Sun, *Appl. Catal. B Environ.*, 2020, **272**, 118976.
- 98 T. Chen, S. Li, J. Wen, P. Gui and G. Fang, *ACS Appl. Mater. Interfaces*, 2017, **9**, 35927–35935.
- 99 W. Li, B. Yu, Y. Hu, X. Wang, D. Yang and Y. Chen, *ACS Sustain. Chem. Eng.*, 2019, **7**, 4351–4359.

- 100 X. Liu, Y. Liu and L. Z. Fan, *J. Mater. Chem. A*, 2017, **5**, 15310–15314.
- 101 X. Sun, H. Huang, C. Wang, Y. Liu, T. L. Hu and X. H. Bu, *ChemElectroChem*, 2018, **5**, 3639–3644.
- 102 F. Ming, H. Liang, H. Shi, X. Xu, G. Mei and Z. Wang, *J. Mater. Chem. A*, 2016, **4**, 15148–15155.
- 103 Z. Zhang, S. Li, X. Bu, Y. Dai, J. Wang, X. Bao and T. Wang, *New J. Chem.*, 2021, **45**, 17313–17319.
- 104 R. K. Tripathy, A. Padhy, N. Sahu and J. N. Behera, *Sustain. Energy Fuels*, 2022, **6**, 4146–4152.

CHAPTER – 2

Metal–organic framework (MOF)-derived plate-shaped CoS_{1.097} nanoparticles for an improved hydrogen evolution reaction

2.1 Abstract

2.2 Introduction

2.3 Experimental Section

2.3.1 Materials

2.3.2 Synthesis of Co-MOF

2.3.3 Synthesis of CoS_{1.097}-160

2.3.4 Synthesis of bare CoS_x

2.4 Characterization

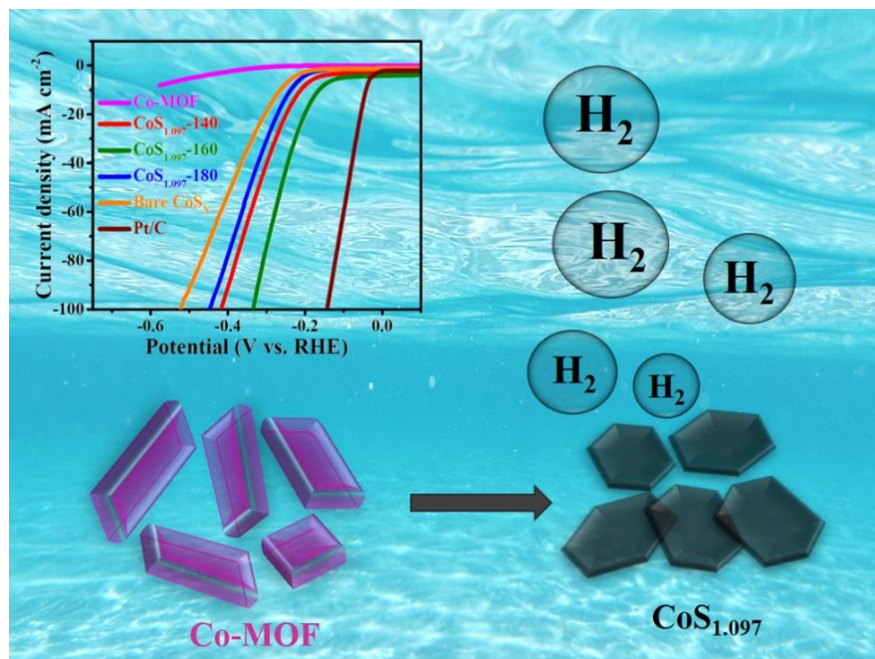
2.5 Electrochemical measurements

2.6 Results and discussion

2.7 Conclusions

2.8 References

2.1 Abstract



Metal–organic framework (MOF)-derived transition metal sulfides are viewed as reliable, cost-effective, and alternative hydrogen evolution reaction (HER)-efficient electrocatalysts. They have been used to replace platinum (and their alloys) for production of renewable energy carriers such as hydrogen. Progress towards development of non-precious transition-metal sulfides through different synthetic routes to obtain unique morphological nanostructures with enhanced HER activity is challenging. We introduced a transition-metal sulfide, cobalt sulfide ($\text{CoS}_{1.097}$), derived from a cobalt MOF [Co-BPY-DDE] by following facile, one-step solvothermal sulfurization. By varying the sulfurization temperature (from 140 °C to 180 °C) during the solvothermal method, three cobalt-sulfide products were obtained: $\text{CoS}_{1.097}$ -140, $\text{CoS}_{1.097}$ -160, and $\text{CoS}_{1.097}$ -180, respectively. Temperature variation had a vital role in optimizing the HER activity of the electrocatalyst. Besides, notable plate-shaped cobalt sulfide nanoparticles ($\text{CoS}_{1.097}$ -160) required overpotential of 163 mV to deliver a current density of 10 mA cm^{-2} with a low Tafel slope of 53 mV dec^{-1} , thereby

demonstrating faster reaction kinetics during the evolution of molecular hydrogen. Furthermore, 25 h of long-term stability of the electrocatalyst reflected its practical applicability in acidic media. CoS_{1.097}-160 had uniform plate-shaped morphology and large electrochemical active surface area, which contributed to enhanced electrochemical performance through water electrolysis.

2.2 Introduction

Global energy research has focused on carriers of renewable energy, such as hydrogen (H₂) and oxygen (O₂), because they do not result in a carbon byproduct.^{1,2} Different energy-storage and energy-conversion technologies, such as metal–air batteries, water-splitting devices, and fuel cells, have been developed. In fuel cells, molecular hydrogen and oxygen are used to generate electrical energy.^{3–5} Besides, water splitting is a simple path for hydrogen production in an eco-friendly way. However, the sluggish surface dynamics involved in the electrochemical process via water oxidation [oxygen evolution reaction (OER)] and reduction [hydrogen evolution reaction (HER)] restrict large-scale production. There is interest in preparing an effective electrocatalyst that can accelerate surface kinetics with increased hydrogen evolution with low overpotential.^{5,6} Until now, platinum-based precious materials and their alloys have been considered state-of-the-art electrocatalysts for the HER. The expense, scarcity, and poor durability of noble metals limits their industrial application. To reduce the liability associated with the electrocatalytic process and to search for an alternative efficient electrocatalyst, a broad range of cost-effective, non-precious transition metal-based oxides, sulfides, selenides, carbonitrides, phosphides, and borides have been used as HER electrocatalysts in acidic media.^{7–9} Transition-metal sulfides, especially cobalt sulfides (e.g., CoS₂, Co₃S₄, CoS, Co₉S₈, and their various heterostructures) and metal-

doped cobalt sulfides have been used to obtain enhanced HER performance.^{10–13} In addition, some derivatives of cobalt sulfides of the pyrite series of CoS₂ have been used due to their superior electrochemical performance (storage and conversion). They have unique structural features attributed to their metallic or semiconducting nature.^{14,15} However, bulk cobalt sulfide materials have elicited unsatisfactory hydrogen generation due to having few active sites and poor stability. The efficacy of a catalyst depends primarily upon having good electrical conductivity, along with a large active surface area and numerous active sites.^{16,17} In recent years, metal–organic frameworks (MOFs) have garnered much attention due to their porosity, high crystallinity, and enormous specific surface area.^{18–20} However, low electrical conductivity and poor chemical stability restrict use of pristine MOFs as electrode materials for electrocatalytic processes. In particular, MOFs can be used as suitable starting materials to synthesize highly efficient HER electrocatalysts due to a perfect metal cluster network and organic ligand blocks, which correspond to the synthesis of unique morphological structures with satisfactory electrochemical performances.^{21–24} Recently, Co-based MOFs based on secondary sulfurization or selenylation via chemical vapor deposition or hydro/solvothermal methods have been employed to develop unique metal sulfide/selenide nanostructured electrocatalysts for electrochemical water splitting.^{25–29} Extensive efforts have been made to synthesize specific cobalt-containing sulfide nanomaterials derived from MOF precursors by employing one-step sulfurization and studying their HER mechanism in acidic media. In particular, Co-MOFs and their derived functional CoS₂ materials have attracted much attention as stable electrocatalysts for the OER, HER, and as bifunctional catalysts for overall water electrolysis. Based on the various electrocatalytic applications of Co-MOF-derived CoS₂ electrode materials, Wang and colleagues

designed a novel hollow CoS₂ nanotube array from a MOF precursor, and used it as a bifunctional electrocatalyst supported over a carbon-cloth substrate.³⁰ Joo et al. reported gaseous sulfurization of Co-MOF, namely a cobalt Prussian blue analog (Co-PBA), to convert monophase CoS₂ nanoparticles, and studied their bifunctional electrocatalytic nature towards the overall water splitting process. The electrocatalyst required 196 mV of overpotential to reach a current density of 10 mA cm⁻² to catalyze the HER.³¹ Likewise, MOF-derived CoS₂ and various non-MOF-derived cobalt-based sulfide materials are frontline electrocatalysts in the energy sector (e.g., energy conversion and energy storage) because of their unique crystal phase, morphology-controlled synthesis, and modulation of their surface state.^{32–35} However, MOF-derived and non-MOF-derived cobalt sulfide electrode materials have limited ability to execute enhanced HER activity in acidic media. The HER performance of a cobalt sulfide electrocatalyst can be determined in an acidic electrolytic condition, where it needs a lower overpotential, better surface kinetics, and long-term stability. To overcome these obstacles, tremendous effort has been made to investigate a regular synthetic path and its temperature-dependent sulfurization to expand development of highly HER-efficient MOF-derived cobalt sulfide electrode materials.

Herein, we report a facile one-step solvothermal synthesis of CoS_{1.097} electrode material from a known Co-MOF precursor (Co-BPY-DDE) followed by sulfurization. This synthetic path includes a solvothermal reaction and “tuning” of the reaction temperature. We developed free-standing CoS_{1.097} nanoplates, represented as “CoS_{1.097}-160”, as promising electrocatalyst for improved HER performance through a water-splitting process. In particular, tuning of the sulfurization temperature plays a pivotal role in the synthesis of optimized HER-efficient cobalt sulfide (CoS_{1.097}-160) having a uniform morphological plate-shaped structure compared with that of other temperature

varied products (CoS_{1.097}-140 and CoS_{1.097}-180). The electrochemical HER performance revealed that the optimized plate-shaped cobalt sulfide (CoS_{1.097}-160) required only 163 mV of overpotential to reach the predefined current density of 10 mA cm⁻². In addition, the low Tafel slope of 53 mV dec⁻¹ demonstrated that the electrocatalyst followed the Volmer–Heyrovsky reaction path to execute the HER. Also, 25 h of a steady durability test of the material in the supporting acidic media indicated its practical applicability. Besides, the uniform plate-shaped morphological structure with a large electrochemical active surface area (ECSA) of the electrocatalyst contributed significantly to enhance HER activity.

2.3 Experimental section

2.3.1 Materials

Co(NO₃)₂·6H₂O, 2,2'-bipyridyl (BPY), 4,4'-dicarboxy diphenyl ether (DDE), sulfur powder, NaBH₄, N,N'-dimethylformamide (DMF), and Nafion solution were received from Sigma Aldrich, Himedia Chemicals and used without further purification. Deionized water (DI water) was used throughout the preparation of electrolyte solutions as well as washing of as-synthesized products.

2.3.2 Synthesis of Co-MOF

4,4'-Dicarboxy diphenyl ether and 2,2'-bipyridyl, as ligands, were used for the synthesis of the Co-MOF precursor by following a simple solvothermal method, as described previously.³⁶ Typically, 0.0645 g of 4,4'-dicarboxy diphenyl ether and 0.039 g of 2,2'-bipyridyl were added to a solution of deionized water (3 mL) and N,N'-dimethylformamide (DMF; 2 mL) with continuous stirring for 10 min. After that, 0.073 g of Co (NO₃)₂·6H₂O was added to the mixed solution and stirred further for 30 min. The obtained solution was transferred to a 23 mL Teflon-lined autoclave and heated in

a running oven at 145 °C for 2 days. After the autoclave had cooled down naturally to room temperature, products were collected and washed several times with DMF and ethanol.

2.3.3 Synthesis of CoS_{1.097}-160

First, 0.042 g of sulfur powder and 0.0215 g of NaBH₄ were dissolved in 6 mL of DMF and the resulting mixture stirred for 30 min. NaBH₄ was employed to reduce S to S²⁻. Furthermore, 0.0825 g of as-prepared Co-MOF was added to the black solution and stirring continued for 1 h. The final reaction mixture was transferred to a 23 mL Teflon-lined digestion bomb and sealed. Then, it was placed in a hot air oven at 160 °C for 1 day. The as-obtained black product was washed repeatedly with deionized water and ethanol through centrifugation and dried at 60 °C to procure CoS_{1.097}-160. For comparison, two more temperature-varied cobalt sulfide products were synthesized at 140 °C and 180 °C under similar reaction conditions and represented as CoS_{1.097}-140 and CoS_{1.097}-180, respectively.

2.3.4 Synthesis of bare CoS_x

Bare CoS_x was prepared by following the stepwise reaction process stated above using a cobalt nitrate hexahydrate precursor instead of Co-MOF as the starting material at 160 °C for 24 h.

2.4 Characterization

The phase purity of as-prepared samples was verified through a powder-diffraction system equipped with a diffractometer (D8 Advance; Bruker) with Cu-K α radiation ($\lambda = 1.5418 \text{ \AA}$). Morphological and elemental studies were undertaken with the help of a field emission scanning electron microscope (Merlin Compact) with a GEMINI-I

electron column (Zeiss) and a transmission electron microscope (2100F; JEOL) with an operating voltage of 200 kV. X-ray photoelectron spectroscopy (XPS) was operated using Versa Probe III (PHI) to further demonstrate the composition and chemical state of the material.

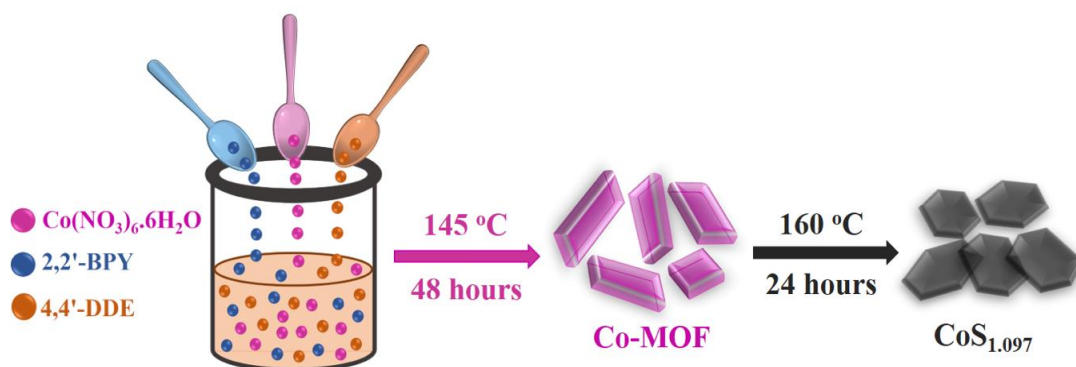
2.5 Electrochemical measurements

Electrochemical measurements with respect to the HER were recorded in a multi-channel three-electrode measurement system (Autolab PGSTAT100N; Metrohm). The electrolytic medium was H₂SO₄ solution (0.5 M). Preparation of electrocatalyst ink was carried out by mixing 1 mg of sample in a mixture of ethanol (95 μ L) and Nafion (5 μ L) followed by ultrasonication. The sample slurry-coated glassy-carbon electrode (GCE; mass loading of 0.25 mg cm⁻²) was used as the working electrode. A graphite rod electrode and aqueous Ag/AgCl electrode were used as the auxiliary electrode and reference electrode, respectively. HER activity was measured through linear sweep voltammetry (LSV) curves with an applied sweep rate of 5 mV s⁻¹. All electrochemical potentials were recorded with a standard aqueous Ag/AgCl reference electrode and calibrated to a reversible hydrogen electrode (RHE) according to the equation: $E_{\text{RHE}} = E_{(\text{Ag}/\text{AgCl})} + 0.0591 (\text{pH}) + 0.21 \text{ V}$. Electrochemical impedance spectroscopy (EIS) was undertaken at a potentiostatic mode of -0.19 V (vs. RHE) by supplying an AC amplitude of 5 mV on a frequency scale of 1 MHz to 0.1 Hz. In addition, the recorded LSVs were calculated and analyzed by iR compensation, where “ i ” represents the current and “ R ” is the solution resistance. To ascertain the surface kinetics associated with the HER, Tafel slopes were calculated by plotting the logarithm of current density (J) vs. overpotential from linear regions of LSVs by following the Tafel equation: $\eta = a + b \log J$ (where η is the overpotential, and a , b , and J are the Tafel constant, Tafel

slope, and current density, respectively). The double-layer capacitance (C_{dl}) of the used electrocatalyst was linearly correlated with the ECSA calculated from a specified potential window where an apparent Faradaic process was absent. Non-Faradaic cyclic voltammetry (CV) was carried out in a specific potential window of 0.31 V to 0.41 V (vs. RHE) at various scan rates (20 mV s^{-1} to 200 mV s^{-1}). The obtained plot between $\Delta J/2$ (half of the difference between the anodic current density and cathodic current density) and different scan rates gave a straight line, where the slope value corresponded to C_{dl} .^{37–39}

2.6 Results and discussion

The synthesis of Co-MOF-derived plate-shaped $\text{CoS}_{1.097}$ -160 nanoparticles involved a two-step synthetic procedure (**Scheme 2.1**).



Scheme 2.1: Stepwise reaction path for the synthesis of $\text{CoS}_{1.097}$ -160.

First, the Co-MOF precursor was synthesized via a solvothermal method using 4, 4'-DDE and 2,2'-BPY as ligands. The crystal structures of the Co-MOF are shown in **Figures 2.1a–d**. The cobalt cation was hexa-coordinated by four oxygen atoms of two different 4,4'-DDE ligands and two nitrogen atoms of the same 2,2'-BPY ligand, which formed a continuous one-dimensional (1D) chain, as shown in **Figures 2.1a and b**, respectively. The adjacent 1D chains were connected through H-bonding interactions

to form a 3D structure. The 1D and corresponding 3D structures are presented in **Figures 2.1c and d**.

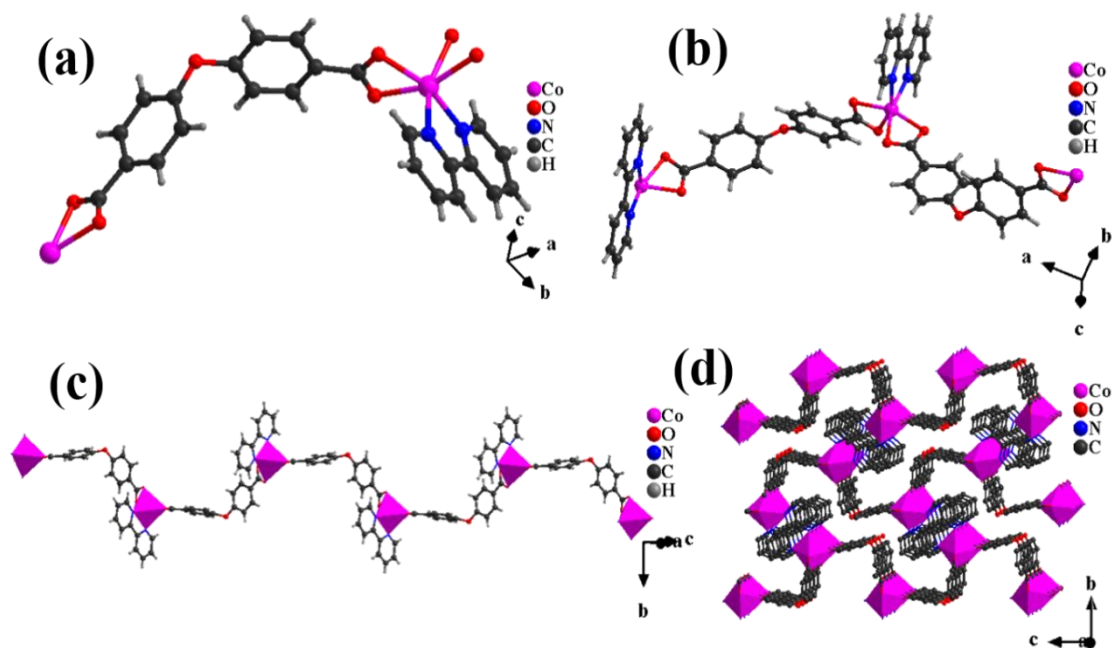


Figure 2.1: Crystal structures of Co-MOF (a-d).

In addition, the well-matched simulated and experimental powder pattern described the phase purity of the as-obtained Co-MOF precursor (**Figure 2.2a**). Furthermore, by adopting subsequent temperature-varied solvothermal sulfurization, cobalt sulfide nanoparticles were synthesized and termed as $\text{CoS}_{1.097-T}$ (T is the temperature of 140 °C, 160 °C, and 180 °C). The as-synthesized $\text{CoS}_{1.097-160}$ material was primarily characterized by powder X-ray diffraction (PXRD) pattern, which verified the phase purity (**Figure 2.2b**). PXRD depicted diffraction planes of (204), (220), (306), and (330), indexed to the hexagonal cobalt sulfide crystal system. These diffraction peaks were well supported by a data file (PDF 00-019-0366). In contrast, the powder diffraction of as-synthesized bare CoS_x revealed an amorphous phase (**Figure 2.2c**).

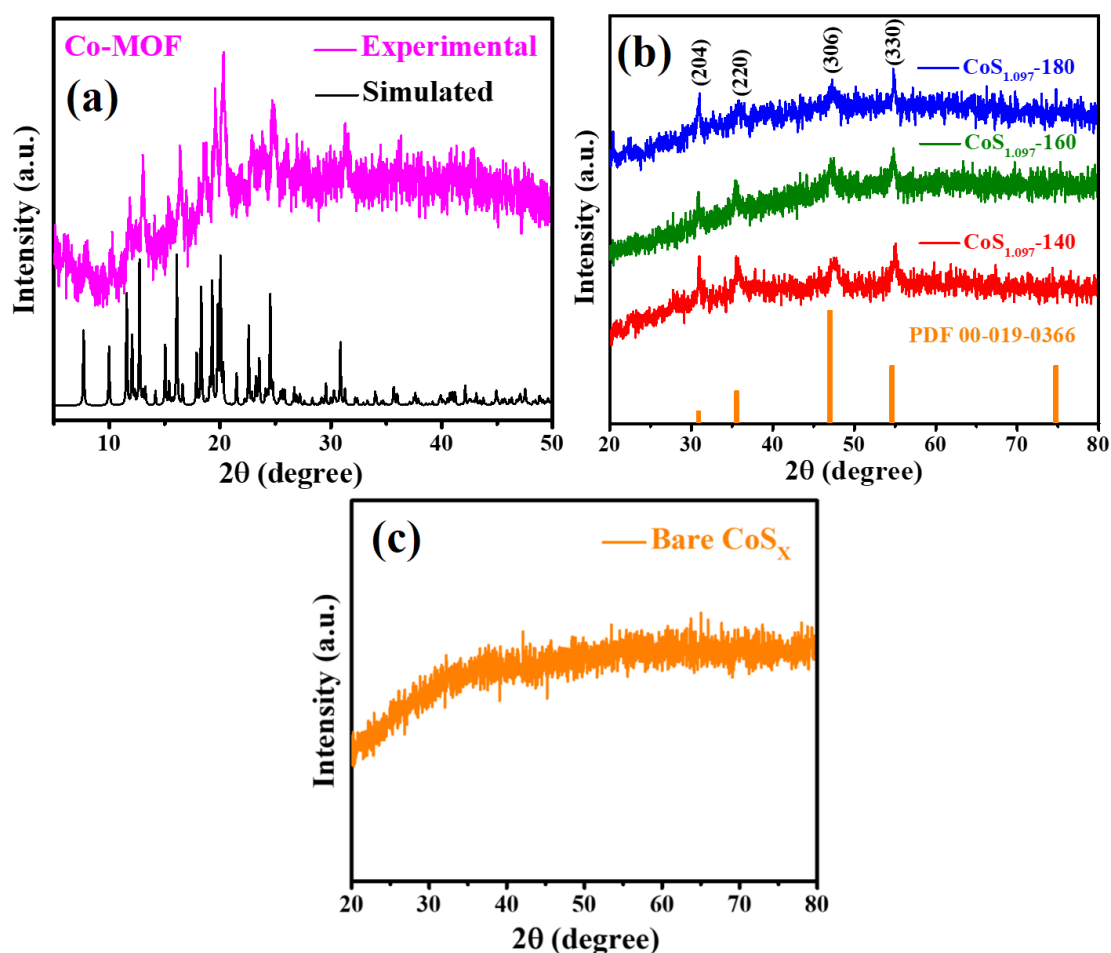


Figure 2.2: PXRD data of Co-MOF (a), $\text{CoS}_{1.097}$ -T products (b), and bare CoS_x (c).

The surface morphology of the pristine Co-MOF and its derived $\text{CoS}_{1.097}$ -160 electrocatalyst were discovered through scanning electron microscopy (SEM). SEM image of the Co-MOF precursor depicted a thick plate-shaped morphology as shown in **Figure 2.3**. After solvothermal sulfurization of Co-MOF at different temperatures, a nanoplate-shaped morphology was observed for all synthesized $\text{CoS}_{1.097}$ -T products ($T = 140\text{ }^\circ\text{C}$, $160\text{ }^\circ\text{C}$, and $180\text{ }^\circ\text{C}$). The morphology of the as-obtained products correlated directly with the different sulfurization temperature conditions of the electrocatalyst. At the optimized temperature condition of $160\text{ }^\circ\text{C}$, the as-synthesized cobalt sulfide ($\text{CoS}_{1.097}$ -160) displayed a hexagonal plate-shaped morphology. Uniform distribution of hexagonal nanoplates was observed at different magnifications (**Figure 2.4**).

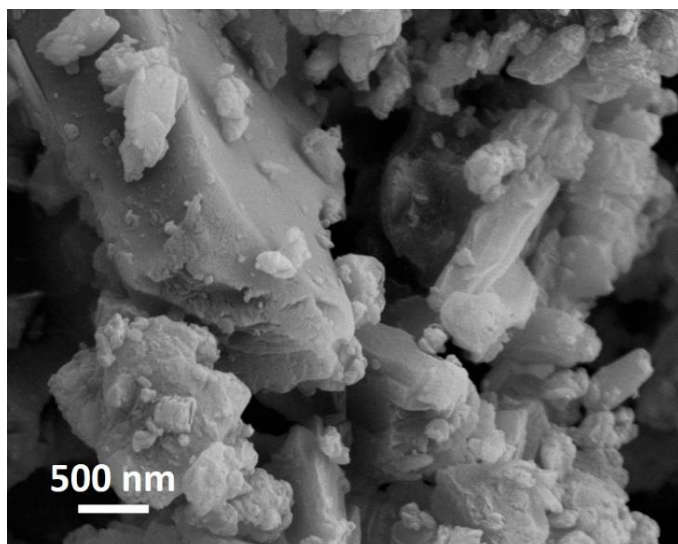


Figure 2.3: SEM analysis of Co-MOF.

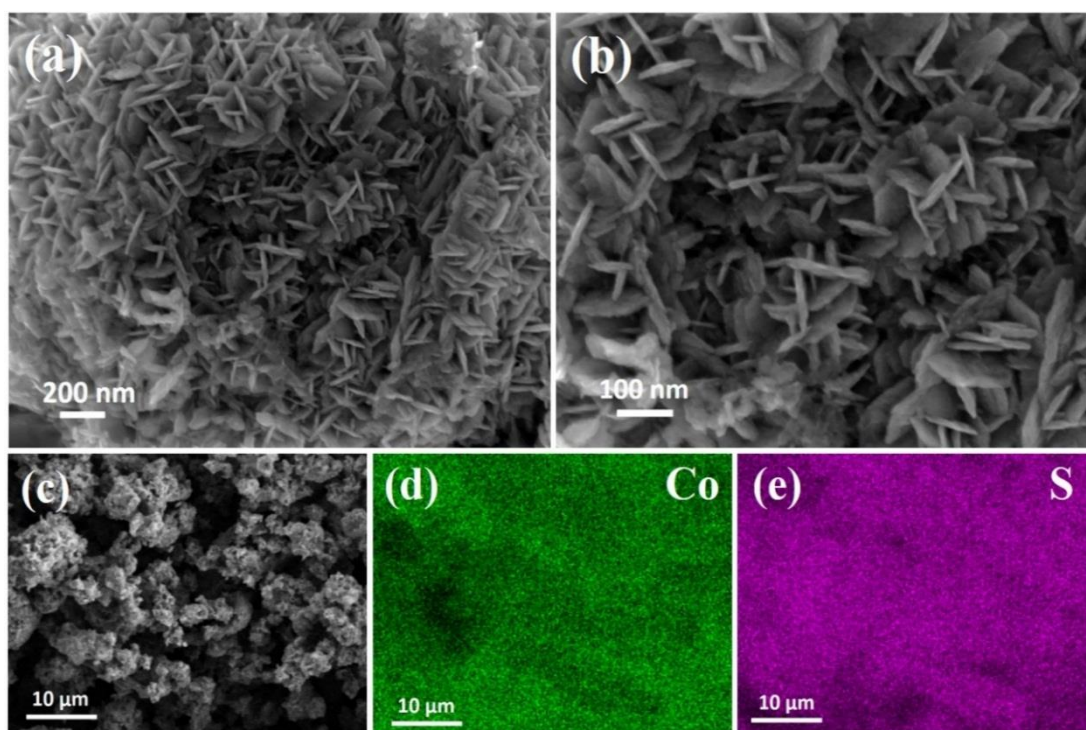


Figure 2.4: SEM images of $\text{CoS}_{1.097-160}$ at different magnifications (a and b) and elemental mapping of $\text{CoS}_{1.097-160}$ (c–e).

However, in the case of $\text{CoS}_{1.097-140}$, the growth of hexagonal nanoplates was partially restricted, which might have been due to incomplete sulfurization at 140 °C (**Figures**

2.5a and b). With an increase in temperature to 180 °C, agglomeration of the plate-shaped morphology was observed (**Figures 2.5c and d**).

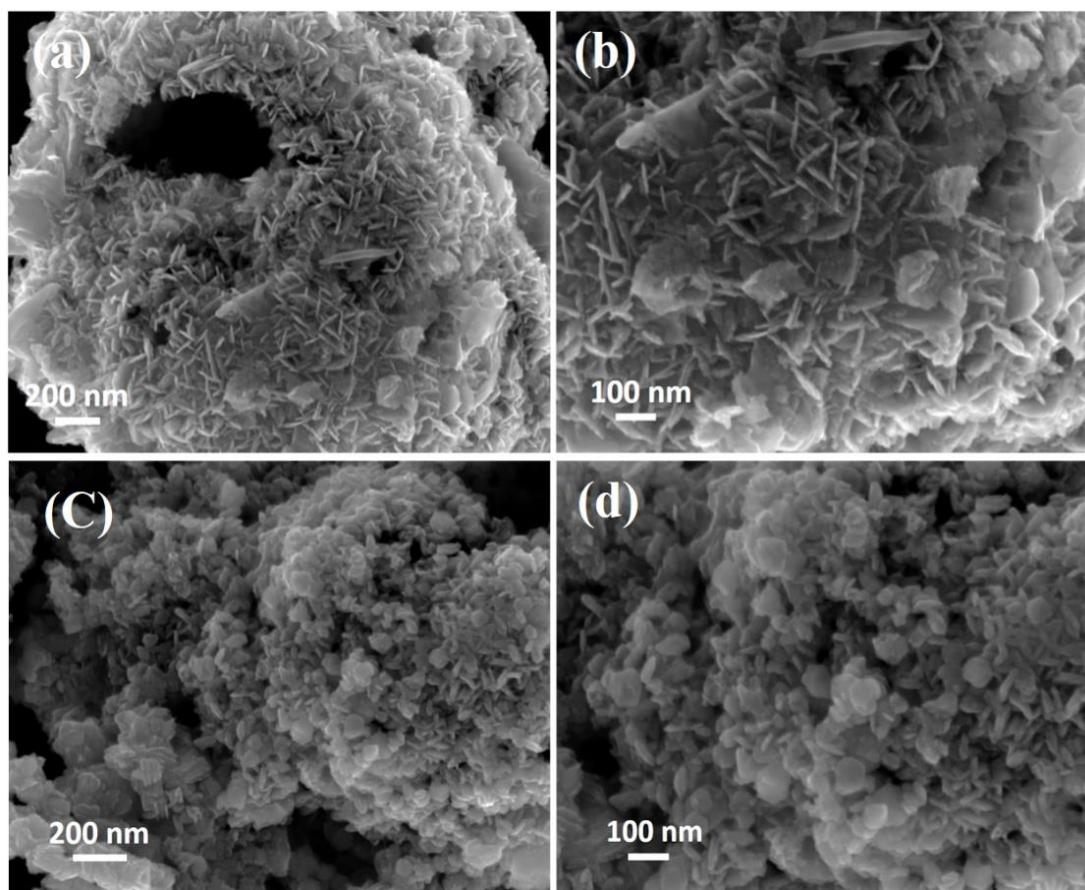


Figure 2.5: SEM images of $\text{CoS}_{1.097-140}$ (a and b), and $\text{CoS}_{1.097-180}$ at different magnifications (c and d).

Furthermore, the plate-shaped morphology and its uniform distribution were examined by transmission electron microscopy (TEM) at different magnifications (**Figures 2.6a and b**). **Figure 2.6c** reveals that the nanoplates were, in general, hexagonal. High-resolution transmission electron microscopy (HRTEM) confirmed the existence of a distinct lattice fringe with calculated d-spacing value of 0.25 nm, which was attributed to the (220) plane of the hexagonal crystal system of $\text{CoS}_{1.097}$ nanoparticles (**Figure 2.6d**). HRTEM data were consistent with the observed PXRD data. The inset picture in **Figure 2.6b** is the selected area electron diffraction (SAED) pattern of $\text{CoS}_{1.097-160}$.

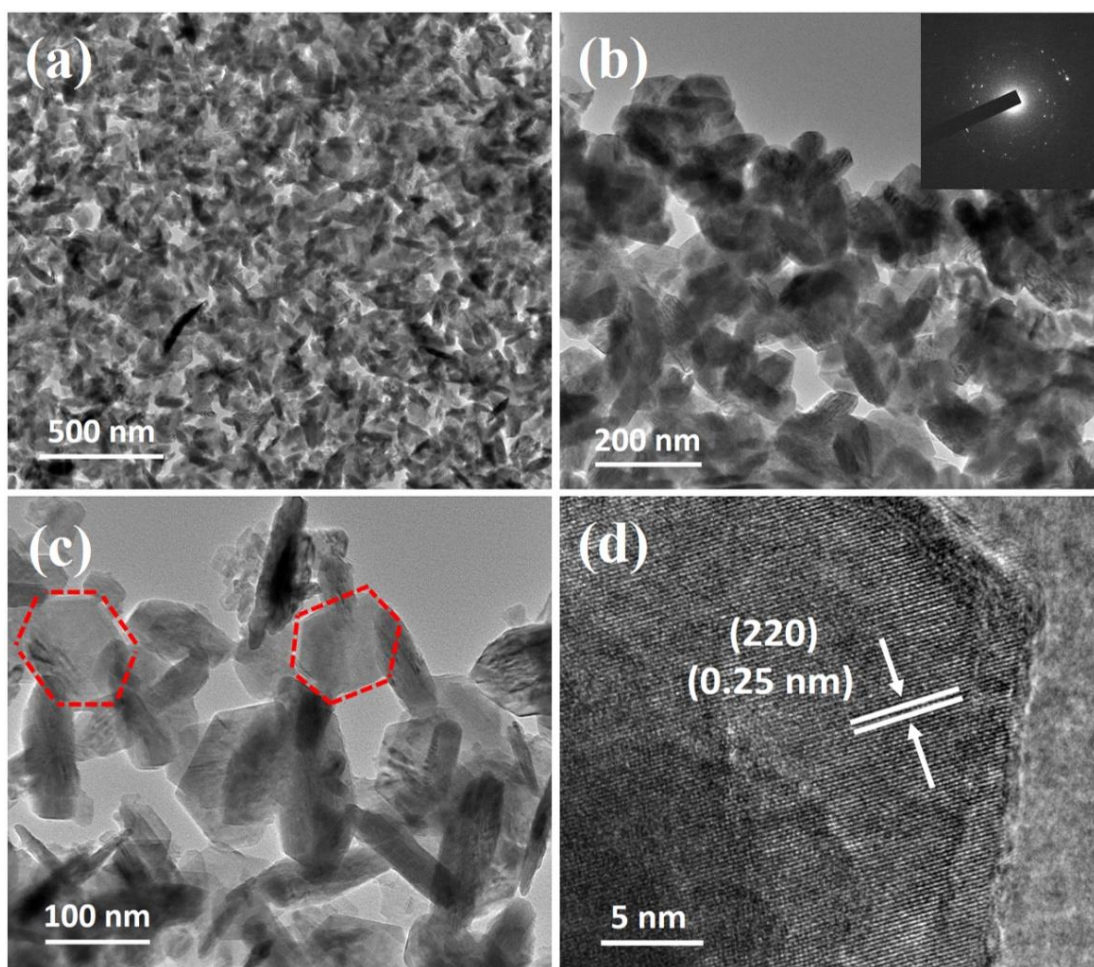


Figure 2.6: TEM of $\text{CoS}_{1.097}$ -160 at different magnifications (a and b), high-resolution TEM of $\text{CoS}_{1.097}$ -160 (c and d), inset in (b) is the selected area electron diffraction (SAED) pattern.

XPS verified the elemental state and actual chemical composition of as-prepared $\text{CoS}_{1.097}$ -160 nanoparticles. **Figure 2.7a** displays the XPS survey spectrum: Co, S, C, and O are present. The oxygen peak shows the availability of oxidized species of the sample in contact with air.^{40,41} The Co 2p spectrum of the temperature-optimized sample exhibited two doublets (**Figure 2.7b**). The observed peak positions of Co $2p_{3/2}$ and Co $2p_{1/2}$ at 779.5 and 794.4 eV represent Co^{3+} , whereas the characteristic peak positions at 781.8 and 797.9 eV show the existence of Co $2p_{3/2}$ and Co $2p_{1/2}$ of Co^{2+} , suggesting the presence of Co^{2+} and Co^{3+} species. Two satellite peaks are obtained at

the binding energy of 786.1 and 804.4 eV.^{41–43} Furthermore, the S 2p spectrum of $\text{CoS}_{1.097-160}$ depicts a peak centered at a binding energy of 159.8 eV, which corresponds with $\text{CoS}_{1.097}$ or the Co-deficient nonstoichiometric sulfide species in **Figure 2.7c**. The associated peak positions at the binding energies of 162.6 and 165.2 eV can be assigned to S 2p_{3/2} and S 2p_{1/2}, respectively.^{44,45}

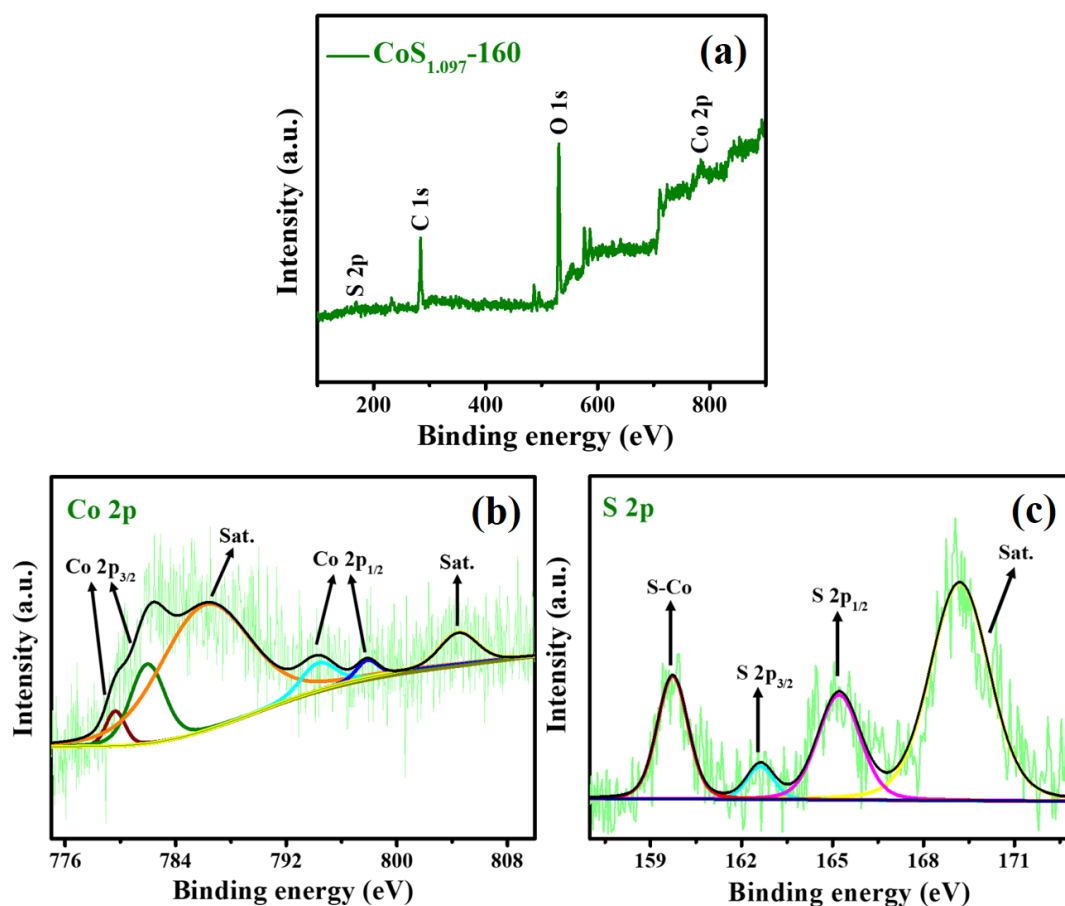


Figure 2.7: Full scan XPS spectra (a) and deconvoluted XPS spectra of Co 2p (b) and S 2p (c).

The electrochemical results corresponded to the HER performances of the cobalt MOF and temperature-varied cobalt sulfide products, which were termed $\text{CoS}_{1.097-T}$ ($T = 140$ °C, 160 °C, and 180 °C) and studied using a multichannel three-electrode configuration in acidic electrolytic media (0.5 M H_2SO_4). In addition, LSV of Pt/C and bare CoS_x was done to compare the overall HER performance. **Figure 2.8** shows the iR -

compensated LSV curves for CoS_{1.097}-140, CoS_{1.097}-160, CoS_{1.097}-180, bare CoS_X, and the standard Pt/C recorded at a scan rate of 5 mV s⁻¹. The Co-MOF precursor exhibited poor HER performance. However, among different temperature-varied cobalt sulfide products, CoS_{1.097}-160 showed stronger HER activity in terms of lower overpotential (163 mV) to reach the standard cathodic current density of 10 mA cm⁻² (**Figure 2.9a**). The as-obtained overpotential of CoS_{1.097}-160 was much lower than that of CoS_{1.097}-140 (211 mV), CoS_{1.097}-180 (236 mV), and bare CoS_X (262 mV), along with various reported sulfide materials shown in **Table 2.1**. **Figure 2.9b** displays a comparison of overpotential of CoS_{1.097}-T products with different synthesis temperatures.

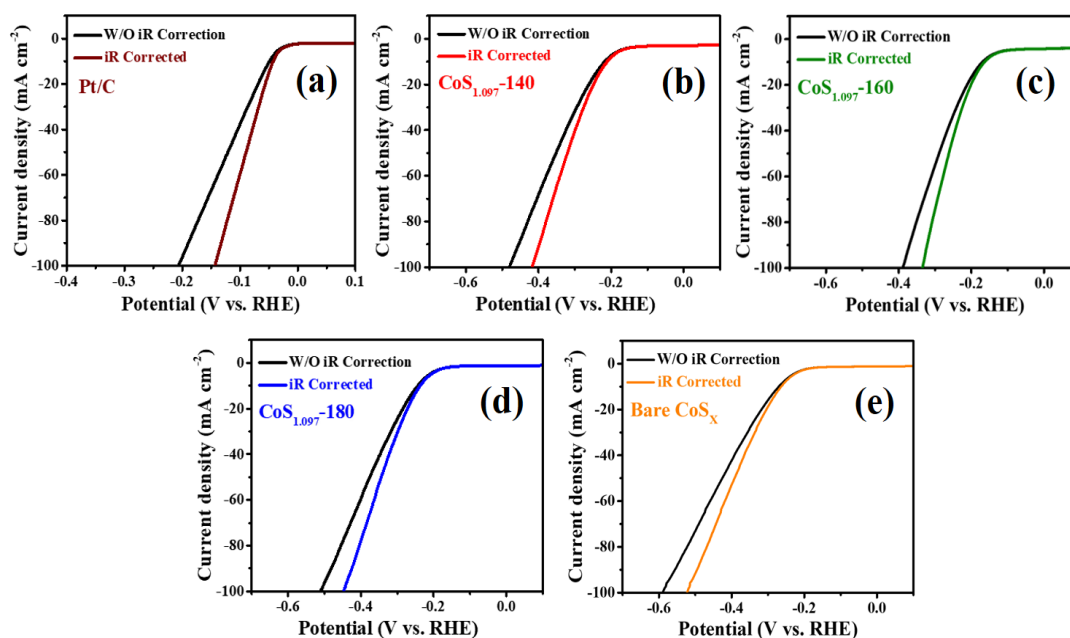


Figure 2.8: Polarization curves of CoS_{1.097}-T products, Pt/C and bare CoS_X before and after *iR* compensation.

The actual surface reaction kinetics were verified from the obtained LSV data known as the Tafel plot.⁴⁶ CoS_{1.097}-160 had a lower Tafel slope (53 mV dec⁻¹), which demonstrated faster surface kinetics resulting in improved HER performance.^{47,48} The calculated Tafel slope (in mV dec⁻¹) was lower than that of the other as-prepared products, such as CoS_{1.097}-140 (64), CoS_{1.097}-180 (69), and bare CoS_X (77).

Furthermore, the Tafel slope of precious Pt/C (31 mV dec^{-1}) was used to compare the Tafel slope of the as-prepared non-precious cobalt sulfide products (**Figure 2.9c**). EIS was employed at -0.19 V vs. RHE to investigate the charge transfer process of as-synthesized HER electrocatalysts. **Figure 2.9d** shows the EIS of bare CoS_x and $\text{CoS}_{1.097}\text{-T}$ products. $\text{CoS}_{1.097}\text{-160}$ showed a smaller arc diameter, which corresponded to a lower charge transfer resistance (R_{CT}) of 57Ω in comparison with that of $\text{CoS}_{1.097}\text{-140}$ (128Ω), $\text{CoS}_{1.097}\text{-180}$ (161Ω), and bare CoS_x (337Ω). A lower R_{CT} indicates faster electron diffusion between the used electrode surface and supporting electrolyte, thereby resulting in stronger HER activity.^{49,50} The inset in **Figure 2.9d** is the fitted equivalent circuit diagram obtained from the EIS result.

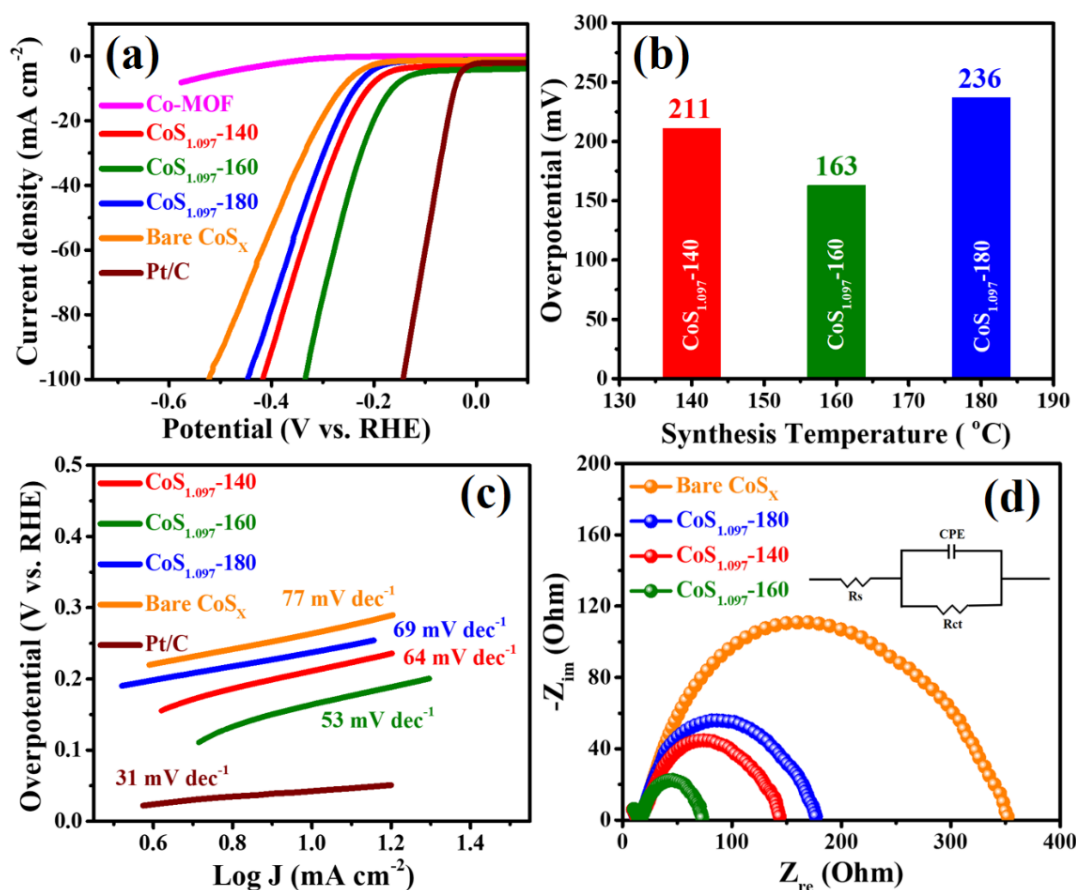


Figure 2.9: LSVs of Co-MOF, $\text{CoS}_{1.097}\text{-T}$ products, bare CoS_x , and Pt/C (a). Comparison of overpotential of $\text{CoS}_{1.097}\text{-T}$ products at 10 mA cm^{-2} current density (b). Tafel slopes of $\text{CoS}_{1.097}\text{-T}$ products, bare CoS_x , and Pt/C (c). PEIS comparison at -0.19 V vs. RHE of $\text{CoS}_{1.097}\text{-T}$ products and bare CoS_x (d). Inset in (d) is the equivalent circuit diagram.

Insights into the electrocatalytic activity of the electrocatalyst were obtained with the ECSA. However, ECSA has a direct relationship with the C_{dl} of the electrocatalyst, and is applied to calculate the accessible units of electrochemical active sites.^{22,37} The C_{dl} is estimated from a specific non-Faradaic potential window through a standard CV method.⁵¹ **Figure 2.10a** represents the non-Faradaic CV of CoS_{1.097}-160, where the desired current arises due to charge accumulation. CV in a non-Faradaic potential window of CoS_{1.097}-140, CoS_{1.097}-180, and bare CoS_x is presented in **Figure 2.11**. C_{dl} values were calculated by plotting different scan rates versus half of the difference between the anodic current density and cathodic current density ($\Delta J = J_a - J_c$) at 0.36 V vs. RHE. The C_{dl} of CoS_{1.097}-160 was found to be 4.21 mF cm⁻², which was higher than that of the other temperature-varied cobalt sulfide products, such as CoS_{1.097}-140 (2.97 mF cm⁻²), CoS_{1.097}-180 (2.14 mF cm⁻²), and also the bare CoS_x (1.06 mF cm⁻²) (**Figure 2.10b**).

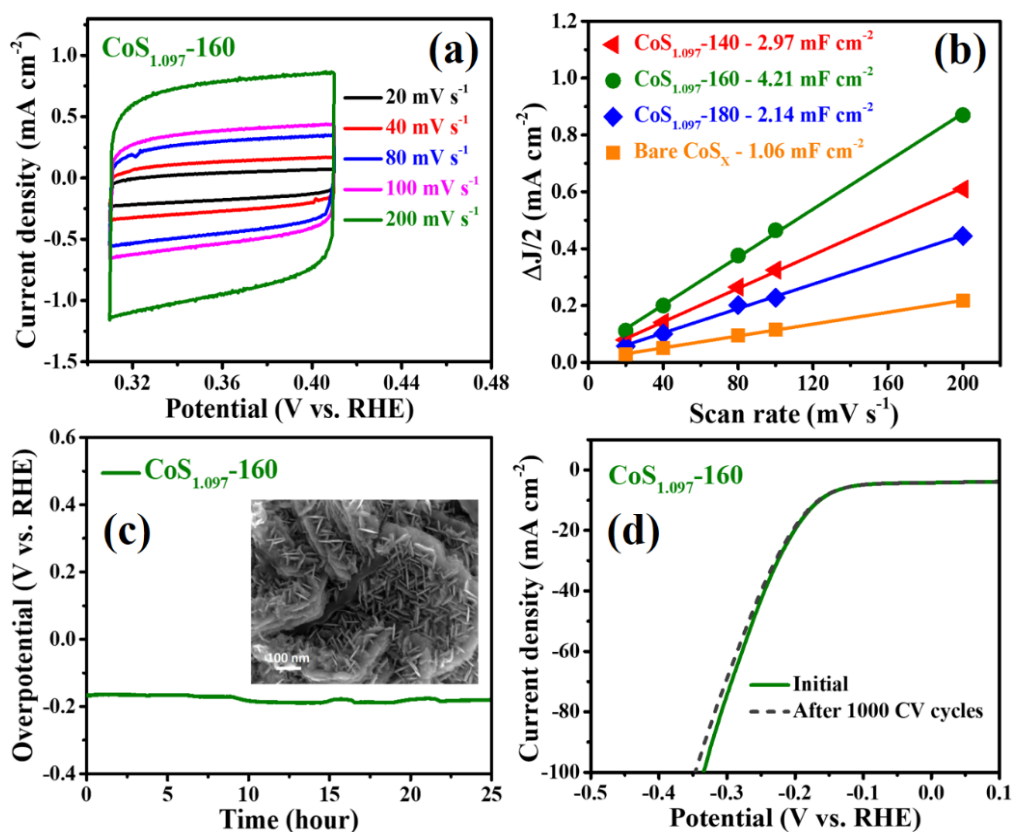


Figure 2.10: CV of CoS_{1.097}-160 in a potential window of 0.31 to 0.41 V vs. RHE (a). Estimated C_{dl} of CoS_{1.097}-T products and bare CoS_x at 0.36 V vs. RHE (b). Stability test of CoS_{1.097}-160 in an acidic solution (c). LSVs of CoS_{1.097}-160 before and after 1000 CV cycles (d). Inset in (c) is the SEM image of CoS_{1.097}-160 after 25 h of the constant durability test.

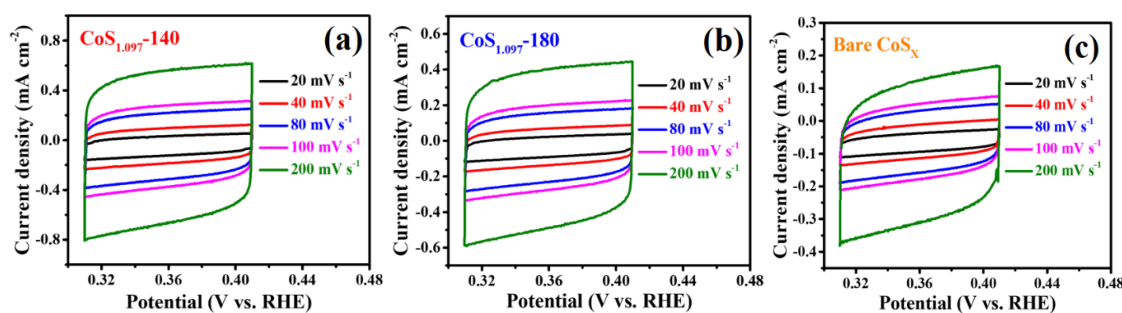


Figure 2.11: Cyclic voltammograms (CVs) of $\text{CoS}_{1.097-140}$ (a), $\text{CoS}_{1.097-180}$ (b) and bare CoS_x (c) in a non-Faradaic potential region of 0.31 V vs. RHE to 0.41 V vs. RHE.

The optimized temperature condition for the synthesis of the $\text{CoS}_{1.097}$ product had a significant role in regulating its well-organized hexagonal plate-shaped morphology, with a higher ECSA (which might have been responsible for the improved HER results).^{16,17} Furthermore, the chronopotentiometry test was carried out to estimate the practical applicability of the HER-active $\text{CoS}_{1.097-160}$ electrocatalyst (**Figure 2.10c**). The electrocatalyst was very stable up to 25 h of constant electrolysis, with a negligible increase in overpotential at a constant current density of 10 mA cm^{-2} , signifying excellent electrochemical durability in an acidic solution.^{42,52} In addition, the initial and final polarization curves after 1000 CV cycles showed minimal change in overpotential, thereby indicating the outstanding stability of the electrocatalyst (**Figure 2.10d**).⁵³ Furthermore, post-stability characterization using PXRD and field emission scanning electron microscopy verified the material's phase and morphology, but was also used to understand the actual surface catalytic behaviour of the as-prepared material. **Figure 2.12** shows the post-stability powder pattern of the material, which demonstrated no significant changes in the phase of $\text{CoS}_{1.097-160}$. However, the plate-shaped morphology of the temperature-optimized cobalt sulfide sample suffered negligible surface distortion (inset of **Figure 2.10c**) after continuous electrolysis in an acidic electrolytic medium.

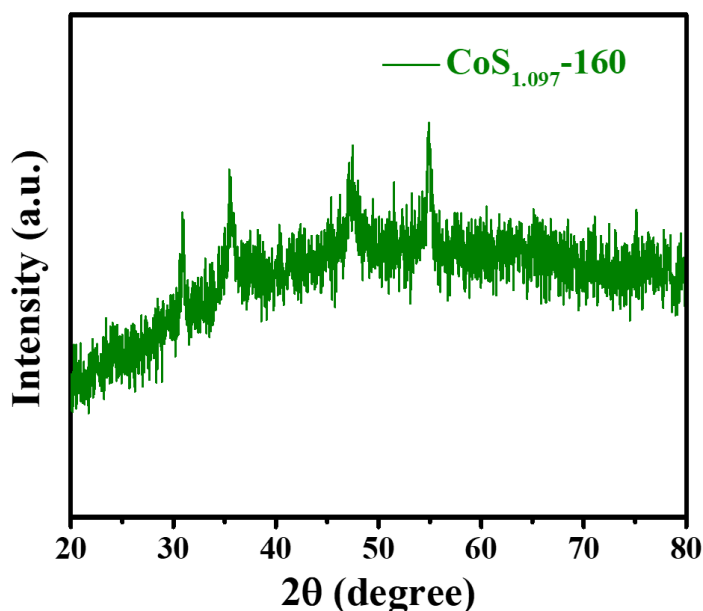


Figure 2.12: PXRD study of $\text{CoS}_{1.097}$ -160 after chronopotentiometry measurement of 25 h at 10 mA cm^{-2} current density under acidic electrolytic conditions.

The outstanding catalytic activity and durability of the electrocatalyst could be attributed to the nanoplate-like architecture that provided structural integrity and exposed a sufficient number of active sites to promote smooth contact of the electrocatalyst with the electrolyte solution. The temperature regulated the morphology. Under the optimized temperature condition, the uniformity in morphology triggered the availability of a sufficient number of active sites to improve the catalytic behaviour towards the HER. The systematic characterization stated above and the improved electrochemical results of the distinct cobalt sulfide phase ($\text{CoS}_{1.097}$ -160) suggest that it could be a substitute HER electrocatalyst in comparison with noble metals. Our work provides a new way to design non-precious MOF-derived electrocatalysts for electrochemical applications.

Table 2.1: Hydrogen evolution reaction (HER) comparison of cobalt sulfide-based electrocatalysts.

Electrocatalyst	Overpotential at 10 mA cm ⁻² (mV)	Tafel slope (mV dec ⁻¹)	Electrolyte	References
$\text{CoS}_{1.097}/\text{MoS}_2$	228	59.7	0.5 M H_2SO_4	ACS Appl. Energy Mater. 2019, 2, 10, 7504–7511
CoP-CoS composite nanorods	156	74	0.5 M H_2SO_4	ChemCatChem 2019, 11, 6099–6104
$\text{MoS}_2/\text{Co}_3\text{S}_4$	175	55.6	0.5 M H_2SO_4	Electrochim. Acta 2018, 269, 262–273
CoS_2	192	52	0.5 M H_2SO_4	J. Phys. Chem. C. 2014, 118, 21347–21356.
CoS_2	165	86.57	0.5 M H_2SO_4	ACS Appl. Mater. Interfaces 2021, 13, 41573–41583
Ni-doped CoS_2	156	52	0.5 M H_2SO_4	Electrochim. Acta, 2017, 228, 428-435
CoS_2/CC	288	210.7	0.5 M H_2SO_4	J. Mater. Chem. A, 2015, 3, 22886-22891
CoS_2 microwires	158	58	0.5 M H_2SO_4	J. Am. Chem. Soc., 2014, 136,10053-10061
Co_xS_y	188	96	0.5 M H_2SO_4	ChemElectroChem 2018, 5, 3639–3644
$\text{CoS}-\text{MoS}_2$	270	74	0.5 M H_2SO_4	J. Solid State Electrochem. 2017, 21, 409–417
$\text{CoS}_{1.097-160}$	163	53	0.5 M H_2SO_4	This Work

2.7 Conclusions

We synthesized a series of temperature-varied cobalt sulfide nanoparticles ($\text{CoS}_{1.097-140}$, $\text{CoS}_{1.097-160}$, and $\text{CoS}_{1.097-180}$) by using a Co-MOF as the precursor. An optimized cobalt sulfide ($\text{CoS}_{1.097-160}$) displayed uniform and organized plate-shaped morphology. The latter corresponded to a larger ECSA that enhanced the overall HER performance. $\text{CoS}_{1.097-160}$ needed a lower overpotential of 163 mV to deliver a current density of 10 mA cm⁻² and a small Tafel slope of 53 mV dec⁻¹ compared with the other

as-prepared cobalt sulfide products (CoS_{1.097}-140 and CoS_{1.097}-180). The outstanding 25 h long-term durability test with negligible change in overpotential indicated its remarkable HER performance. We provide an optimized temperature-dependent strategy for the synthesis of Co-MOF-derived cobalt sulfides as replaceable and cost-effective HER electrocatalysts in comparison with noble metal-based catalysts and their alloys for electrocatalytic hydrogen evolution.

2.8 References

- 1 M. S. Faber and S. Jin, *Energy Environ. Sci.*, 2014, **7**, 3519–3542.
- 2 Y. Jiao, Y. Zheng, M. Jaroniec and S. Z. Qiao, *Chem. Soc. Rev.*, 2015, **44**, 2060–2086.
- 3 S. Ghosh and R. N. Basu, *Nanoscale*, 2018, **10**, 11241–11280.
- 4 I. Katsounaros, S. Cherevko, A. R. Zeradjanin and K. J. J. Mayrhofer, *Angew. Chemie - Int. Ed.*, 2014, **53**, 102–121.
- 5 M. Zeng and Y. Li, *J. Mater. Chem. A*, 2015, **3**, 14942–14962.
- 6 X. Li, X. Hao, A. Abudula and G. Guan, *J. Mater. Chem. A*, 2016, **4**, 11973–12000.
- 7 J. Zhu, L. Hu, P. Zhao, L. Y. S. Lee and K. Y. Wong, *Chem. Rev.*, 2020, **120**, 851–918.
- 8 J. Huang, Y. Jiang, T. An and M. Cao, *J. Mater. Chem. A*, 2020, **8**, 25465–25498.
- 9 D. Siegmund, N. Blanc, M. Smialkowski, K. Tschulik and U. P. Apfel, *ChemElectroChem*, 2020, **7**, 1514–1527.
- 10 W. Xing, Y. Zhang, Q. Xue and Z. Yan, *Nanoscale Res. Lett.*, 2015, **10**, 1–6.
- 11 X. Zhu, J. Dai, L. Li, D. Zhao, Z. Wu, Z. Tang, L.-J. Ma and S. Chen, *Carbon N. Y.*, 2020, **160**, 133–144.

- 12 L. Wang, X. Wu, S. Guo, M. Han, Y. Zhou, Y. Sun, H. Huang, Y. Liu and Z. Kang, *J. Mater. Chem. A*, 2017, **5**, 2717–2723.
- 13 D. Dong, Z. Wu, J. Wang, G. Fu and Y. Tang, *J. Mater. Chem. A*, 2019, **7**, 16068–16088.
- 14 B. Dutta, Y. Wu, J. Chen, J. Wang, J. He, M. Sharafeldin, P. Kerns, L. Jin, A. M. Dongare, J. Rusling and S. L. Suib, *ACS Catal.*, 2019, **9**, 456–465.
- 15 W. Zhang, X. Ma, C. Zhong, T. Ma, Y. Deng, W. Hu and X. Han, *Front. Chem.*, 2018, **6**, 1–10.
- 16 N. Sahu, J. K. Das and J. N. Behera, *Sustain. Energy Fuels*, 2021, **5**, 4992–5000.
- 17 A. Zhao, G. Xu, Y. Li, J. Jiang, C. Wang, X. Zhang, S. Zhang and L. Zhang, *Inorg. Chem.*, 2020, **59**, 12778–12787.
- 18 X. Wang, W. Zhang, Q. Yu, X. Liu, Q. Liang, X. Meng, X. Wang and L. Wang, *Chem. Eng. J.*, 2022, **446**, 136987.
- 19 Z. Ye, Y. Jiang, L. Li, F. Wu and R. Chen, *Adv. Mater.*, 2022, **34**, 1–11.
- 20 C. Chen, A. Wu, H. Yan, Y. Xiao, C. Tian and H. Fu, *Chem. Sci.*, 2018, **9**, 4746–4755.
- 21 T. Qiu, Z. Liang, W. Guo, H. Tabassum, S. Gao and R. Zou, *ACS Energy Lett.*, 2020, **5**, 520–532.
- 22 T. Chen, S. Li, J. Wen, P. Gui and G. Fang, *ACS Appl. Mater. Interfaces*, 2017, **9**, 35927–35935.
- 23 R. R. Salunkhe, Y. V. Kaneti and Y. Yamauchi, *ACS Nano*, 2017, **11**, 5293–5308.
- 24 X. Wen and J. Guan, *Appl. Mater. Today*, 2019, **16**, 146–168.

- 25 K. Ao, J. Dong, C. Fan, D. Wang, Y. Cai, D. Li, F. Huang and Q. Wei, *ACS Sustain. Chem. Eng.*, 2018, **6**, 10952–10959.
- 26 X. Liu, Y. Liu and L. Z. Fan, *J. Mater. Chem. A*, 2017, **5**, 15310–15314.
- 27 L. Yang, L. Zhang, G. Xu, X. Ma, W. Wang, H. Song and D. Jia, *ACS Sustain. Chem. Eng.*, 2018, **6**, 12961–12968.
- 28 H. Zou, B. He, P. Kuang, J. Yu and K. Fan, *ACS Appl. Mater. Interfaces*, 2018, **10**, 22311–22319.
- 29 N. Yao, T. Tan, F. Yang, G. Cheng and W. Luo, *Mater. Chem. Front.*, 2018, **2**, 1732–1738.
- 30 C. Guan, X. Liu, A. M. Elshahawy, H. Zhang, H. Wu, S. J. Pennycook and J. Wang, *Nanoscale Horizons*, 2017, **2**, 342–348.
- 31 I. K. Ahn, W. Joo, J. H. Lee, H. G. Kim, S. Y. Lee, Y. Jung, J. Y. Kim, G. B. Lee, M. Kim and Y. C. Joo, *Sci. Rep.*, 2019, **9**, 1–10.
- 32 J. Wang, N. Wu, L. Han, C. Liao, X. Mu, Y. Kan and Y. Hu, *J. Colloid Interface Sci.*, 2021, **581**, 552–565.
- 33 C. Feng, Z. Li, J. Wang, T. Yan, H. Dong, J. Feng, Q. Zhang, J. Sui, L. Yu and L. Dong, *J. Electroanal. Chem.*, 2019, **840**, 27–34.
- 34 H. B. M. Sidek, X. Jin, M. S. Islam and S. J. Hwang, *ChemCatChem*, 2019, **11**, 6099–6104.
- 35 L. Wu, K. Zhang, T. Wang, X. Xu, Y. Zhao, Y. Sun, W. Zhong and Y. Du, *ACS Appl. Nano Mater.*, 2018, **1**, 1083–1093.
- 36 W. Bai, G. Qin, J. Wang, L. Li and Y. Ni, *Dye. Pigment.*, 2021, **193**, 109473.

-
- 37 N. Sahu, J. K. Das and J. N. Behera, *Inorg. Chem.*, 2022, **61**, 2835–2845.
- 38 J. K. Das, A. K. Samantara, S. Satyarthi, C. S. Rout and J. N. Behera, *RSC Adv.*, 2020, **10**, 4650–4656.
- 39 S. Xu, J. Xu, Y. Z. Liu, Y. Hua, Z. Duan, Y. Wang, A. Neville and X. Gao, *ACS Appl. Energy Mater.*, 2019, **2**, 8974–8984.
- 40 X. Ma, W. Zhang, Y. Deng, C. Zhong, W. Hu and X. Han, *Nanoscale*, 2018, **10**, 4816–4824.
- 41 X. Sun, H. Huang, C. Wang, Y. Liu, T. L. Hu and X. H. Bu, *ChemElectroChem*, 2018, **5**, 3639–3644.
- 42 J. Sun, Z. Huang, T. Huang, X. Wang, X. Wang, P. Yu, C. Zong, F. Dai and D. Sun, *ACS Appl. Energy Mater.*, 2019, **2**, 7504–7511.
- 43 Y. Zhao, J. Wang, L. Zheng, P. Sun, N. Huang, X. Huang and X. Sun, *J. Nanoparticle Res.*, 2019, **21**, 1–12.
- 44 F. Cao, M. Zhao, Y. Yu, B. Chen, Y. Huang, J. Yang, X. Cao, Q. Lu, X. Zhang, Z. Zhang, C. Tan and H. Zhang, *J. Am. Chem. Soc.*, 2016, **138**, 6924–6927.
- 45 H. Liang, D. Jiang, S. Wei, X. Cao, T. Chen, B. Huo, Z. Peng, C. Li and J. Liu, *J. Mater. Chem. A*, 2018, **6**, 16235–16245.
- 46 J. K. Das, A. K. Samantara, A. K. Nayak, D. Pradhan and J. N. Behera, *Dalton Trans.*, 2018, **47**, 13792–13799.
- 47 F. Yang, P. Zhao, X. Hua, W. Luo, G. Cheng, W. Xing and S. Chen, *J. Mater. Chem. A*, 2016, **4**, 16057–16063.
- 48 J. Sun, J. Li, Z. Li, X. Hu, H. Bai and X. Meng, *ACS Sustain. Chem. Eng.*, 2022,

- 10**, 4022–4030.
- 49 L. Yan, L. Cao, P. Dai, X. Gu, D. Liu, L. Li, Y. Wang and X. Zhao, *Adv. Funct. Mater.*, 2017, **27**, 1703455.
- 50 Y. Zang, B. Yang, A. Li, C. Liao, G. Chen, M. Liu, X. Liu, R. Ma and N. Zhang, *ACS Appl. Mater. Interfaces*, 2021, **13**, 41573–41583.
- 51 J. Liang, Y. Yang, J. Zhang, J. Wu, P. Dong, J. Yuan, G. Zhang and J. Lou, *Nanoscale*, 2015, **7**, 14813–14816.
- 52 T. Tian, L. Huang, L. Ai and J. Jiang, *J. Mater. Chem. A*, 2017, **5**, 20985–20992.
- 53 T. Liu, P. Li, N. Yao, T. Kong, G. Cheng, S. Chen and W. Luo, *Adv. Mater.*, 2019, **31**, 1–8.

CHAPTER – 3

MOF-derived Co₃S₄ nanoparticles embedded in nitrogen-doped carbon for electrochemical oxygen production

3.1 Abstract

3.2 Introduction

3.3 Experimental Section

3.3.1 Materials

3.3.2 Synthesis of Co-MOF

3.3.3 Preparation of Co₃S₄-3h

3.4 Material characterization

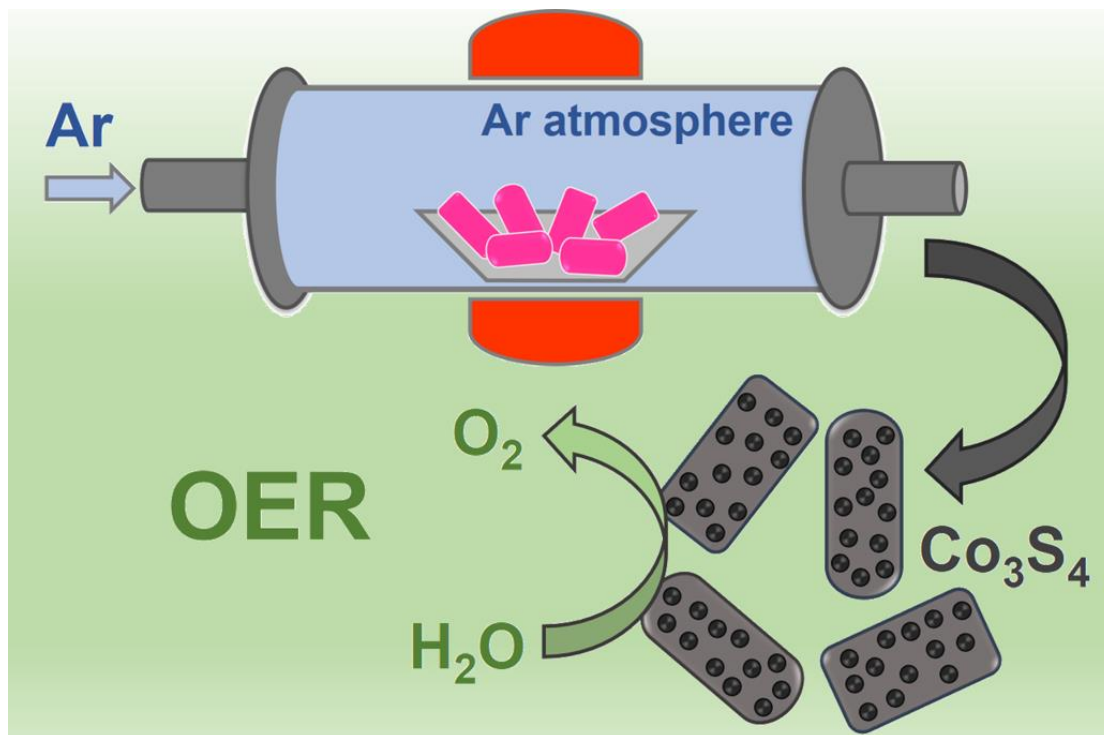
3.5 Electrochemical measurements

3.6 Results and discussion

3.7 Conclusions

3.8 References

3.1 Abstract



The development of a simple and effective strategy for designing a highly efficient oxygen evolution electrocatalyst is more important to speed up the efficiency-limiting step involved in water electrolysis. The high efficiency of the oxygen evolution reaction (OER) is directly correlated with the class of electrode materials employed. This work reports a series of Co_3S_4 nanoparticles (Co_3S_4 -2h, Co_3S_4 -3h, and Co_3S_4 -4h) derived from a metal-organic framework (MOF) via a single-step annealing strategy with varying reaction times for the study of OER. During the annealing process, the MOF precursor $[\text{Co}_3(\text{tiron-bpy})_2(\text{bpy})(\text{H}_2\text{O})_8] \cdot (\text{H}_2\text{O})_2$ termed as Co-T-BPY directly converted to cobalt sulfide (Co_3S_4) nanoparticles, along with additional support of the N-doped carbon moiety. Interestingly, variation of reaction time in a fixed temperature condition played a decisive role in optimizing the surface area with huge active sites of the derived products. The optimized Co_3S_4 -3h product needed an overpotential of 285

mV to reach 10 mA cm^{-2} current density and an acceptable Tafel value (109 mV dec^{-1}) with excellent 14 h of stability performance under harsh alkaline conditions. The OER results are attributed to the combined effect of the Co_3S_4 phase and N-doped carbon matrix, resulting in substantial stability and high conductivity. Therefore, we believe that the time variation strategy for the preparation of a cobalt-based non-precious electrode material can pave the way in search of an OER-efficient electrocatalyst.

3.2 Introduction

The growing energy crisis and environmental deterioration motivate researchers to search for alternative clean energy techniques that maintain a carbon-free environment compared to traditional fossil fuels. The electrocatalytic water splitting system offers a better footpath for producing energy fuels such as hydrogen.¹⁻³ However, the major obstacle to producing hydrogen through water splitting is to overcome the high overpotential for counter anodic oxygen evolution reaction (OER). OER is the half-cell reaction that demands a kinetically sluggish four-electron step reaction mechanism to evolve molecular oxygen (O_2).⁴⁻⁶ Consequently, developing an appropriate electrocatalyst with improved surface kinetics is necessary to catalyze OER at lower additional energy (overpotential). Noble metal-based oxides such as RuO_2 and IrO_2 are considered the benchmark electrocatalyst for O_2 production in alkaline media. However, scarcity, low abundance, and stability issues in alkaline medium restrict its widespread industrial application.^{7,8} In recent years, enormous efforts have been made to design efficient non-precious OER electrocatalysts to overcome the sluggish kinetics and stability issues for the smooth running of oxygen evolution.

Transition metal-based chalcogenides like sulfides, selenides, and tellurides are considered as the suitable candidate for OER, on account of their inherent advantages

such as high catalytic activity, low cost, and high abundance.^{9–13} In particular, cobalt-based electrocatalysts gained much attention as outstanding contenders for water electrolysis due to their distinctive electronic properties and superior catalytic performance.^{14–17} Notably, cobalt-based sulfide materials (Co₃S₄, CoS₂, Co₉S₈, CoS, and Co_xS_y, etc.) have acquired eye-catching recognition as OER electrocatalysts owing to their variable stoichiometric composition, excellent durability, and lower overpotential values in alkaline electrolytic conditions.^{18–22} As per the literature survey, Ji et al. reported CoS₂ microspheres that needed an overpotential of 310 mV to achieve a current density of 10 mA cm⁻².²³ Similarly, Guo et al. synthesized CoS nanosheet arrays on nickel foam that demands an overpotential of 297 mV to acquire 10 mA cm⁻² current density.²⁴ Among all reported sulfides, Co₃S₄, being a normal spinel and having a metallic nature, assures rapid charge transport during electrocatalytic water oxidation.²⁵ However, bulk Co₃S₄ is still associated with some limitations in electrocatalytic OER because of their easy aggregation and fewer electrochemical active sites leading to an increase in the value of overpotential. Zhao et al. fabricated nanoporous hollow Co₃S₄ nanosheets that required 363 mV overpotential to deliver 10 mA cm⁻² current density.²⁶ To overcome such limitations, several strategies have been made to modulate the surface chemical structure of the Co₃S₄ catalyst, increasing the stability and accelerating the charge transport for better catalytic performance. The embedment of a carbon moiety serves as a conventional approach to prevent corrosion as well as aggregation of electroactive material during long-term electrolysis. Additionally, the introduction of the heteroatom doped carbon matrix (N-doped carbon) is one of the strategies that are advantageous in regard to both conductivity and chemical stability.^{27,28}

Recently, metal-organic frameworks (MOFs) earned enormous attention as a suitable sacrificial template for the fabrication of carbon-based functional materials. The porous characteristic and orderly arranged crystalline structure in MOFs are established by the systematic arrangement of metal centers and organic ligands.^{29–31} In this regard, selecting the proper MOF precursor becomes the most important aspect for synthesizing efficient derived products. Nevertheless, the deficiency of the ideal MOF template holds considerable limitations in this area of research, excluding some well-known single ligand-based MOFs (ZIF-67, MIL-101).^{32,33} Furthermore, the synthesis of metal sulfides, selenides, and nanostructured materials starting with a MOF precursor requires additional sulfurization and selenylation steps that increase the complicity of the overall reaction process.^{34,35} To achieve better performance for OER, various substrates (Ni foam, stainless steel, and carbon cloth), metal doping, and electrodeposition are used for additional activity and durability.^{36,37} Carbonization is one of the strategies where the MOF template is annealed at high temperature for a desired period of time under an inert atmosphere. Upon annealing, the metal part is converted into metal nanoparticles and metal compound nanoparticles and the organic ligand part is transformed into a graphitic carbon matrix to provide additional carbon support.^{38–40} The heteroatoms (N, S, P) present in the organic ligands of the MOF precursor open the window for the development of functional materials supported by the heteroatom-doped carbon matrix upon high-temperature heat treatment under an inert atmosphere.^{41,42} As a consequence, it is incredibly challenging to fabricate efficient metal compound nanoparticles encapsulated by the heteroatom-doped graphitic carbon moiety through a single-step pathway, derived from a MOF template corresponding to a better electrocatalytic performance.

Based on the above findings, we have synthesized a Co-MOF (Co-T-BPY), by considering tiron (contains sulfur) and 4,4'-bipyridine (contains nitrogen) as the ligands. A single-step high-temperature pyrolysis (700 °C) method was followed via a time variation strategy to obtain a series of Co₃S₄ nanoparticles embedded by N-doped carbon moiety such as Co₃S₄-2h, Co₃S₄-3h, and Co₃S₄-4h (time: 2, 3, and 4 h). The time variation factor plays a significant role in optimizing the OER efficiency of the derived products. The optimized Co₃S₄- 3h outperforms as an excellent OER electrocatalyst, which required an overpotential of 285 mV to deliver 10 mA cm⁻² current density and displayed a long-term 14 h constant electrolysis under alkaline conditions reflecting its practical applicability. The improved electrocatalytic performance can be attributed to the spherical nanoparticles like morphology of Co₃S₄ that can afford a higher number of electrochemical active sites for the smooth progress of OER. The nitrogen-doped carbon moiety regulates the chemical environment of the electrocatalyst, which increases the conductivity and provides robust stability during long-term electrolysis. This single-step approach for the preparation of OER-efficient nanoparticles makes the synthesis more feasible and reduces the complexity of the overall reaction process.

3.3 Experimental section

3.3.1 Materials

Co(NO₃)₂·6H₂O, 4,4'-bipyridine, 4,5-dihydroxy-1,3- benzenedisulfonate disodium salt (tiron), RuO₂, Nafion solution, and potassium hydroxide were received from Sigma-Aldrich and HiMedia Chemicals. The chemicals obtained were used as such without further processing. Deionized water was used for washing and preparing the electrolyte solution.

3.3.2 Synthesis of Co-MOF (Co-T-BPY)

The Co-MOF precursor was obtained through a facile hydrothermal method by taking 4,4'-bipyridine and tiron as the ligands as per a previous report.⁴³ First, 0.078 g of 4,4'-bipyridine and 0.166 g of tiron were mixed in 10 mL of deionized water and stirred for 30 min. Afterward, 0.145 g of $\text{Co}(\text{NO}_3)_2 \cdot 6\text{H}_2\text{O}$ was added to the mixed solution and stirring was continued for 1 h. Eventually, the procured solution was transferred into a 23 mL Teflon-lined autoclave and kept in a running oven at 140 °C for 72 h to obtain the desired crystal with the formula $[\text{Co}_3(\text{tiron-bpy})_2(\text{bpy})(\text{H}_2\text{O})_8] \cdot (\text{H}_2\text{O})_2$ labelled as Co-T-BPY.

3.3.3 Preparation of Co_3S_4 -3h

The MOF-precursor was placed in a porcelain boat and was annealed at 700 °C in an Ar atmosphere for 3 h to acquire Co_3S_4 nanoparticles embedded by N-doped carbon moiety termed as Co_3S_4 -3h. For a comparison study, further the MOF-precursor was annealed at 700 °C for 2 and 4 h and the obtained products were named as Co_3S_4 -2h and Co_3S_4 -4h, respectively.

3.4 Material characterization

The phase analysis and crystal system of the materials were recorded using a powder X-ray diffraction instrument (Bruker D8 Advance diffractometer) furnished with a $\text{Cu-K}\alpha$ radiation source with wavelength 1.5418 Å. The morphological evolution and changes have been investigated by a field emission scanning electron microscope (FESEM, Carl Zeiss, Germany make, Model: Σ igma) and a transmission electron microscope (TEM, JEOL 2100F) operated at 200 kV. In order to demonstrate the graphitic phase and disorderredness associated with the materials, a Raman microscope (Horiba Scientific) possessing laser excitation at a wavelength of 532 nm was used.

ray photoelectron spectroscopy examined the sample's elemental composition and desired chemical state by surveying the change in binding energy (XPS, Omicron Nanotechnology Ltd., Germany). The specific surface area investigation of the as-prepared samples was carried out by Quantachrome Instruments (Autosorb iQ) through a N₂ adsorption-desorption isotherm.

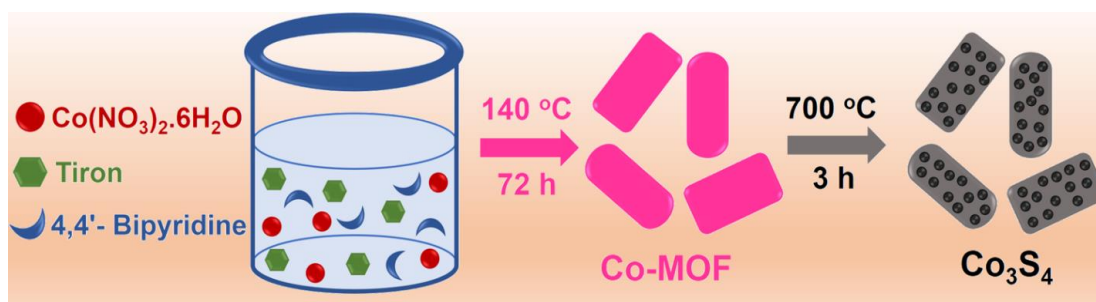
3.5 Electrochemical measurements

All the electrochemical analyses regarding OER were recorded in a three-electrode measurement set-up (BioLogic electrochemical workstation; SP-200) in 1.0 M KOH as the electrolyte. The glassy carbon electrode (GCE; geometrical surface area, 0.07 cm²), platinum wire, and mercury-mercury oxide (Hg/HgO) were used as working, counter, and reference electrodes, respectively. The catalyst ink was prepared by taking 1 mg of active material with a mixture of Nafion and ethanol solutions, followed by sonication to acquire a homogenous slurry. The mass loading of the electrocatalyst on the GCE was maintained at 0.25 mg cm⁻² throughout the measurements. The estimated potentials (vs. Hg/HgO) were converted into the reversible hydrogen electrode (RHE) scale by following the Nernst equation, $E_{\text{RHE}} = E_{\text{Hg/HgO}}^0 + 0.059 \text{ pH} + E_{\text{Hg/HgO}}$. Linear sweep voltammograms (LSVs) for all the samples were measured at a sweep rate of 5 mV s⁻¹. The polarization curves have been *iR* compensated using the solution resistance in order to achieve the actual catalytic behaviour of the electrocatalysts. Tafel slopes were calculated by fitting the linear portion of the logarithm of the current density versus overpotential plot as per the Tafel equation ($\eta = a + b \log J$; where η is overpotential, a is the intercept, b is the Tafel slope and J is the current density). Electrochemical impedance spectroscopy (EIS) or Nyquist plot was carried out in a potentiostatic mode at 1.51 V vs. RHE by applying an AC amplitude of 5 mV in the frequency region of 1

MHz to 0.1 Hz. In order to investigate the electrochemical active surface area (ECSA), double-layer capacitance (C_{dl}) was estimated from cyclic voltammograms (CVs) in the non-Faradaic potential window of 1.12 to 1.22 V vs. RHE at different scan rates (20 mV to 100 mV s^{-1}). A chronopotentiometry method evaluated the durability of the active electrocatalyst at a constant current density of 10 mA cm^{-2} .⁴⁴⁻⁴⁶

3.6 Results and discussions

Scheme 3.1 represents the synthetic route for the preparation of Co_3S_4 nanoparticles embedded by nitrogen-doped carbon moiety. First, the Co-T-BPY MOF was prepared by a hydrothermal approach (the detailed synthesis process is described in the experimental section).



Scheme 3.1: Reaction scheme for the preparation of Co_3S_4 -3h nanoparticles.

The crystal structure, along with the well-matched simulated and experimental powder pattern, confirmed the successful formation of the Co-T-BPY MOF, as illustrated in **Figure 3.1**. The Co-T-BPY MOF was further annealed at $700\text{ }^\circ\text{C}$ under an Ar atmosphere by optimizing the reaction time (2, 3 and 4h) to develop N-doped carbon incorporated Co_3S_4 -T (T represents time) nanoparticles.

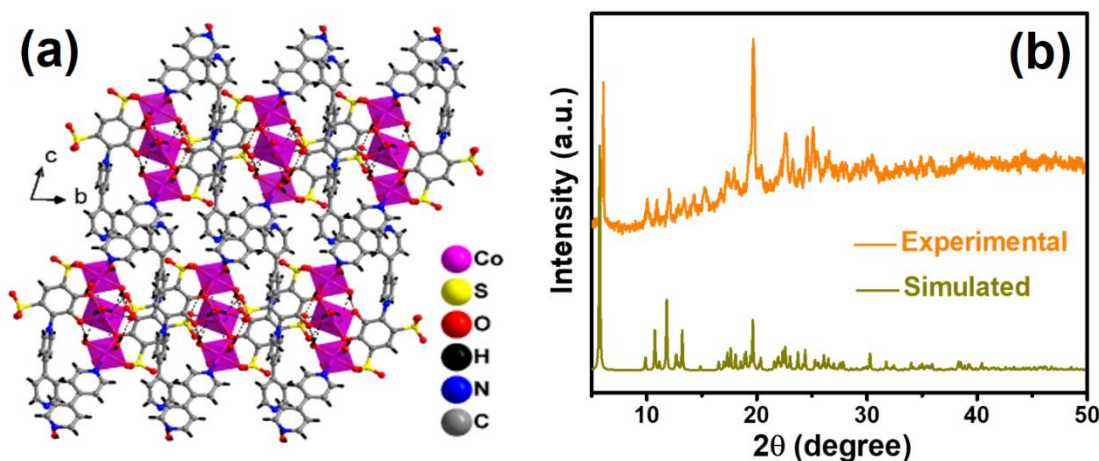


Figure 3.1: Crystal structure (a), and PXRD analysis of Co-MOF (b).

Powder X-ray diffraction (PXRD) analysis of the as-prepared Co_3S_4 -T samples was carried out to investigate the crystal phase information. **Figure 3.2a** illustrates the PXRD data, whereas the distinguished peaks around 26.9 , 31.7 , 38.4 , 47.5 , 50.6 , 55.4° indexed to (220), (311), (400), (422), (511) and (440) diffraction planes of cubic Co_3S_4 phase (JCPDS no. 01-071-4923).⁴⁷ Raman spectroscopy was used to investigate the disorderedness and sp^2 graphitic phase associated with the material. The D band generally indicates disorderedness in the graphite, and the G band represents sp^2 graphitic carbon, indicating the existence of graphitic carbon in the desired sample. As shown in **Figure 3.2b**, two peaks around 1338 and 1596 cm^{-1} were detected, corresponding to D and G bands for all the Co_3S_4 -T products. Additionally, the intensity ratio ($I_{\text{D}}/I_{\text{G}} = 1.01$) is higher for Co_3S_4 -3h compared to other Co_3S_4 -T products (0.97 for Co_3S_4 -2h, 0.95 for Co_3S_4 -4h) demonstrating more structural defects, which became advantageous for the electrocatalytic performance of the sample.⁴⁸

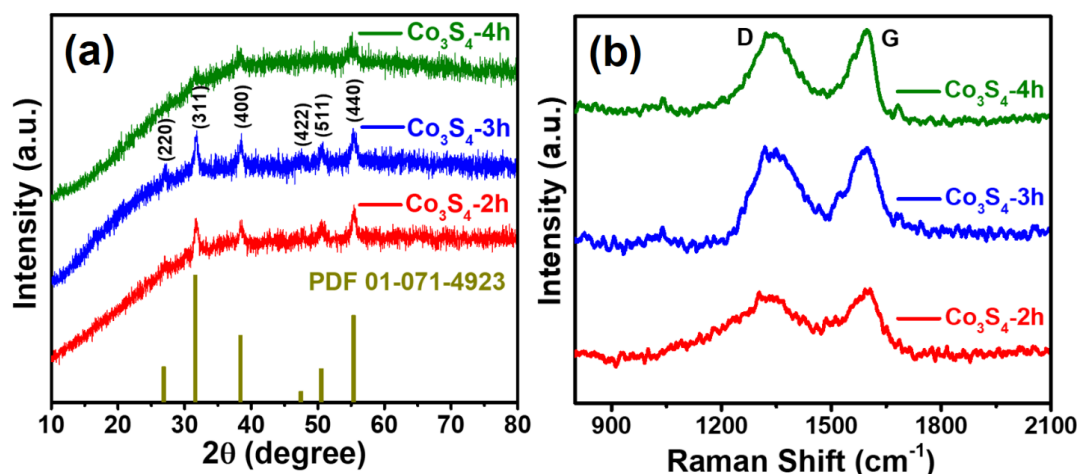


Figure 3.2: Powder X-ray diffraction study (a) and Raman spectra of Co_3S_4 -2h, Co_3S_4 -3h, and Co_3S_4 -4h (b).

The surface morphology of the as-synthesized samples was investigated by scanning electron microscopy (SEM) technique. The SEM analysis suggests the Co-MOF possesses nearly rectangular plates-like morphology prior to the high-temperature heat treatment, as presented in **Figure 3.3**.

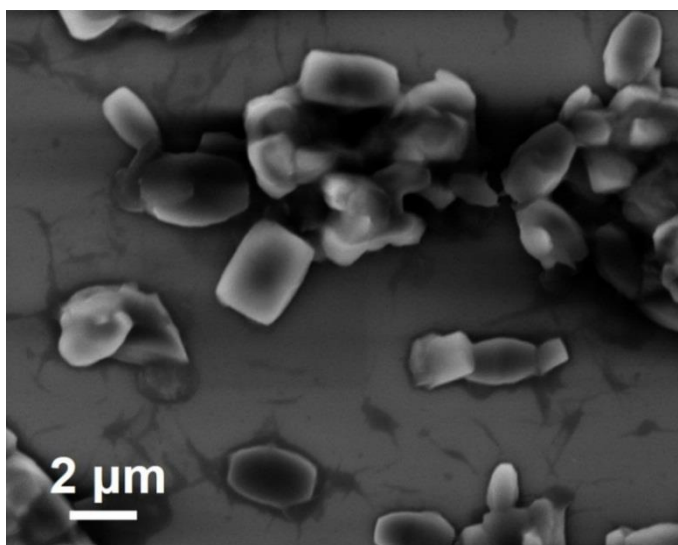


Figure 3.3: SEM image of Co-MOF

After annealing in the Ar atmosphere, the MOF was carbonized, and morphological evolution of Co_3S_4 nanoparticles was observed over the carbonized surface of the MOF.

Interestingly, the variation of time had a significant impact on controlling the morphology of the derived products. An even distribution of the nanoparticles was observed in the case of optimized Co_3S_4 -3h that can be clearly distinguished at different magnifications, as shown in **Figures 3.4a and b**.

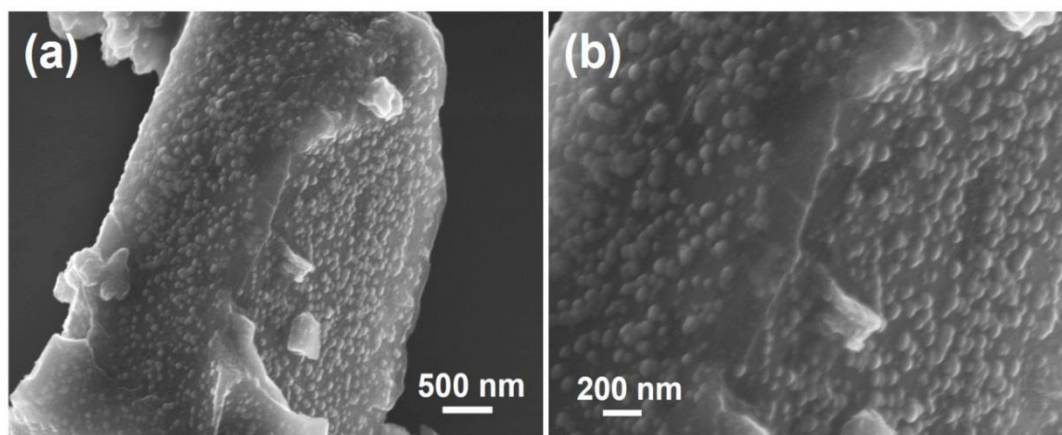


Figure 3.4: SEM analysis of Co_3S_4 -3h at different magnifications (a, b).

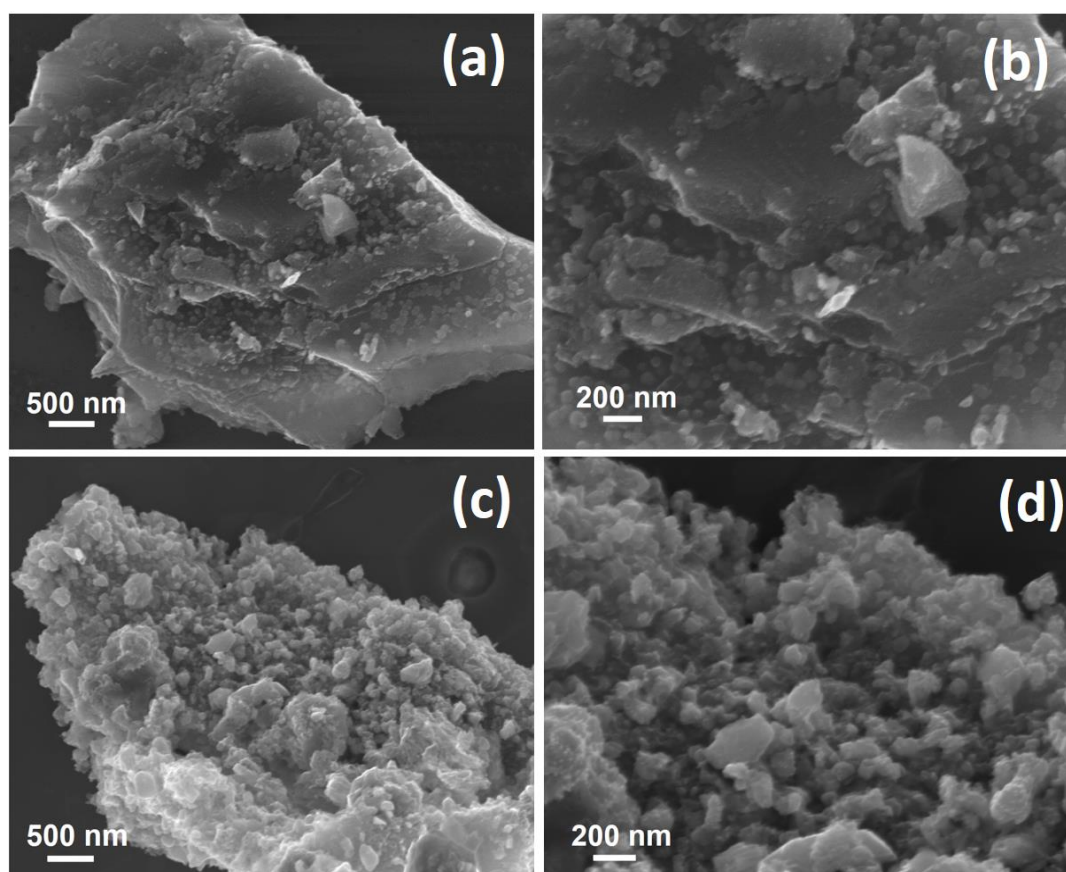


Figure 3.5: FESEM images of Co_3S_4 -2h (a, b) and Co_3S_4 -4h (c, d).

In contrast, in case of Co_3S_4 -2h, the growth of the nanoparticles was restricted to some extent, which may be attributed to lesser reaction of time of 2 h (**Figures 3.5a and b**). For Co_3S_4 -4h, nanoparticles were organized to form a fused morphology owing to the longer exposure time of 4 h, as shown in **Figures 3.5c and d**.

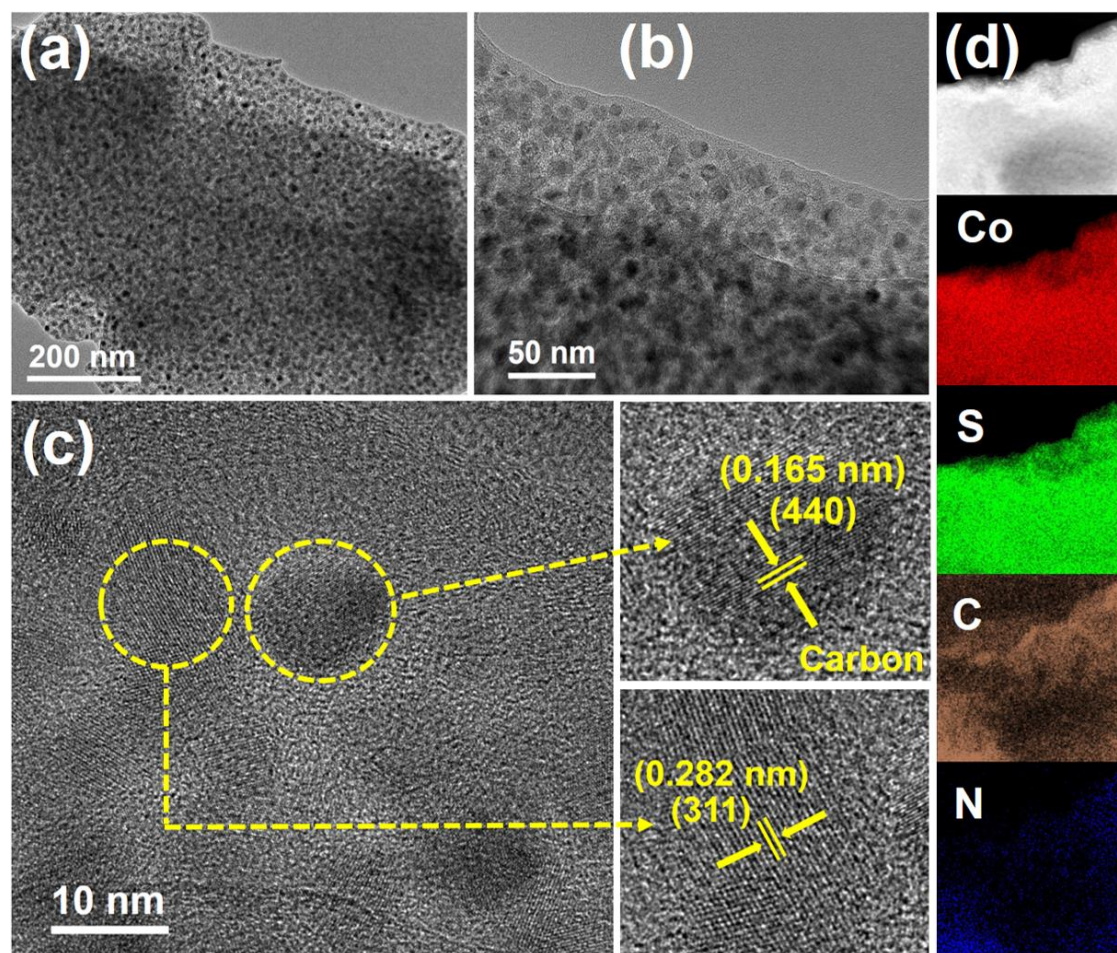


Figure 3.6: TEM investigation of Co_3S_4 -3h at various magnifications (a, b). High-resolution TEM of Co_3S_4 -3h (c). EDS mapping images showing Co, S, C, and N distribution in Co_3S_4 -3h (d).

TEM analysis was used to gain deep insights into the surface morphology of the Co_3S_4 -3h. The TEM analysis at different magnifications confirmed that these nanoparticles were organized uniformly and embedded by the carbon layers, as presented in **Figures 3.6a and b**. The HRTEM analysis shows two lattice fringes with an interplanar spacing value of 0.165 and 0.282 nm corresponding to the (440) and (311) planes of the Co_3S_4

phase, respectively, as shown in **Figure 3.6c**. The elemental distribution of the as-prepared Co_3S_4 -3h was explored with the help of energy dispersive spectrum (EDS) mapping. **Figure 3.6d** represents the uniform distribution of Co, S, C, and N, indicating the suitable conversion of Co-MOF into Co_3S_4 nanoparticles embedded by N-doped carbon moiety.

The specific surface area analysis of the electrocatalysts was carried out by Brunauer-Emmett-Teller (BET) isotherm. The N_2 adsorption-desorption isotherm suggests that Co_3S_4 -3h has the highest specific surface area of $101.03 \text{ m}^2 \text{ g}^{-1}$, which is higher than Co_3S_4 -2h ($42.91 \text{ m}^2 \text{ g}^{-1}$) and Co_3S_4 -4h ($39.53 \text{ m}^2 \text{ g}^{-1}$) as appeared in **Figure 3.7**. The BET results indicate that the time optimization factor of the annealing process plays a crucial role in optimizing the specific surface area of the samples, which later became beneficial for providing a larger ECSA for OER.

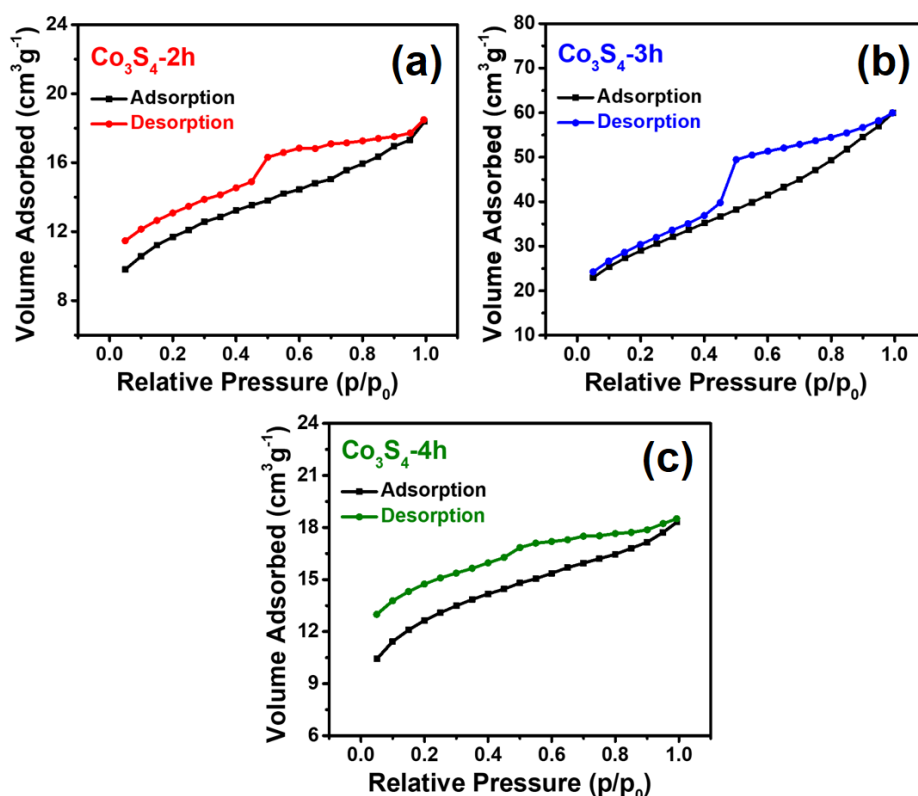


Figure 3.7: BET surface area investigation of Co_3S_4 -2h (a), Co_3S_4 -3h (b), and Co_3S_4 -4h.

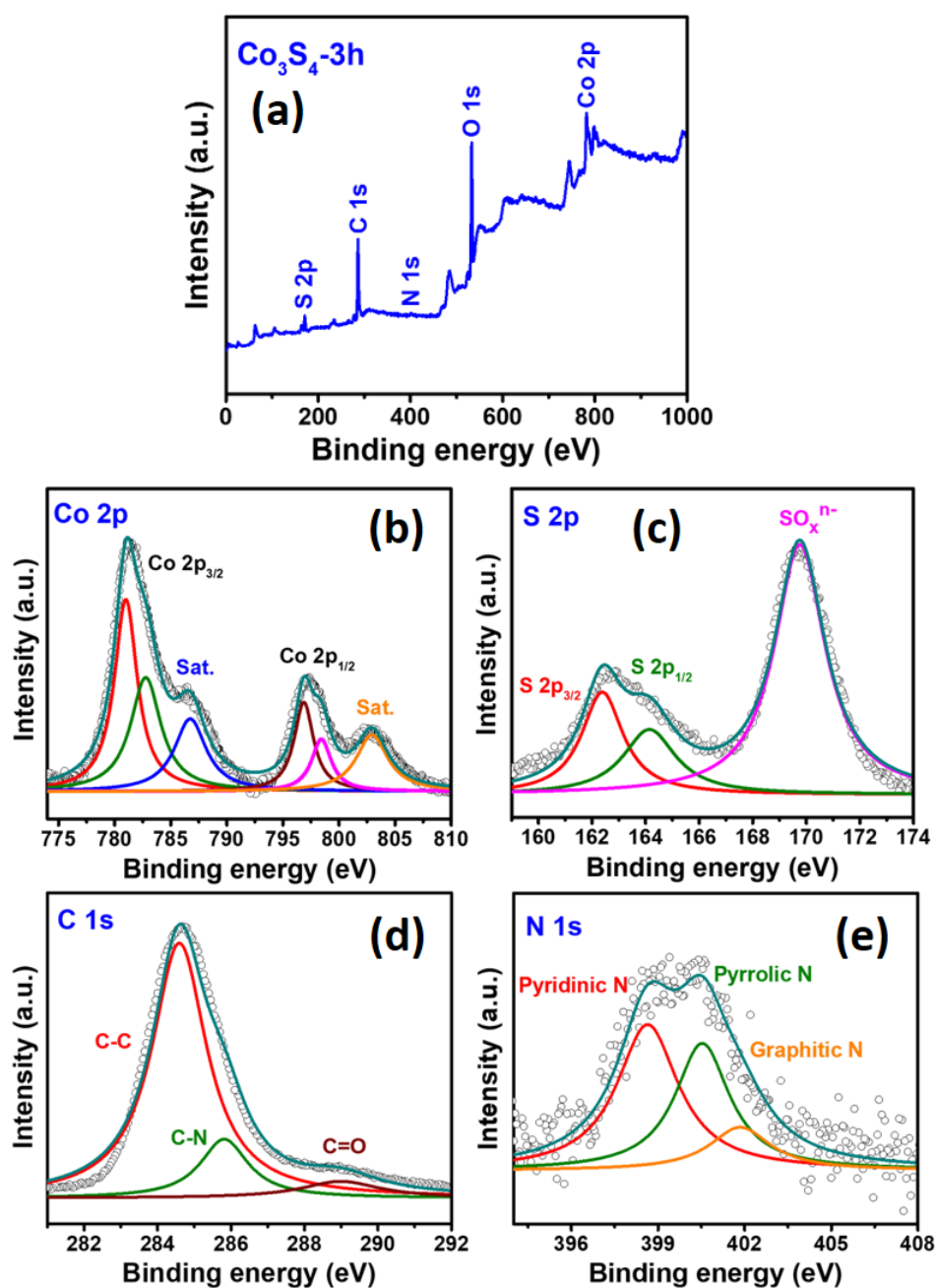


Figure 3.8: Full scan XPS survey spectra of Co_3S_4 -3h (a), deconvoluted XPS spectra of Co 2p (b), S 2p (c), C 1s (d), N 1s (e).

In order to explore the chemical composition and elemental state, XPS analysis was performed for the electroactive Co_3S_4 -3h sample. **Figure 3.8a** illustrates the full scan survey spectrum that confirms the presence of Co, S, C, N, and O elements in the sample. The presence of O_2 can be ascribed to the inevitable O_2 species or the surface

oxidation of the sample upon areal exposure.⁴⁹ As shown in **Figure 3.8b** the high-resolution Co 2p XPS spectrum is deconvoluted into two spin-orbit doublets. The first doublet centered at 780.9 eV (Co 2p_{3/2}) and 796.8 eV (Co 2p_{1/2}) ascribed to Co³⁺, and the second doublet located at 782.7 eV (Co 2p_{3/2}) and 798.3 eV (Co 2p_{1/2}) assigned to Co²⁺, indicating the coexistence of Co²⁺ and Co³⁺ species. In addition, the broad peaks at 786.7 and 802.9 eV are ascribed to the satellite peaks.^{50,51} **Figure 3.8c** reveals the high-resolution S 2p spectra of the Co_3S_4 -3h sample. The peaks around 162.3 eV and 164.1 eV can be assigned to S 2p_{3/2} and S 2p_{1/2}, respectively, owing to the formation of the Co-S bond.^{52,53} The peak located at 169.7 eV can be assigned to the oxidized sulfur species, possibly due to the partial surface oxidation on exposure to air.^{54,55} The C 1s spectra can be deconvoluted into three peaks located at 284.6 eV (C-C), 285.8 eV (C-N), and 289.0 eV (C=O) as depicted in **Figure 3.8d**.⁵⁶ **Figure 3.8e** represents deconvoluted N 1s spectrum, having three different kinds of nitrogen, positioned at 398.6 eV (pyridinic), 400.5 eV (pyrrolic), and 401.8 eV (graphitic).^{57,58}

Oxygen evolution reaction

The electrocatalytic activity of the samples toward water oxidation was evaluated in a three-electrode measurement set-up under an alkaline environment (1.0 M KOH). Sample-modified GCE was taken as the working electrode, Pt-wire as the counter electrode, and Hg/HgO as the reference electrode. In order to acquire the inherent catalytic behaviour of the electrocatalysts, *iR* compensation was done, and the LSVs with and without *iR* correction are presented in **Figure 3.9**. **Figure 3.10a** shows the LSV curves of the RuO₂, Co-MOF, and derived Co_3S_4 products synthesized by time variation. From the LSV plot, it is evident that the time optimized Co_3S_4 -3h has the lowest overpotential compared to other derived Co_3S_4 products (Co_3S_4 -2h and Co_3S_4 -

4h) as well as RuO_2 and the Co-MOF precursor. Co_3S_4 -3h required a lower overpotential of 285 mV to deliver 10 mA cm^{-2} current density, compared to Co_3S_4 -2h (316 mV), Co_3S_4 -4h (334 mV), Co-MOF (404 mV) revealing their relatively substandard catalytic activity. The lower overpotential value obtained in the case of Co_3S_4 -3h demonstrates the significance of time optimization for the annealing process. The overpotential comparison of all the Co_3S_4 -T products is displayed in **Figure 3.10b**. The optimized Co_3S_4 -3h with such remarkable OER performance surpasses Co_3S_4 -2h, Co_3S_4 -4h, RuO_2 , and other previously investigated non-noble metal-based electrocatalysts reflecting its superiority as an efficient water oxidation catalyst, as depicted in **Table 3.1**.

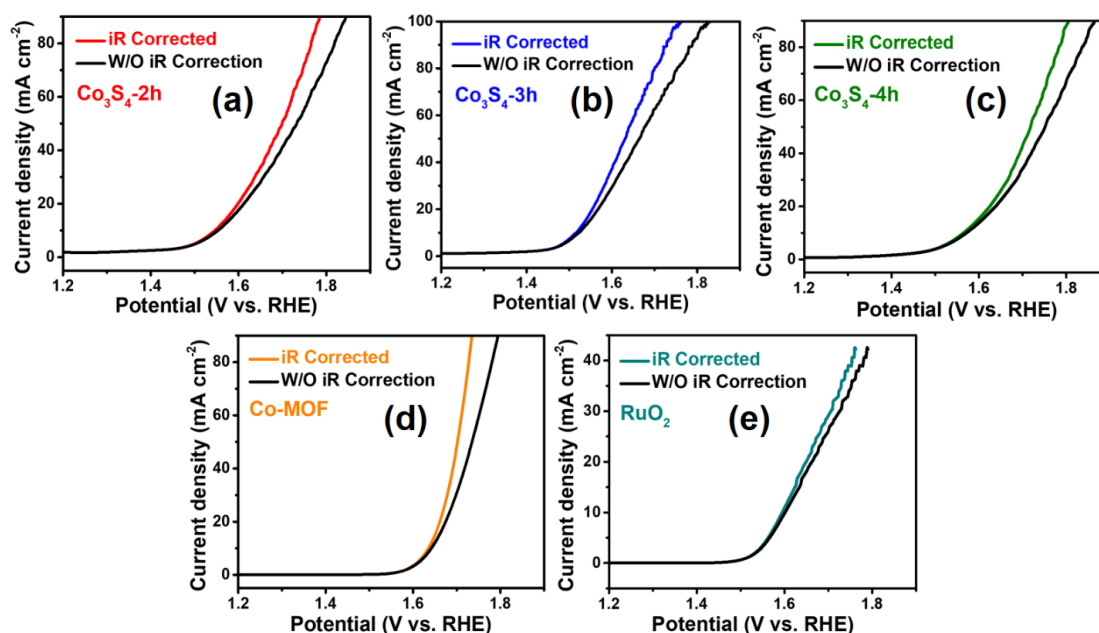


Figure 3.9: LSVs of Co_3S_4 -T products (a-c), Co-MOF (d), and RuO_2 before and after iR compensation (e).

Tafel slope dealing with the kinetics of the electrocatalysts was investigated for all the samples. A smaller Tafel slope indicates faster reaction kinetics of an active electrocatalyst for oxygen production.⁵⁹ The Tafel slope calculated from the LSV data demonstrates that among different time-varied Co_3S_4 products, Co_3S_4 -3h has the lowest Tafel slope of 109 mV dec^{-1} , smaller than those of Co_3S_4 -2h (156 mV dec^{-1}) and Co_3S_4 -4h (167 mV dec^{-1}) illustrating suitable kinetics for oxygen evolution (Figure 3.10c).⁶⁰

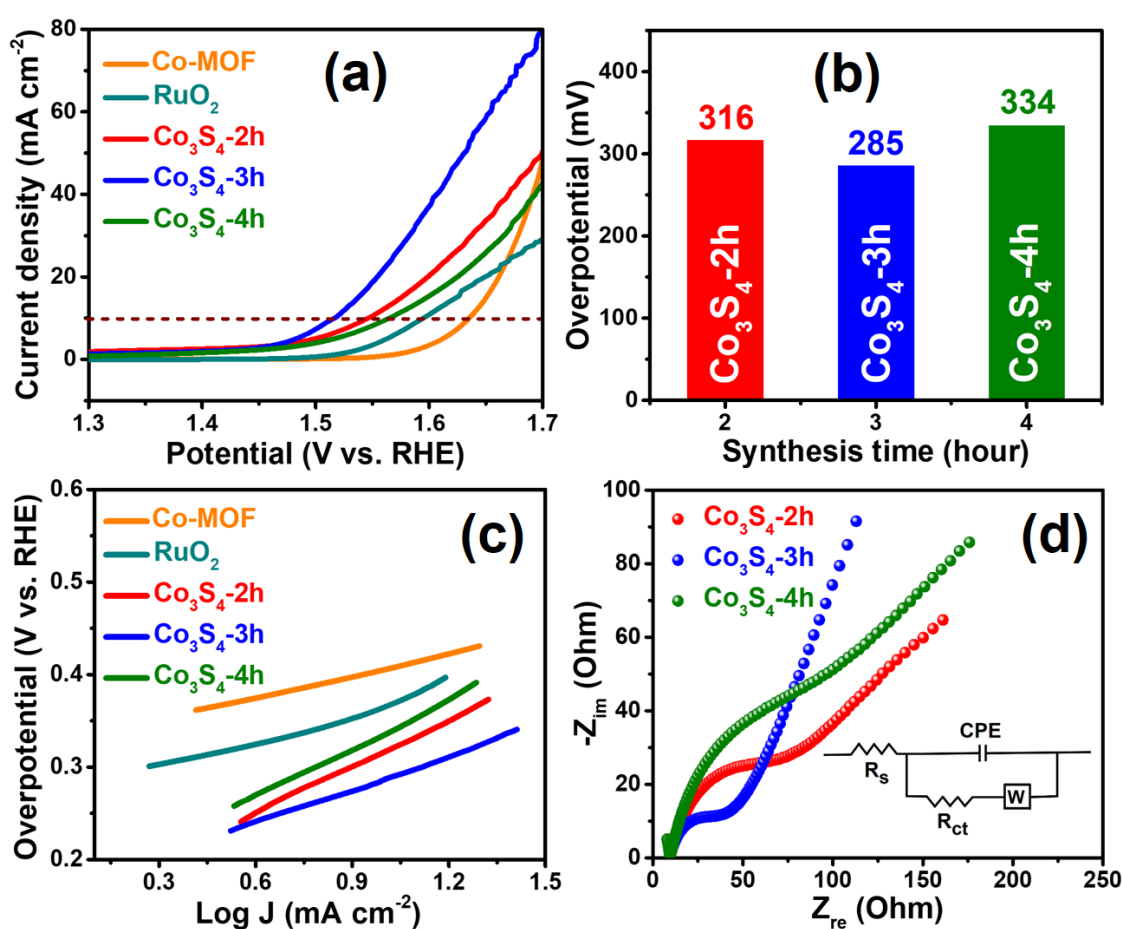


Figure 3.10: LSVs of Co-MOF, Co_3S_4 -T samples, and RuO_2 (a). Overpotential comparison of Co_3S_4 -T products at 10 mA cm^{-2} current density (b). Corresponding Tafel slopes of Co-MOF, Co_3S_4 -T products, and RuO_2 (c). EIS study of Co_3S_4 -T products at 1.51 V vs. RHE (d). Inset in (d) is the corresponding equivalent circuit diagram.

EIS or Nyquist plot was employed to examine the charge transfer dynamics of the as-synthesized OER active electrocatalysts. EIS data were recorded at 1.51 V vs. RHE in a frequency region of 1 MHz to 0.1 Hz by supplying an AC amplitude of 5 mV for all the Co_3S_4 -T samples. It is evident in **Figure 3.10d** that at the region of high frequency, all the Co_3S_4 -T samples showed relatively similar solution resistance (R_s), which is a combination of electrolyte resistance, intrinsic resistance of the used electrode, and contact resistance. However, the lower the diameter of the arc, the lesser will be the charge transfer resistance resulting in faster electron transfer at the electrode-electrolyte interface. The Co_3S_4 -3h possessed the smallest arc (R_{ct}) among all Co_3S_4 -T products, which became beneficial for the smooth progress of OER in an alkaline medium.^{61,62} The inset in **Figure 3.10d** displays the corresponding equivalent circuit diagram.

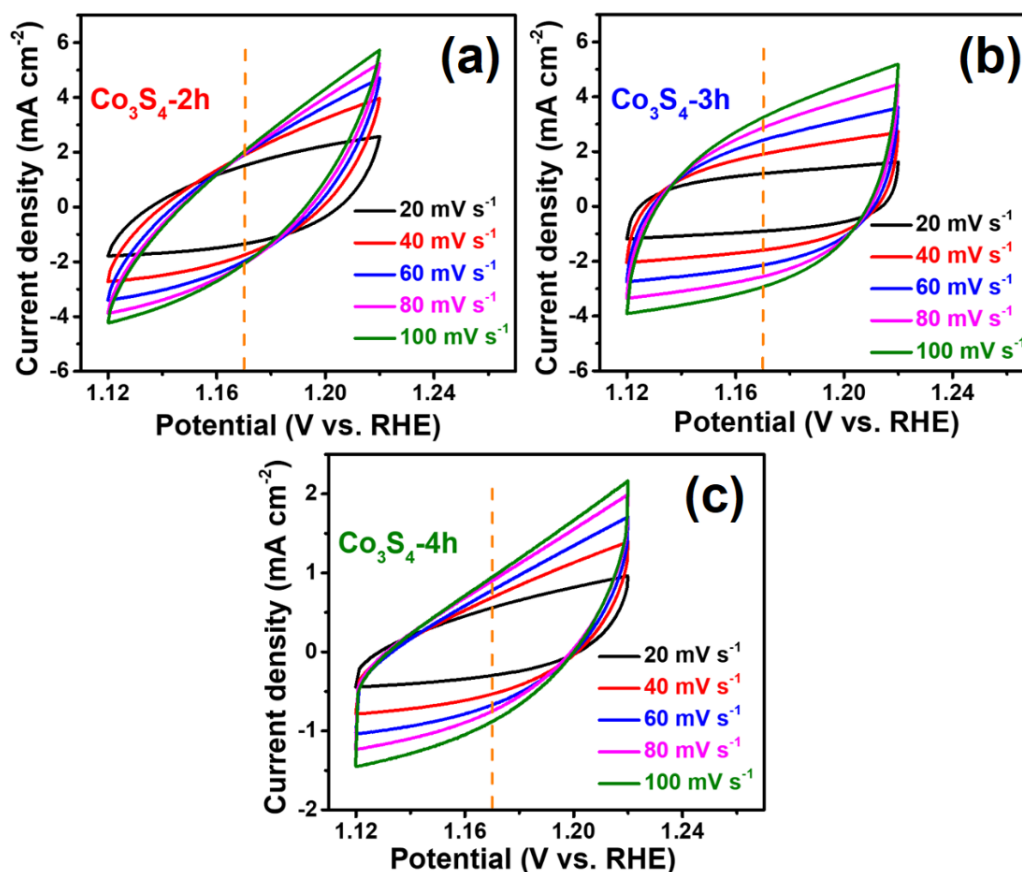


Figure 3.11: CVs of Co_3S_4 -2h (a), Co_3S_4 -3h (b), and Co_3S_4 -4h in the potential window of 1.12 to 1.22 V vs. RHE (c).

Furthermore, the electrochemical accessible surface area (ECSA) for all the Co_3S_4 -T products was investigated by determining C_{dl} from CV curves in the non-Faradaic potential window of 1.12 to 1.22 V vs. RHE by varying the scan rates as shown in **Figure 3.11**.

In general, C_{dl} is directly related to the ECSA of the samples.⁶³ The plot of various scan rates against half of the difference of anodic and cathodic current density ($\Delta J = J_a - J_c$) produces a straight line whose slope is equal to C_{dl} . **Figure 3.12a** presents the C_{dl} values of Co_3S_4 -2h, Co_3S_4 -3h, and Co_3S_4 -4h at 1.17 V vs. RHE. Co_3S_4 -3h has a higher C_{dl} value of 25.23 mF cm^{-2} compared to Co_3S_4 -2h (8.55 mF cm^{-2}) and Co_3S_4 -4h (6.01 mF cm^{-2}), demonstrating the availability of larger electrochemically active sites for the OER to occur.⁶⁴ Interestingly, the ECSA results were closely related to the specific surface area analysis of the Co_3S_4 -T products obtained from the BET data. The nitrogen doping in the carbon network supplement additional defect driven active sites beneficial for the electrocatalytic process.⁶⁵

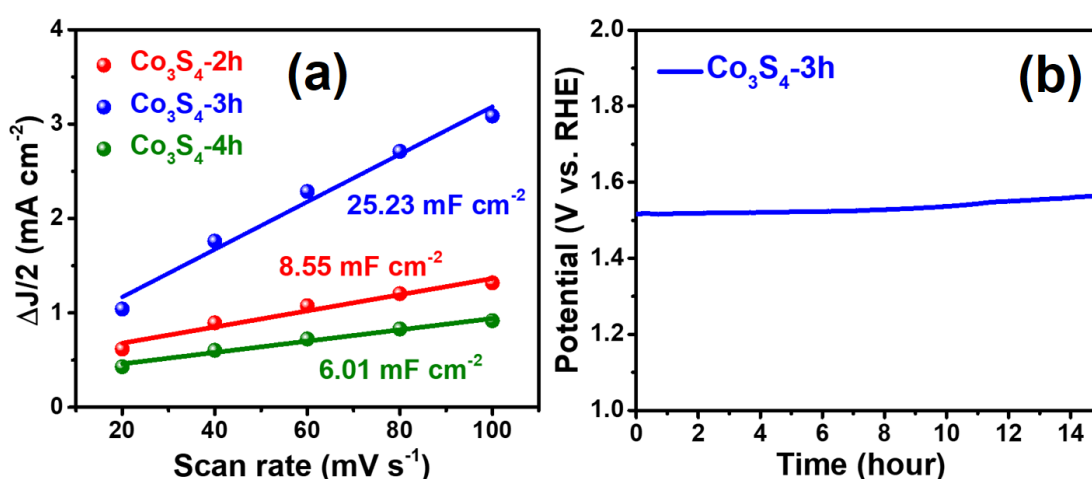


Figure 3.12: Double-layer capacitance of Co_3S_4 -T products at 1.17 V vs. RHE (a), chronopotentiometry durability analysis of Co_3S_4 -3h in alkaline electrolytic conditions (b).

Stability is one of the key parameters related to the practical applicability of the material. In order to investigate the long-term durability of the as-synthesized electrode material, the chronopotentiometry (CP) test was performed at a constant 10 mA cm^{-2} current density. The Co_3S_4 -3h electrocatalyst was significantly stable up to 14 h of constant electrolysis with negligible increase in overpotential under harsh alkaline electrolytic conditions of 1.0 M KOH, as represented in **Figure 3.12b**. The excellent stability of Co_3S_4 -3h can be attributed to the encapsulation of the Co_3S_4 nanoparticles with the N-doped carbon moiety that provides substantial stability and prevents aggregation during long-term electrolysis in alkaline electrolytic conditions.

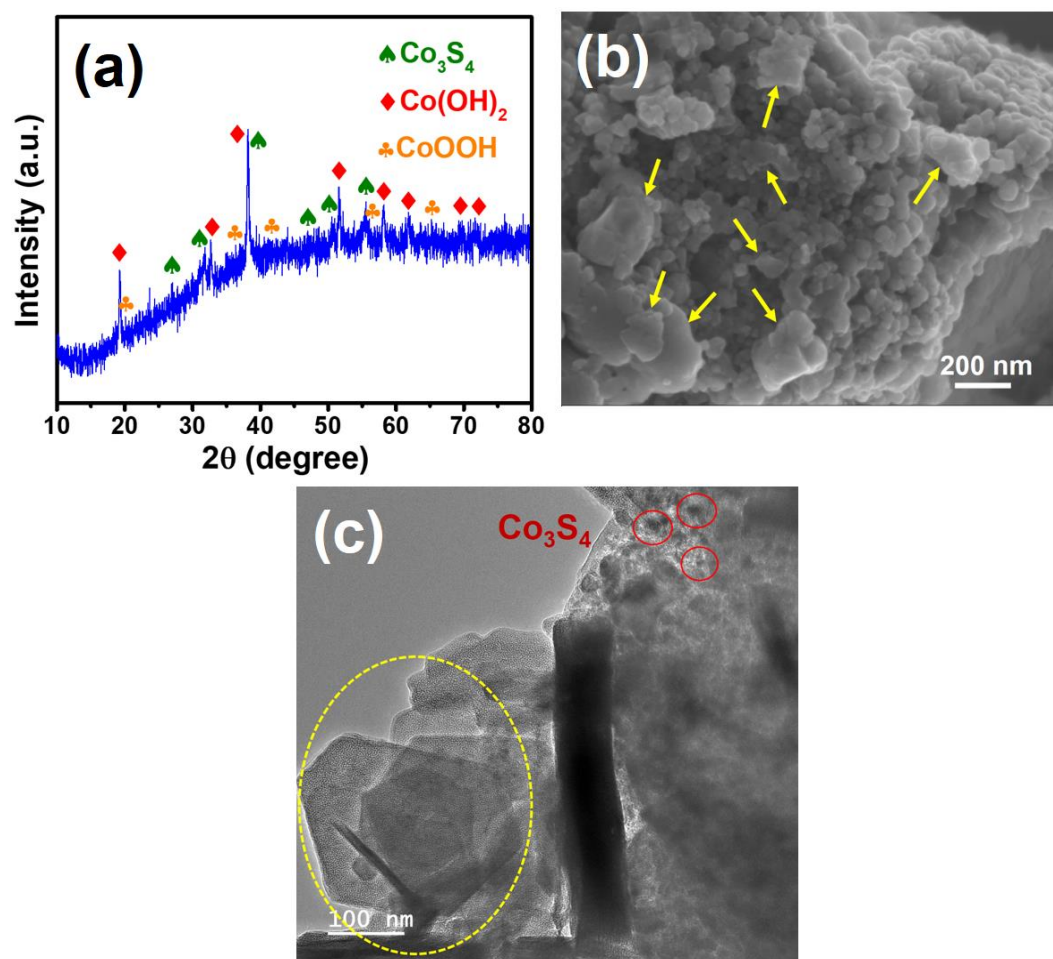


Figure 3.13: PXR (a), FESEM (b), and TEM investigation of Co_3S_4 -3h after the durability test (c).

Additionally, to examine the fate of the material after long-term electrolysis, post-stability PXRD characterization was performed. The PXRD pattern of Co₃S₄-3h after the durability test reveals a slight change in the phase of the material, where two additional phases (Co(OH)₂ and CoOOH) were observed along with the major Co₃S₄ phase as illustrated in **Figure 3.13a**. To support the results obtained from the PXRD data, FESEM and TEM investigations were also carried out. As displayed in the SEM and TEM images (**Figures 3.13b and c**), some additional plate-like morphologies were appeared along with the Co₃S₄ nanoparticles after the long-term stability test. The plate-like morphology can be ascribed to the Co(OH)₂ and CoOOH phases, as per the previous reports.^{51,66} These investigations demonstrate a surface reconstruction of the electrocatalyst during OER, where oxide-hydroxide layers were formed on the surface of the electrocatalyst. The reconstructed oxide-hydroxide species formed during electrolysis becomes the active phase which eventually enhances the oxygen evolution activity.^{22,67}

The outstanding catalytic activity and durability of the as-synthesized material can be ascribed to the distinctive encapsulation of Co₃S₄ nanoparticles by the N-doped carbon moiety. The combination of Co₃S₄ nanoparticles and surrounding N-doped carbon matrix afford a higher specific surface area that ultimately promises a larger ECSA. The larger value of ECSA exposes the active catalytic sites, allowing proper electrolyte diffusion and shortening the electron transfer path for the smooth progress of OER.^{51,62} The carbon part surrounding the Co₃S₄ nanoparticles notably protects the electrocatalyst by avoiding aggregation and corrosion during long-term electrolysis. Nitrogen doping in the carbon matrix tunes the electronic environment by reducing the work function of the carbon layers promoting the electron transfer between carbon layers and Co₃S₄ that eventually enhances the conductivity of the electrocatalysts.

Table 3.1: Oxygen evolution reaction (OER) performance comparison of Co_3S_4 -3h with some previously reported literature.

Electrocatalyst used	Overpotential at 10 mA cm ⁻² (mV)	Electrolyte	References
defect-rich Co_3S_4 nanoparticles	250	1.0 M KOH	Carbon 2020, 160, 133-144
Co_3S_4 thin film	275	1.0 M KOH	Applied Physics A (2020) 126,206
$\text{Co}/\text{Co}_9\text{S}_8@\text{NSOC}-800$	373	1.0 M KOH	Chem. Commun., 2019, 55, 3203-3206
Co_3S_4 nanoparticles	270	1.0 M KOH	ACS Appl. Energy Mater. 2020, 3, 977-986
Ni-doped Co_3S_4 nanospheres	298	1.0 M KOH	Inorg. Chem. Front., 2022, 9, 3924
hollow $\text{Co}_3\text{S}_4@\text{NiMoO}_4$ nanotube	320	1.0 M KOH	Int. J. Hydrog. Energy 45 (2020) 30463-30472
$\text{Co}_9\text{S}_8@\text{MoS}_2$ core-shell heterostructures	342	1.0 M KOH	ACS Appl. Mater. Interfaces 2018, 10, 1678-1689
MOF-derived porous Co_3O_4 composite	420	1.0 M KOH	ChemistrySelect 2019, 4, 1131-1137
Ni-doped CoS_2/CFP	270	1.0 M KOH	ChemElectroChem 2019, 6, 1206-1212
$\text{Co}_{1-x}\text{S}/\text{Co}(\text{OH})\text{F}$	269	1.0 M KOH	ACS Nano 2022, 16, 9, 15460-15470
Co_3S_4-3h	285	1.0 M KOH	This Work

3.7 Conclusions

In summary, we followed a simple and cost-effective strategy for the preparation of Co_3S_4 nanoparticles embedded in N-doped carbon moiety by annealing in an inert atmosphere of a Co-MOF precursor containing N and S heteroatoms. The alteration of time for the annealing process had a significant impact on optimizing the surface area of the derived sulfide products. The optimum Co_3S_4 -3h acts as a superior electrocatalyst for OER, requiring a low overpotential of 285 mV to acquire 10 mA cm⁻² current density as well as outstanding durability of 14 h in an alkaline electrolytic condition.

The notable catalytic performance can be attributed to the combined effect of the active Co_3S_4 phase and the enwrapping of N-doped carbon moiety that restricts the agglomeration and corrosion of the active species during long-term electrolysis under harsh conditions. The N-doped carbon moiety tuned the electronic environment resulting in the enhancement of the conductivity of the electrocatalyst and triggering the intrinsic catalytic activity. The sacrificial annealing approach of the Co-MOF precursor opens a new window for the development of N-doped carbon-wrapped non-noble metal-based sulfide (Co_3S_4) that excels as an outstanding electrocatalyst for O_2 production.

3.8 References

- 1 N. T. Suen, S. F. Hung, Q. Quan, N. Zhang, Y. J. Xu and H. M. Chen, *Chem. Soc. Rev.*, 2017, **46**, 337–365.
- 2 Z. Kang, H. Guo, J. Wu, X. Sun, Z. Zhang, Q. Liao, S. Zhang, H. Si, P. Wu, L. Wang and Y. Zhang, *Adv. Funct. Mater.*, 2019, **29**, 1807031.
- 3 M. Tahir, L. Pan, F. Idrees, X. Zhang, L. Wang, J. J. Zou and Z. L. Wang, *Nano Energy*, 2017, **37**, 136–157.
- 4 J. Joo, T. Kim, J. Lee, S. Il Choi and K. Lee, *Adv. Mater.*, 2019, **31**, 1–23.
- 5 J. Wang, W. Cui, Q. Liu, Z. Xing, A. M. Asiri and X. Sun, *Adv. Mater.*, 2016, **28**, 215–230.
- 6 X. Xia, L. Wang, N. Sui, V. L. Colvin and W. W. Yu, *Nanoscale*, 2020, **12**, 12249–12262.
- 7 L. Zhao, B. Dong, S. Li, L. Zhou, L. Lai, Z. Wang, S. Zhao, M. Han, K. Gao, M. Lu, X. Xie, B. Chen, Z. Liu, X. Wang, H. Zhang, H. Li, J. Liu, H. Zhang, X. Huang and W. Huang, *ACS Nano*, 2017, **11**, 5800–5807.

-
- 8 V. Maruthapandian, M. Mathankumar, V. Saraswathy, B. Subramanian and S. Muralidharan, *ACS Appl. Mater. Interfaces*, 2017, **9**, 13132–13141.
 - 9 C. Mahala, M. D. Sharma and M. Basu, *New J. Chem.*, 2019, **43**, 15768–15776.
 - 10 Z. Fang, L. Peng, H. Lv, Y. Zhu, C. Yan, S. Wang, P. Kalyani, X. Wu and G. Yu, *ACS Nano*, 2017, **11**, 9550–9557.
 - 11 M. Wang, L. Zhang, Y. He and H. Zhu, *J. Mater. Chem. A*, 2021, **9**, 5320–5363.
 - 12 M. Nath, U. De Silva, H. Singh, M. Perkins, W. P. R. Liyanage, S. Umapathi, S. Chakravarty and J. Masud, *ACS Appl. Energy Mater.*, 2021, **4**, 8158–8174.
 - 13 W. Li, D. Xiong, X. Gao and L. Liu, *Chem. Commun.*, 2019, **55**, 8744–8763.
 - 14 A. Zhao, G. Xu, Y. Li, J. Jiang, C. Wang, X. Zhang, S. Zhang and L. Zhang, *Inorg. Chem.*, 2020, **59**, 12778–12787.
 - 15 N. Sahu, J. K. Das and J. N. Behera, *Sustain. Energy Fuels*, 2021, **5**, 4992–5000.
 - 16 S. Li, S. Peng, L. Huang, X. Cui, A. M. Al-Enizi and G. Zheng, *ACS Appl. Mater. Interfaces*, 2016, **8**, 20534–20539.
 - 17 S. Chakrabartty, S. Karmakar and C. R. Raj, *ACS Appl. Nano Mater.*, 2020, **3**, 11326–11334.
 - 18 M. Chauhan, K. P. Reddy, C. S. Gopinath and S. Deka, *ACS Catal.*, 2017, **7**, 5871–5879.
 - 19 X. Feng, Q. Jiao, T. Liu, Q. Li, M. Yin, Y. Zhao, H. Li, C. Feng and W. Zhou, *ACS Sustain. Chem. Eng.*, 2018, **6**, 1863–1871.
 - 20 C. Yang, Y. X. Chang, H. Kang, Y. Li, M. Yan and S. Xu, *Appl. Phys. A Mater. Sci. Process.*, 2021, **127**, 1–9.
 - 21 L. Yang, L. Zhang, G. Xu, X. Ma, W. Wang, H. Song and D. Jia, *ACS Sustain.*

- Chem. Eng.*, 2018, **6**, 12961–12968.
- 22 M. Chauhan and S. Deka, *ACS Appl. Energy Mater.*, 2020, **3**, 977–986.
- 23 S. Ji, T. Li, Z. Da Gao, Y. Y. Song and J. J. Xu, *Chem. Commun.*, 2018, **54**, 8765–8768.
- 24 P. Guo, Y. X. Wu, W. M. Lau, H. Liu and L. M. Liu, *J. Alloys Compd.*, 2017, **723**, 772–778.
- 25 Y. Liu, C. Xiao, M. Lyu, Y. Lin, W. Cai, P. Huang, W. Tong, Y. Zou and Y. Xie, *Angew. Chemie Int. Ed.*, 2015, **54**, 11231–11235.
- 26 W. Zhao, C. Zhang, F. Geng, S. Zhuo and B. Zhang, *ACS Nano*, 2014, **8**, 10909–10919.
- 27 S. Gao, X. Wei, H. Fan, L. Li, K. Geng and J. Wang, *Nano Energy*, 2015, **13**, 518–526.
- 28 B. K. Kang, S. Y. Im, J. Lee, S. H. Kwag, S. Bin Kwon, S. N. Tiruneh, M. J. Kim, J. H. Kim, W. S. Yang, B. Lim and D. H. Yoon, *Nano Res.*, 2019, **12**, 1605–1611.
- 29 Y. Z. Chen, R. Zhang, L. Jiao and H. L. Jiang, *Coord. Chem. Rev.*, 2018, **362**, 1–23.
- 30 G. Yilmaz, K. M. Yam, C. Zhang, H. J. Fan and G. W. Ho, *Adv. Mater.*, 2017, **29**, 1–8.
- 31 X. Qin, D. Kim and Y. Piao, *Carbon Energy*, 2021, **3**, 66–100.
- 32 X. Luo, Q. Zhou, S. Du, J. Li, J. Zhong, X. Deng and Y. Liu, *ACS Appl. Mater. Interfaces*, 2018, **10**, 22291–22302.
- 33 Y. Cheng, J. Guo, Y. Huang, Z. Liao and Z. Xiang, *Nano Energy*, 2017, **35**, 115–120.

-
- 34 F. Ming, H. Liang, H. Shi, X. Xu, G. Mei and Z. Wang, *J. Mater. Chem. A*, 2016, **4**, 15148–15155.
- 35 K. Tao, X. Han, Q. Cheng, Y. Yang, Z. Yang, Q. Ma and L. Han, *Chem. - A Eur. J.*, 2018, **24**, 12584–12591.
- 36 M. Nozari-Asbemarz, M. Amiri, A. Khodayari, A. Bezaatpour, S. Nouhi, P. Hosseini, M. Wark, R. Boukherroub and S. Szunerits, *ACS Appl. Energy Mater.*, 2021, **4**, 2951–2959.
- 37 Y. Guo, C. Zhang, J. Zhang, K. Dastafkan, K. Wang, C. Zhao and Z. Shi, *ACS Sustain. Chem. Eng.*, 2021, **9**, 2047–2056.
- 38 H. F. Wang, L. Chen, H. Pang, S. Kaskel and Q. Xu, *Chem. Soc. Rev.*, 2020, **49**, 1414–1448.
- 39 L. Zhou, J. Meng, P. Li, Z. Tao, L. Mai and J. Chen, *Mater. Horizons*, 2017, **4**, 268–273.
- 40 Y. Ma, Y. Ma, D. Bresser, Y. Ji, D. Geiger, U. Kaiser, C. Streb, A. Varzi and S. Passerini, *ACS Nano*, 2018, **12**, 7220–7231.
- 41 B. Chen, G. Ma, Y. Zhu and Y. Xia, *Sci. Rep.*, 2017, **7**, 1–9.
- 42 Z. Huang, S. Yuan, T. Zhang, B. Cai, B. Xu, X. Lu, L. Fan, F. Dai and D. Sun, *Appl. Catal. B Environ.*, 2020, **272**, 118976.
- 43 R. K. Tiwari, I. Shruti and J. N. Behera, *RSC Adv.*, 2021, **11**, 10767–10776.
- 44 N. Sahu, J. K. Das and J. N. Behera, *Inorg. Chem.*, 2022, **61**, 2835–2845.
- 45 S. K. Ramesh, V. Ganesan and J. Kim, *ACS Appl. Energy Mater.*, 2021, **4**, 12998–13005.
- 46 J. G. Li, H. Sun, L. Lv, Z. Li, X. Ao, C. Xu, Y. Li and C. Wang, *ACS Appl.*
-

- Mater. Interfaces*, 2019, **11**, 8106–8114.
- 47 H. Zhang, M. Zou, W. Zhao, Y. Wang, Y. Chen, Y. Wu, L. Dai and A. Cao, *ACS Nano*, 2019, **13**, 3982–3991.
- 48 J. Du, R. Wang, Y. R. Lv, Y. L. Wei and S. Q. Zang, *Chem. Commun.*, 2019, **55**, 3203–3206.
- 49 Z. Xie, H. Tang and Y. Wang, *ChemElectroChem*, 2019, **6**, 1206–1212.
- 50 B. Liu, D. Kong, J. Zhang, Y. Wang, T. Chen, C. Cheng and H. Y. Yang, *J. Mater. Chem. A*, 2016, **4**, 3287–3296.
- 51 Y. Guo, J. Tang, H. Qian, Z. Wang and Y. Yamauchi, *Chem. Mater.*, 2017, **29**, 5566–5573.
- 52 K. Ji, Q. Che, Y. Yue and P. Yang, *ACS Appl. Nano Mater.*, 2022, **5**, 9901–9909.
- 53 Q. Lin, D. Guo, L. Zhou, L. Yang, H. Jin, J. Li, G. Fang, X. Chen and S. Wang, *ACS Nano*, 2022, **16**, 15460–15470.
- 54 K. Srinivas, Y. Chen, X. Wang, B. Wang, M. Karpuraranjith, W. Wang, Z. Su, W. Zhang and D. Yang, *ACS Sustain. Chem. Eng.*, 2021, **9**, 1920–1931.
- 55 J. Wang and H. C. Zeng, *ACS Appl. Mater. Interfaces*, 2019, **11**, 23180–23191.
- 56 D. I. Jeong, H. W. Choi, S. Woo, J. H. Yoo, D. Kang, S. M. Kim, B. Lim, J. H. Kim, S. W. Kim, B. K. Kang and D. H. Yoon, *J. Mater. Chem. A*, 2022, **10**, 16704–16713.
- 57 W. Li, B. Yu, Y. Hu, X. Wang, D. Yang and Y. Chen, *ACS Sustain. Chem. Eng.*, 2019, **7**, 4351–4359.
- 58 Y. Xu, W. Tu, B. Zhang, S. Yin, Y. Huang, M. Kraft and R. Xu, *Adv. Mater.*, 2017, **29**, 1–8.

-
- 59 X. Ma, W. Zhang, Y. Deng, C. Zhong, W. Hu and X. Han, *Nanoscale*, 2018, **10**, 4816–4824.
- 60 M. S. Kim, M. H. Naveen, R. Khan and J. H. Bang, *J. Mater. Chem. A*, 2020, **8**, 7647–7652.
- 61 Q. Wang, Y. Song, D. Sun and L. Zhang, *ACS Omega*, 2021, **6**, 11077–11082.
- 62 L. Chen, G. C. Xu, G. Xu, L. Zhang and H. Ding, *Int. J. Hydrogen Energy*, 2020, **45**, 30463–30472.
- 63 L. Chen, Y. Zhang, H. Wang, Y. Wang, D. Li and C. Duan, *Nanoscale*, 2018, **10**, 21019–21024.
- 64 K. Srinivas, F. Ma, Y. Liu, Z. Zhang, Y. Wu and Y. Chen, *ACS Appl. Mater. Interfaces*, , 2022, 14, 52927–52939.
- 65 Y. Pan, K. Sun, S. Liu, X. Cao, K. Wu, W. C. Cheong, Z. Chen, Y. Wang, Y. Li, Y. Liu, D. Wang, Q. Peng, C. Chen and Y. Li, *J. Am. Chem. Soc.*, 2018, **140**, 2610–2618.
- 66 K. Fan, H. Zou, Y. Lu, H. Chen, F. Li, J. Liu, L. Sun, L. Tong, M. F. Toney, M. Sui and J. Yu, *ACS Nano*, 2018, **12**, 12369–12379.
- 67 W. Chen, H. Wang, Y. Li, Y. Liu, J. Sun, S. Lee, J. S. Lee and Y. Cui, *ACS Cent. Sci.*, 2015, **1**, 244–251.

CHAPTER – 4

Metal–organic framework (MOF) derived flower-shaped CoSe₂ nanoplates as a superior bifunctional electrocatalyst for both oxygen and hydrogen evolution reactions

4.1 Abstract

4.2 Introduction

4.3 Experimental Section

4.3.1 Materials

4.3.2 Synthesis of Co-MOF

4.3.3 Preparation of Co-MOF-derived CoSe₂ (MOF-D CoSe₂)

4.3.4 Synthesis of bare CoSe₂

4.4 Characterization

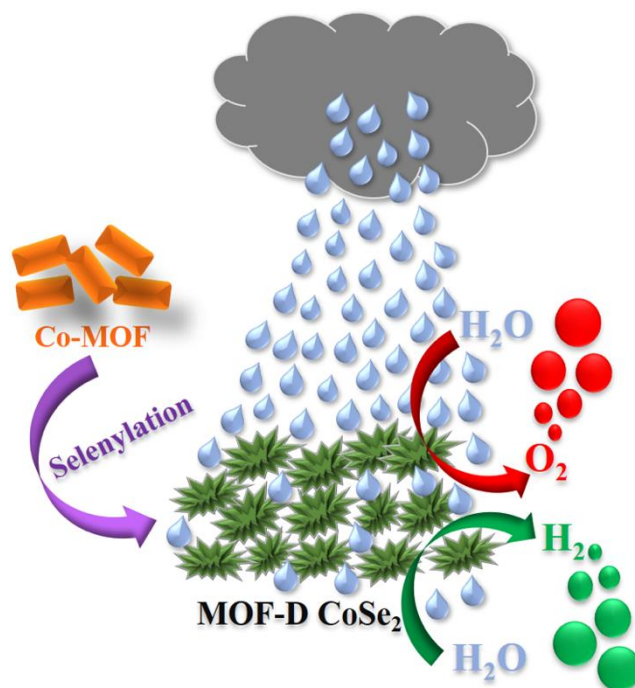
4.5 Electrochemical measurements

4.6 Results and discussion

4.7 Conclusions

4.8 References

4.1 Abstract



The development of a non-precious metal-based stable and cost-effective bifunctional electrocatalyst remains a significant challenge for the production of hydrogen (H₂) and oxygen (O₂) through water splitting. Although some progress has been made to develop efficient electrocatalysts from transition metal-based nanostructured selenides, the electrocatalyst derived from metal-organic framework (MOF) transition metal selenides demand additional effort due to their well-defined morphological structure and high accessible surface area resulting in better electrochemical performances. Herein, by tuning the selenylation technique through a facile solvothermal approach, we have successfully synthesized flower-like CoSe₂ nanoplates termed MOF-D CoSe₂, derived from a Co-MOF of the formula [Co₃(tiron-bpy)₂(bpy)(H₂O)₈].(H₂O)₂ [tiron = 4,5-dihydroxy-1,3-benzenedisulfonate disodium salt, and bpy = 4,4'-bipyridyl]. The MOF-D CoSe₂ performs as an excellent bifunctional electrocatalyst, which requires an overpotential of 320 mV to achieve the predefined current density of 10 mA cm⁻², with a Tafel slope of 60 mV dec⁻¹ in 1 M KOH to catalyze the oxygen evolution reaction

(OER). For the hydrogen evolution reaction (HER), MOF-D CoSe₂ needs an overpotential of 195 mV at 10 mA cm⁻² current density and a low Tafel slope of 43 mV dec⁻¹ in an acidic medium of 0.5 M H₂SO₄. The enhanced bifunctional electrochemical performance of the MOF-D CoSe₂ electrocatalyst has been attributed to the combination of a unique flower-shaped morphology with a plate-like nanoarchitecture, higher electrochemical active surface area and robust stability in both acidic as well as alkaline media.

4.2 Introduction

The progress of modern society and its growing economy are always more conscious about sustainable energy carriers and their commercial use.¹ The evolution of hydrogen through a simple electrolysis process is a clean and green energy source and an alternative chemical fuel, which could be used as the substitute of traditional fossil fuels to fulfill the future energy demands.^{2,3} The higher specific energy and zero-carbon emission capability of hydrogen make it a front-line energy source for coming decades.⁴ Electrochemical water splitting is the safest process, with the half-cell cathodic reaction corresponding to the hydrogen evolution reaction (HER) and half-cell anodic reaction to the oxygen evolution reaction (OER). The water-splitting process is a surface phenomenon, and it is very sluggish due to the multi-step reaction kinetics of the electron coupling or decoupling process.⁵ Overcoming all these types of kinetic barriers in the electrolytic medium and to lower the additional potential required with respect to the thermodynamic potential of water splitting of 1.23 V strongly depends upon the use of promising electrocatalysts. To date, precious metals such as platinum (Pt) are best for hydrogen evolution, and the oxides of ruthenium (RuO₂) and iridium (IrO₂) are broadly used for oxygen evolution catalytic activity.^{6,7} The use of these precious metals

is limited because of their high cost and low commercial availability; thus, it is urgent to minimize the use of familiar noble metals and to develop alternative low cost, eco-friendly and non-precious electrocatalysts whose catalytic performance is closer to that of the precious ones.⁸⁻¹¹ In recent years, various nanostructures of noble metal-free electrocatalysts such as transition metal-based phosphides,¹²⁻¹⁵ sulphides,¹⁶⁻²¹ selenides,²²⁻²⁴ oxides,²⁵⁻²⁸ and nitrides¹³ have been used as the prominent electrocatalyst in the fields of energy storage and conversion.^{29,30} In particular, first-row transition metal-based selenides have gathered great attention in the field of energy sector because of their cost-effectiveness, reliability, superior electronic properties and good catalytic activity.^{9,10,30-32} The characteristic metallic features of pristine CoSe₂ show better catalytic performances due to its easy transport of ions to the surface onto the electrodes.³³⁻³⁵ Although many research groups explored their research on carbon-coated or metal-doped, or hetero structure-based CoSe₂ as a superior mono or bifunctional electrocatalyst, the presence of limited active sites and easy aggregation restrict the efficacy behind the searching of an efficient electrode material for energy conversion performances.^{34,36-38} Metal-organic frameworks (MOFs) are a well-known organic-inorganic porous hybrid material composed of various organic ligands and metal clusters or ions. The presence of large surface area, high porosity and active reaction sites pull great attention towards the research areas of energy storage, sensing, gas storage and energy conversion processes. But the poor electrical conductivity of the MOF materials restricts their use as an electrocatalyst in the electrolysis process.³⁹⁻⁴³ In recent studies, different MOF-derived CoSe₂, and cobalt MOF selenylation techniques were employed to synthesize efficient and durable electrocatalysts for simple water splitting. By following the MOF-derived selenylation strategy, Chen's group synthesized N-doped graphitic carbon-based CoSe₂ on carbon nanotubes and

tested its application towards a dual functional electrocatalyst.³⁴ The additional potential or overpotential of 185 mV and 340 mV were required to deliver the predefined current density of 10 mA cm⁻² for the HER and OER, corresponding to Tafel slopes of 98 and 107 mV dec⁻¹, respectively. Fang et al. developed a porous CoSe₂ on carbon cloth derived from MOFs with an etching and selenylation process and studied energy conversion and storage applications.⁴⁰ Fan et al. have derived CoSe₂ microspheres from the selenylation of Co-MOF under an argon atmosphere and made it a promising electrocatalyst for the oxygen evolution reaction.⁴⁴ Dong et al. synthesized a MOF-derived Zn doped CoSe₂ and verified its OER performances in terms of an additional potential of 356 mV at 10 mA cm⁻² and a Tafel value of 88 mV dec⁻¹, respectively.³⁷ The controlled synthesis with various morphological structures due to high surface area and good electrical conductivity gives a better electrocatalyst for water splitting in both the HER and OER.⁴⁵ To avoid the above multi-step unvarying selenylation process with high-temperature annealing under an inert atmosphere, the facile synthesis of MOF-derived metal selenides as an efficient electrocatalyst by following simple selenylation based on the solvothermal process is practically more sensible.

Herein, we have successfully synthesized promising free-standing jasmine-flower like CoSe₂ nanoplates termed MOF-D CoSe₂ electrocatalyst derived from our recently reported cobalt MOF precursor ([Co₃(tiron-bpy)₂(bpy)(H₂O)₈].(H₂O)₂).⁴⁶ This approach includes a simple selenylation process of Co-MOF with selenium powder through a one-step solvothermal technique to obtain a cost-effective bifunctional electrocatalyst with respect to both hydrogen and oxygen evolution reactions. The synthesized electrode material displays excellent OER performance with a lower overpotential of 320 mV at 10 mA cm⁻² and a Tafel slope of 60 mV dec⁻¹ in an alkaline

solution. Additionally, the MOF-D CoSe₂ shows good hydrogen evolution activity in terms of an acceptable overpotential of 195 mV at 10 mA cm⁻² current density and a Tafel value of 43 mV dec⁻¹ in an acidic electrolytic medium. Moreover, the robustness of the as-synthesized bifunctional electrode material was further evaluated with a long-term durability test.

4.3 Experimental section

4.3.1 Materials

Co(NO₃)₂·6H₂O, N,N'-dimethylformamide (DMF), 4,4'-bipyridyl (bpy), 4,5-dihydroxy-1,3-benzenedisulfonate disodium salt (tiron), selenium powder, NaBH₄, and Nafion solution were acquired from both Sigma-Aldrich and Himedia Chemicals. All the chemicals were used without further processing. Deionized water was used for the preparation of all the electrolyte solutions and washing of the as-synthesized materials.

4.3.2 Synthesis of Co-MOF

The Co-MOF precursor [Co₃(tiron-bpy)₂(bpy)(H₂O)₈].(H₂O)₂ was prepared by taking 4,4'-bipyridyl and tiron as ligands as per our recently reported work.⁴⁶ In a reaction procedure, 0.078 g of 4,4'-bipyridyl and 0.166 g of tiron were dissolved in 10 mL of deionized water and continued to stir for 30 minutes. Further, 0.145 g of Co(NO₃)₂·6H₂O was mixed with the solution precursor and left for stirring for 1 h. Afterwards, the as-obtained solution was transferred into a 23 mL Teflon-lined digestion bomb and kept in a pre-heated oven at 140 °C for 72 h to get orange colour plate-shaped crystals with the formula [Co₃(tiron-bpy)₂(bpy)(H₂O)₈].(H₂O)₂.

4.3.3 Synthesis of Co-MOF-derived CoSe₂ (MOF-D CoSe₂)

In a synthetic procedure, 0.0316 g of selenium powder and 0.0189 g of NaBH₄ were dissolved in 6 mL of dimethylformamide and left for stirring until a homogeneous black precursor was observed. Herein, NaBH₄ has been used as a reducing agent. Further 0.081 g of Co-MOF was then added to the black colour solution and continued stirring for 1 h. The as-prepared solution mixture was transferred into a 23 mL Teflon lined digestion bomb and heated at 200 °C for 24 h. The black colour material was collected by centrifugation and washed thoroughly with deionized water and ethanol. The obtained product was further dried at 60 °C overnight to get the black powder sample of CoSe₂.

4.3.4 Synthesis of bare CoSe₂

Bare CoSe₂ was prepared by following the similar reaction conditions to those of the MOF derived CoSe₂ (MOF-D CoSe₂), by taking cobalt nitrate hexahydrate as the starting material instead of Co-MOF precursor.

4.4 Characterization

A powder diffraction system (Bruker D8 Advance diffractometer) furnished with Cu-K α radiation of wavelength $\lambda = 1.5418 \text{ \AA}$ has been used to analyze the crystallinity of the as-synthesized material. Morphological study and elemental mapping analysis of the samples were performed using a field emission scanning electron microscope (FESEM, Merlin Compact with a GEMINI-I electron column, Zeiss Pvt. Ltd., Germany) and a transmission electron microscope (equipped with HRTEM, JEOL 2100F, operated at 200 kV). The chemical state of the material has been well studied with the help of X-ray photoelectron spectroscopy using a PHI Versa Probe III. The surface area measurements were carried out by Brunauer-Emmett-Teller (BET) analysis using a Quantachrome Autosorb instrument.

4.5 Electrochemical measurements

All the electrochemical studies have been carried out with the help of a standard three-electrode measurement setup. The as-prepared sample modified glassy-carbon electrode (surface area of 0.07 cm²) was used as the working electrode, a platinum wire as the auxiliary electrode, and Hg/HgO as the reference electrode for the OER. However, the aqueous Ag/AgCl was used as a standard reference electrode for the HER study. Linear sweep voltammograms or the polarization curves were recorded at a sweep rate of 5 mV s⁻¹. A catalyst slurry was prepared by the combination of 1 mg of an active sample with ethanol and Nafion mixture followed by ultra-sonication to get a homogeneous catalyst ink. The mass loading of the sample throughout all the electrochemical measurements was taken as 0.25 mg cm⁻². Although the electrochemical measurements have been recorded in aqueous Ag/AgCl as the reference electrode for the HER and Hg/HgO reference electrode for the OER, here we presented all the recorded data throughout the manuscript on the reversible hydrogen electrode (RHE) scale as per the Nernst equation as follows;^{5,47,48}

$$E_{RHE} = E_{Ag/AgCl} + 0.0591 (pH) + 0.21 V \quad (1)$$

$$E_{RHE} = E_{Hg/HgO} + 0.0591 (pH) + 0.098 V \quad (2)$$

Electrochemical impedance spectrum (EIS, commonly known as Nyquist plot) was recorded in a potentiostatic mode at -0.21 V vs. RHE by applying an AC amplitude of 5 mV in the frequency window of 1 MHz to 0.1 Hz for the HER in 0.5 M H₂SO₄ and 1.52 V vs. RHE for the OER in 1 M KOH respectively. Further, *iR* correction has been carried out in a similar frequency region to that taken in EIS to minimize the catalyst and electrolyte resistance to achieve the actual catalytic performances of the electrode materials. Herein,

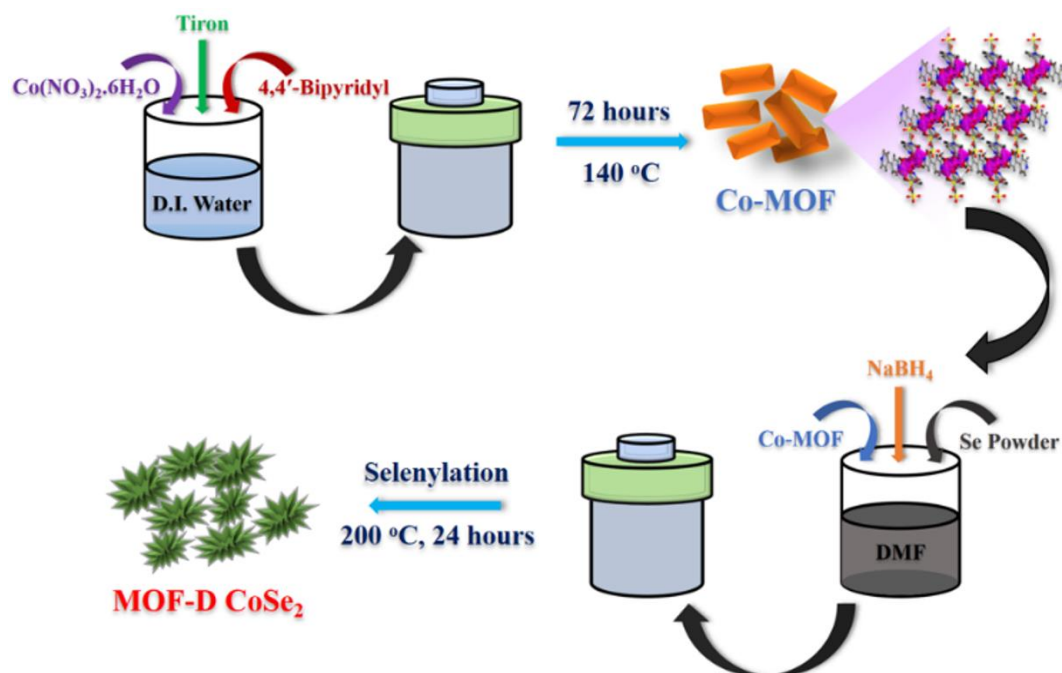
“*R*” is the solution resistance and “*i*” is the current, respectively. The Tafel slopes (plot of $\log J$ vs. overpotential) were obtained as per the following equation;⁴⁹

$$\eta = a + b \log j \quad (3)$$

Where η , a , b , and J are known as the overpotential, Tafel constant, Tafel slope, and current density, respectively. Electrochemical active surface area for all the as-prepared samples was estimated from the double-layer capacitance (C_{dl}) obtained from the non-Faradaic region of cyclic voltammograms at various scan rates (10 to 200 mV s^{-1}). The half of the difference of positive and negative current densities ($\Delta J = J_a - J_c$) is plotted against different scan rates where the C_{dl} value is equal to the linear slope.

4.6 Results and discussion

The synthesis of flower-shaped MOF-derived CoSe₂ nanoplates named MOF-D CoSe₂, has been carried out in a facile two-step method following the hydro/solvothermal approach (Scheme 4.1).



Scheme 4.1: Schematic diagram for the synthesis of MOF-D CoSe₂.

The cobalt-MOF was prepared by a hydrothermal technique in the first step, followed by the solvothermal selenylation to obtain the free-standing MOF-D CoSe₂. The phase purity of the as-prepared Co-MOF and MOF-D CoSe₂ has been verified by powder X-ray diffraction study. The crystal structure and the X-ray diffraction of the Co-MOF precursor are presented in **Figure 4.1**. The crystalline nature of the sample, corresponding to the sharp diffraction peaks of MOF-D CoSe₂, exhibits the presence of different planes of (011), (101), (111), (120), (200), (211), (121), (211), (002) (031), (131) and (122) of the orthorhombic crystal system (PDF 00-053-0449) as shown in **Figure 4.2**. The powder diffraction data are well consistent with the above existing data file, indicating no other impurities, resulting in high phase purity of the MOF-D CoSe₂ sample.

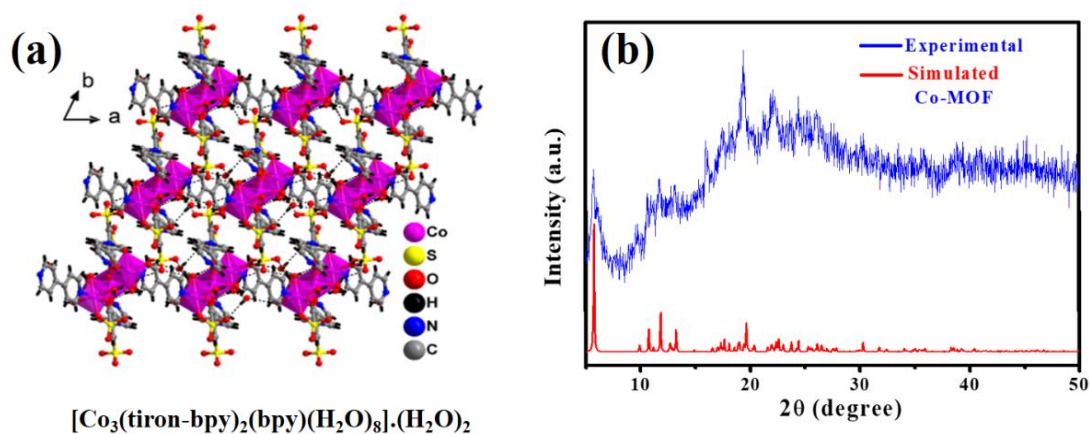


Figure 4.1: Crystal structure (a) and corresponding PXRD of Co-MOF (b).

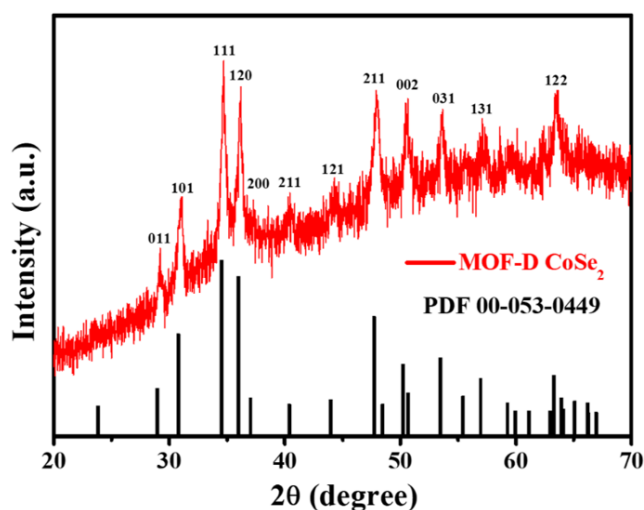


Figure 4.2: PXRD of MOF-D CoSe₂.

A scanning electron microscope (SEM) was used at different magnifications to perform the morphological structure analysis of the as-prepared samples. It has been observed that the pristine Co-MOF precursor shows a regular arrangement of a rectangular capsule type morphology before the selenylation process as shown in **Figure 4.3**. The uniform distribution of the flower-like morphology throughout the material is found in **Figure 4.4a**. However, **Figure 4.4b** gives a clear view of the flower-like MOF-D CoSe₂. Interestingly, the shape of the flower looks like a jasmine flower (**Figures 4.4c and d**). The morphological information obtained from the SEM images of the MOF-D CoSe₂ was further confirmed with transmission electron microscope (TEM) analysis in **Figure 4.5**. The TEM study of MOF-D CoSe₂ at different magnifications confirms that the petals are generally nanoplates which aggregates to give a flower-like morphology (**Figures 4.5a and b**). The well-resolved lattice fringes were further studied by HRTEM analysis in **Figures 4.5c and d**. Two distinct lattice fringes were observed with the inter-planar distance of 0.248 and 0.290 nm, corresponding to the d-spacing value of (120) and (101) planes, respectively. The inset in **Figure 4.5d** presents the selected area electron diffraction (SAED) pattern, confirming the high crystallinity of the as-synthesized MOF-D CoSe₂ material.

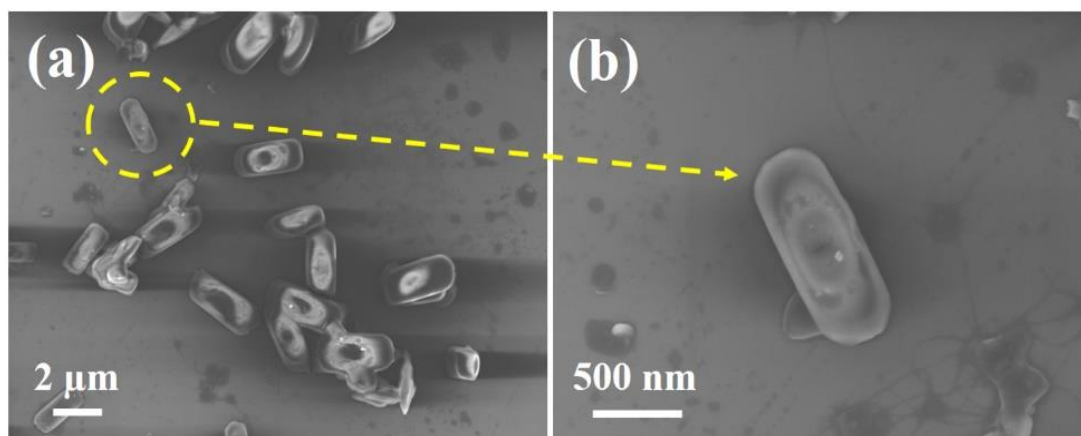


Figure 4.3: SEM images of Co-MOF.

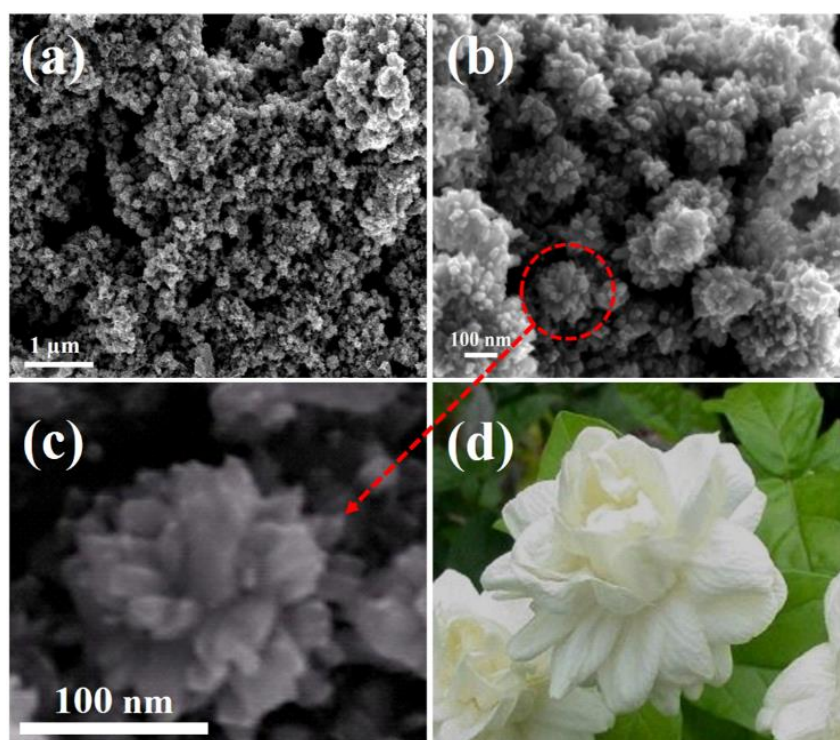


Figure 4.4: FESEM images of flower-shaped MOF-D CoSe_2 at different magnifications (a-d).

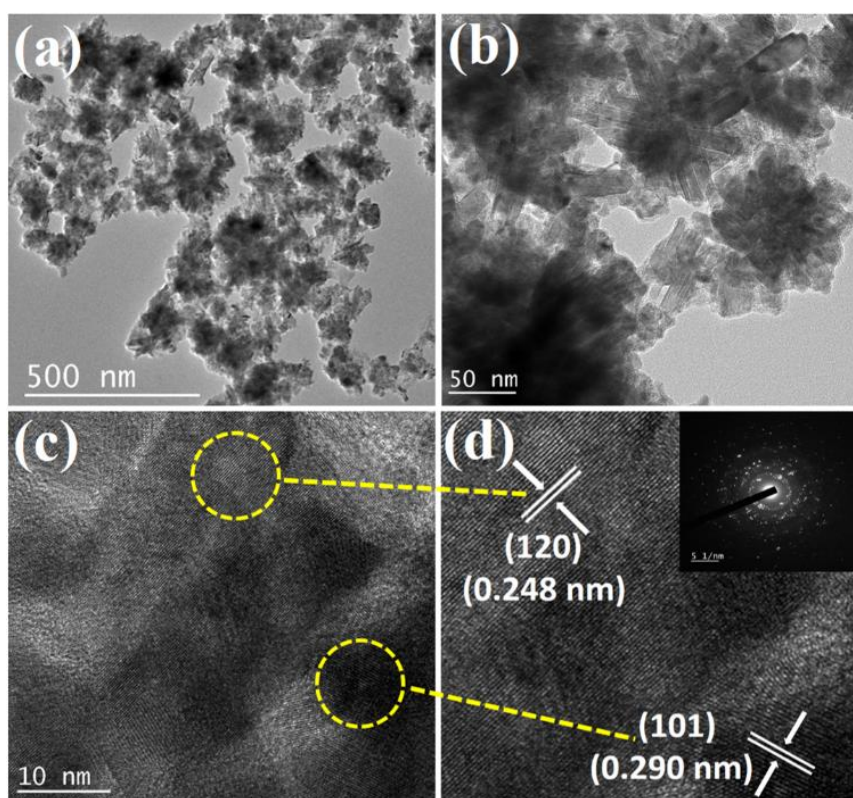


Figure 4.5: TEM images of the MOF-D CoSe_2 at different magnifications (a, b) and (c, d) are the high-resolution TEM images of MOF-D CoSe_2 ; the inset in (d) presents the SAED pattern of MOF-D CoSe_2 .

Furthermore, X-ray photoelectron spectroscopy (XPS) was carried out to verify the chemical state of the MOF-D CoSe₂. As shown in **Figure 4.6a** the as-prepared MOF-D CoSe₂ is composed of Co, Se, C and O. The high-resolution XPS of Co 2p and Se 3d are shown in **Figures 4.6b and c**. The observed peak positions of Co 2p_{3/2} at the binding energies of 778.6 eV and Co 2p_{1/2} at 793.5 eV show the existence of Co–Se bonds corresponding to CoSe₂, where Co is in the +2 oxidation state due to the presence of Se₂²⁻ dimer as shown in **Figure 4.6b**.^{50–52} In addition, peaks of Co 2p_{3/2} and Co 2p_{1/2} at a binding energy of 780.2 and 796.4 eV respectively, show the existence of the Co–O bond due to partial surface oxidation of MOF-D CoSe₂.^{33,53} However, the satellite peaks at the higher binding energies of 784.3 eV and 801.4 eV correspond to the antibonding orbital of both Co and Se atoms.^{33,44} The presence of Se atoms in CoSe₂ was verified at the binding energies of 54.6 eV for Se 3d_{5/2} and 55.3 eV for Se 3d_{3/2}, respectively, as shown in **Figure 4.6c**. Moreover, a noticeable broad peak was observed in the binding energy region of 59.5 eV which shows the presence of surface oxidized selenium (SeO_x).^{52,54–56}

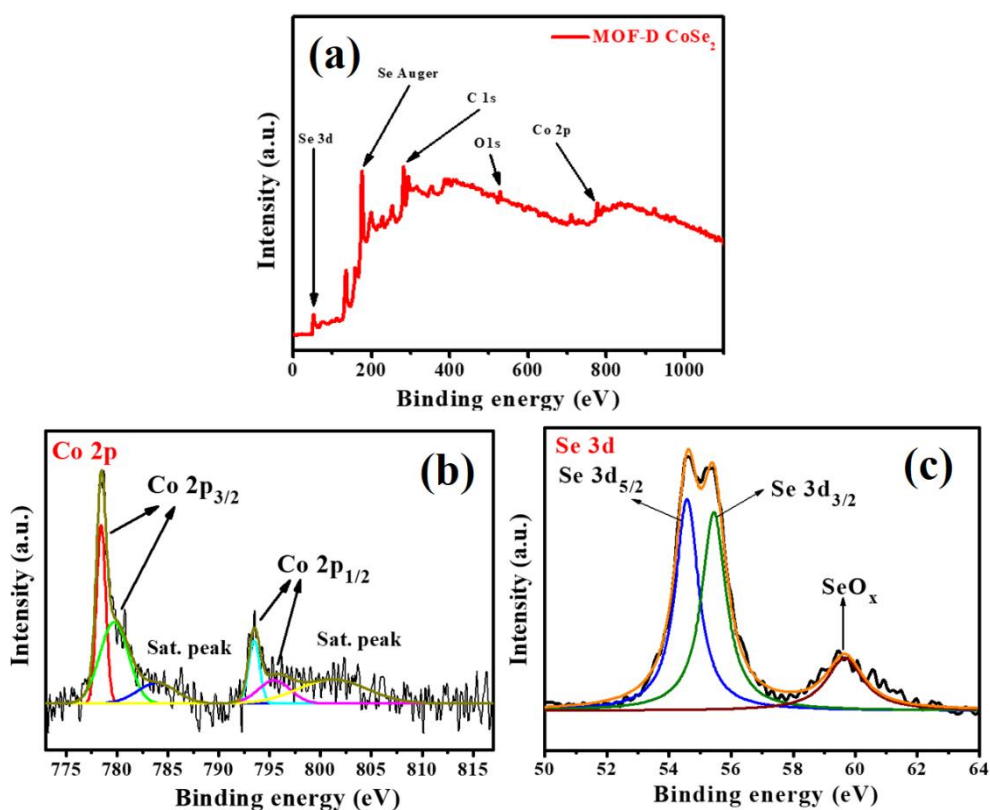


Figure 4.6: Full-scan XPS survey spectrum of MOF-D CoSe₂ (a), deconvoluted XPS data of Co 2p (b), Se 3d (c).

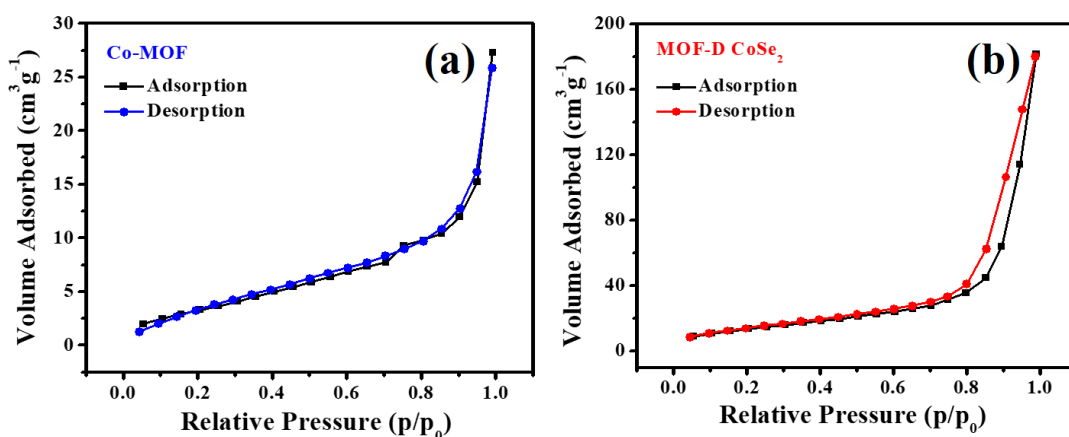


Figure 4.7: BET analysis of Co-MOF (a), MOF-D CoSe₂ (b).

The specific surface areas for both Co-MOF and MOF-D CoSe₂ were determined by BET analysis and were found to be 12.192 m² g⁻¹ and 49.851 m² g⁻¹ for bare Co-MOF and MOF-D CoSe₂ respectively (**Figures 4.7a and b**). The higher specific surface area

of MOF-D CoSe₂ contributes to better electrochemical performance than the Co-MOF having a lower surface area.

The electrochemical analysis of the as-synthesized flower-shaped MOF-D CoSe₂ nanoplates was carried out in a three-electrode measurement setup. The supporting electrolyte used for all the electrochemical measurements was 1 M KOH for the OER and 0.5 M H₂SO₄ for the HER, respectively. At first, the activity towards the oxygen evolution reaction of the Co-MOF derived CoSe₂ (i.e., MOF-D CoSe₂) electrode material was evaluated in an alkaline electrolytic solution of 1 M KOH. The catalytic behaviour towards the oxygen production with respect to a higher anodic current density of MOF-D CoSe₂ shows dominant OER activity compared to Co-MOF, bare CoSe₂, and commercial RuO₂. The linear sweep voltammetry (LSV) plots for all the samples were recorded at a sweep rate of 5 mV s⁻¹, as shown in **Figure 4.8a**. The as-synthesized MOF-D CoSe₂ requires an overpotential of 320 mV to achieve a current density of 10 mA cm⁻², which is much lower than that of the Co-MOF (410 mV), bare CoSe₂ (417 mV) and standard RuO₂ (370 mV), respectively. All the polarization curves have been *iR* corrected and presented in **Figure 4.9**. The Tafel slope dealing with the surface kinetics of the electrode material was calculated from the linear fitting of the plot between overpotential and logarithm of current density as illustrated in **Figure 4.8b**. The calculated Tafel slope value of MOF-D CoSe₂ (60 mV dec⁻¹) is lower than that of the Co-MOF (70 mV dec⁻¹), bare CoSe₂ (73 mV dec⁻¹) and commercial RuO₂ (66 mV dec⁻¹). This lower value of overpotential and Tafel slope of MOF-D CoSe₂ indicates its excellent OER activity compared to some other reported literatures shown in **Table 4.1**.

The frequency response between the modified electrode materials with the electrolyte solution has been recorded by EIS (electrochemical impedance spectroscopy) with an

applied amplitude of 5 mV in the frequency of 1 MHz to 0.1 Hz. The compared EIS data of the MOF-D CoSe₂, bare CoSe₂ and Co-MOF at a potential of 1.52 V vs. RHE shows the electrochemical response (interaction of the electrode surface to the electrolyte) of all the samples. The obtained lower charge transfer resistance of MOF-D CoSe₂ compared to Co-MOF and bare CoSe₂ indicate its faster charge transfer capability, as shown in **Figure 4.8c**.⁵⁷ Moreover, the long-term stability test of the as-prepared CoSe₂ electrode material was performed by the chronopotentiometry (CP) measurement as shown in **Figure 4.8d**. During the 16 h durability test, the as-prepared CoSe₂ modified electrode material was significantly stable up to 7 h of constant electrolysis with negligible change in overpotential. However, the periodic increase in overpotential after 7 h of electrolysis reveals that the material is not stable up to the mark under the harsh alkaline conditions.

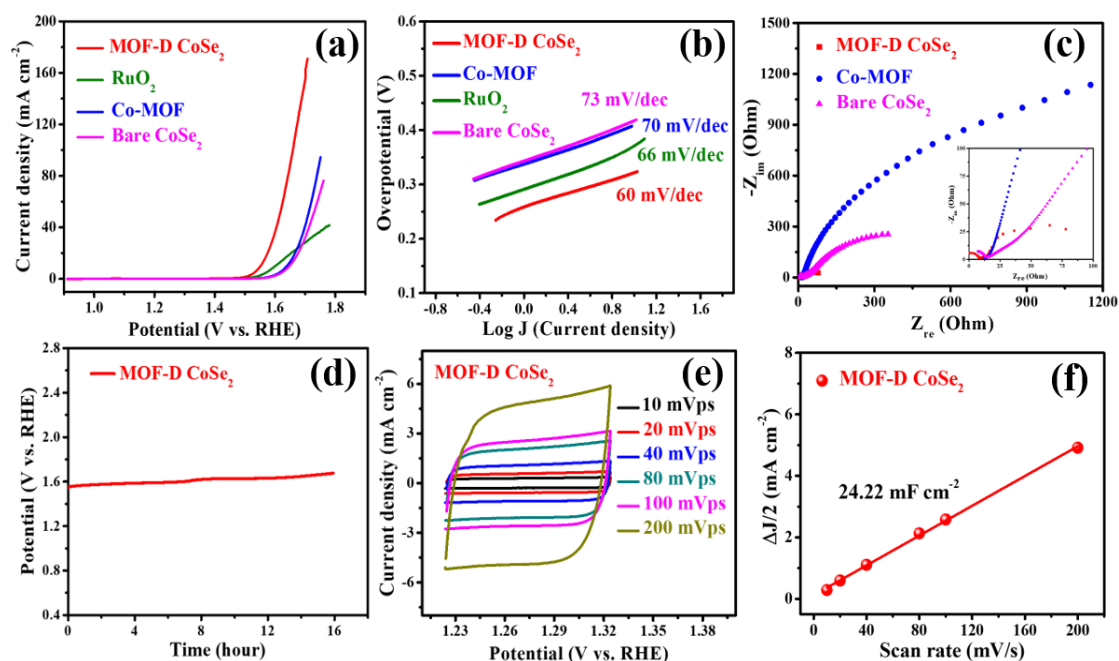


Figure 4.8: LSVs of MOF-D CoSe₂, Co-MOF, bare CoSe₂ and RuO₂ (a), corresponding Tafel slopes of MOF-D CoSe₂, Co-MOF, bare CoSe₂ and RuO₂ (b), EIS of MOF-D CoSe₂, bare CoSe₂ and Co-MOF (c), stability of MOF-D CoSe₂ in alkaline electrolytic environment (d), CV of MOF-D CoSe₂(e), C_{dl} of MOF-D CoSe₂ (f).

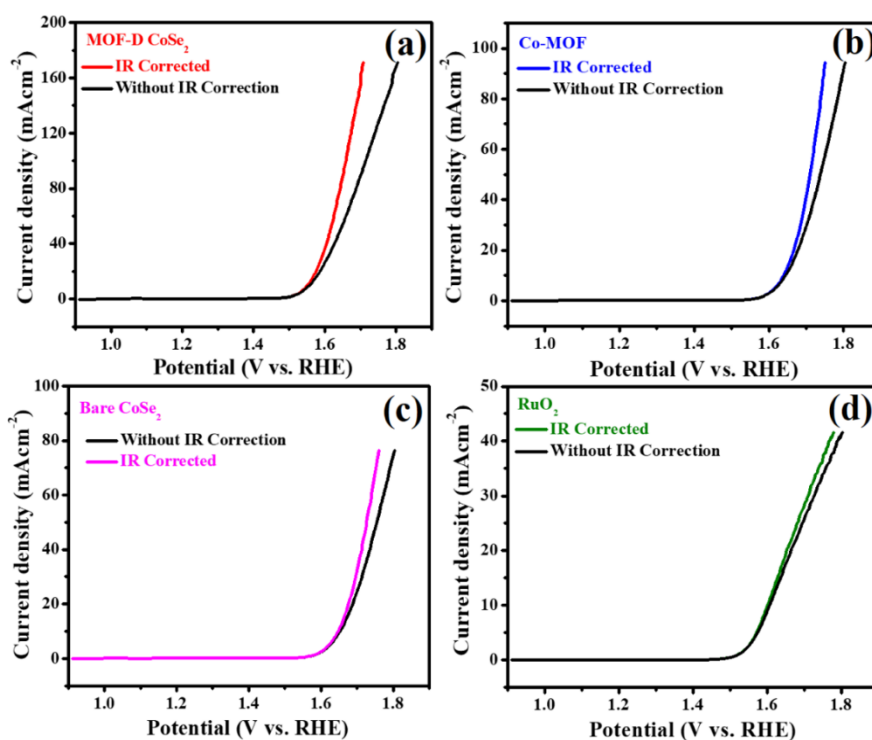


Figure 4.9: LSV plots of (a) MOF-D CoSe₂, (b) Co-MOF, (c) bare CoSe₂ and (d) RuO₂ for oxygen evolution reaction before and after iR compensation.

The high catalytic activity of the as-synthesized MOF-D CoSe₂ electrocatalyst was further verified by the presence of a higher electrochemical active surface area (ECSA). A specific potential window in which there is minimal Faradaic current response is estimated by the standard CV technique. The current measured in this region is assumed to be a charging current that arises due to double-layer charging.⁵⁸ However, ECSA has a linear relationship with the electrochemical double-layer capacitance (C_{dl}) that originates through an interfacial charging process.⁵⁹ By plotting the charging current versus scan rate in a certain potential window (1.22 V vs. RHE to 1.32 V vs. RHE) a straight line was obtained with a slope equivalent to twice the double layer capacitance (C_{dl}), which is used to represent the ECSA,⁶⁰ as shown in **Figures 4.8e and f**. The C_{dl} value for the OER efficient MOF-D CoSe₂ electrode material was found to be 24.22 mF cm⁻². Mainly, the C_{dl} value is directly correlated with ECSA which is an alternative

method to evaluate ECSA.^{38,61} The high ECSA of MOF-D CoSe₂ demonstrates its efficacy as an efficient electrocatalyst for oxygen production.

After a long-term electrolysis process, the post-stability analysis was further used to evaluate the efficacy of the modified electrode material. **Figures 4.10a and b** shows the PXRD pattern and FESEM image of the electrocatalyst after stability process. It has been observed that after the durability test under alkaline conditions, a sharp noticeable change in phase purity was observed due to the surface oxidation of MOF-D CoSe₂, which is responsible for the catalytic activity in an alkaline medium, indicating the presence of active CoOOH, CoSeO₄ and CoO phases for the OER. The reconstructed CoOOH acts as an active catalyst on the surface of the electrode material during the OER process.^{33,34,62,63} Moreover, a distorted morphology has been observed in FESEM after the long-term durability test.

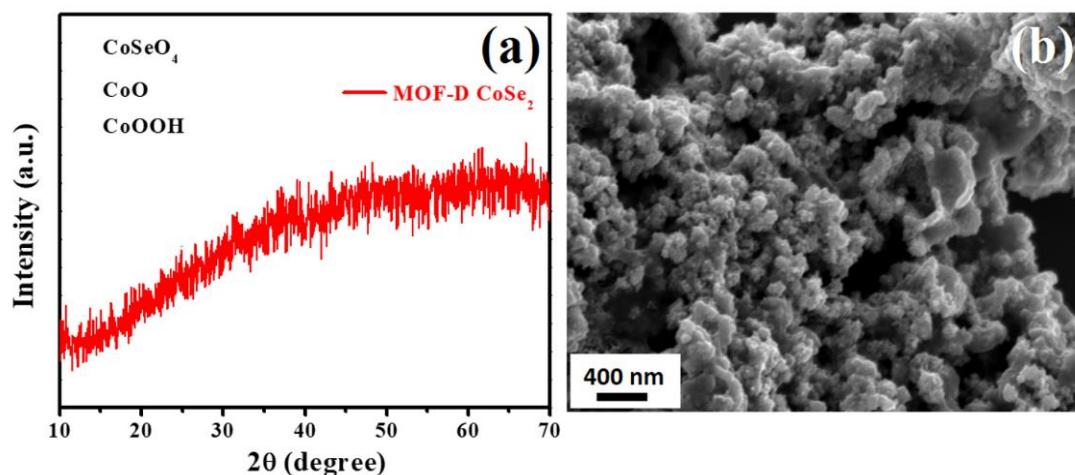


Figure 4.10: PXRD (a) and SEM (b) of MOF-D CoSe₂ after OER stability test.

The unique flower-like morphology of MOF-D CoSe₂ nanoarchitecture leads to developing a platform of high surface area and a large number of active sites, which exhibits enhanced OER performance and also shows good hydrogen evolution activity. Therefore, the HER study with respect to the polarization curves of the MOF-D CoSe₂,

bare CoSe₂, and the Pt/C modified material on a glassy carbon electrode (GCE) is shown in **Figure 4.11a**. The catalytic activity of the MOF-D CoSe₂ required 195 mV overpotential, lower than that for the bare CoSe₂ (262 mV) to deliver the predefined current density of 10 mA cm⁻². The Co-MOF was inactive for HER in acidic media. The linear sweep voltammetry (LSV) curves were plotted after *iR* correction and are shown in **Figure 4.12**.

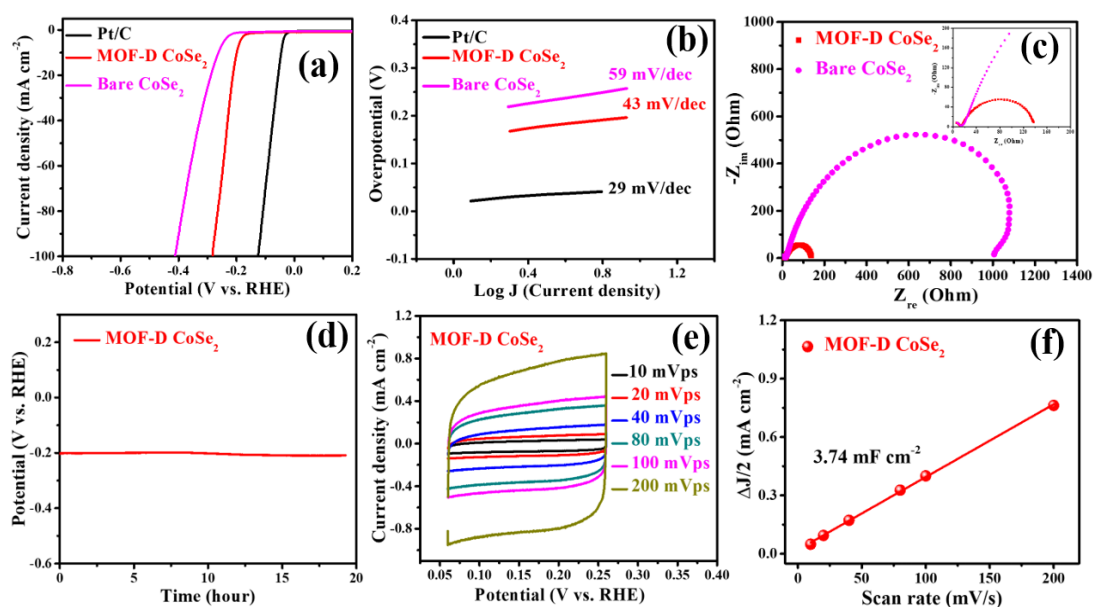


Figure 4.11: LSVs of MOF-D CoSe₂, bare CoSe₂ and Pt/C (a), corresponding Tafel slopes of MOF-D CoSe₂, bare CoSe₂ and Pt/C (b), EIS of MOF-D CoSe₂, bare CoSe₂ (c), CP stability of MOF-D CoSe₂ in an acidic electrolytic medium (d), CV of MOF-D CoSe₂ (e), C_{dl} of MOF-D CoSe₂ (f).

The Tafel slope value determined the surface kinetics of the electrocatalytic process as shown in **Figure 4.11b**, which gives a detailed study about the actual reaction mechanism occurring between the electrolyte and the electrode interface. The lower value of the Tafel slope demonstrates the efficient catalytic behaviour of the electrocatalyst used for water electrolysis. The obtained lower value of the Tafel slope of 43 mV dec⁻¹ shows the faster reaction kinetics of ion adsorption and desorption processes onto the surface of the electrode. The as-prepared electrocatalyst follows the

Volmer–Heyrovsky path instead of Volmer-Tafel compared to precious metals such as Pt/C (29 mV dec⁻¹).^{64,65} The HER performance comparison of the as-synthesized sample with the reported studies in terms of overpotential and Tafel slope has been illustrated in **Table 4.2**. The EIS data displays the smooth charge transfer capability of the electrocatalyst as shown in **Figure 4.11c**. The EIS measurement was carried out within a lower to higher frequency range of 1 MHz to 0.1 Hz at an applied AC amplitude of 5 mV. The series resistance (R_s) and charge transfer resistance (R_{ct}) of the MOF-D CoSe₂ were found to be 13 Ω and 124 Ω at a potential of -0.21 V vs. RHE. Moreover, the long-term durability test of the as-synthesized MOF-D CoSe₂ sample was performed by the chronopotentiometry technique as presented in **Figure 4.11d**. After 19 h of constant HER electrolysis, there is negligible change in overpotential of the electrocatalyst, showing the efficient nature of the electrode material in an acidic medium.

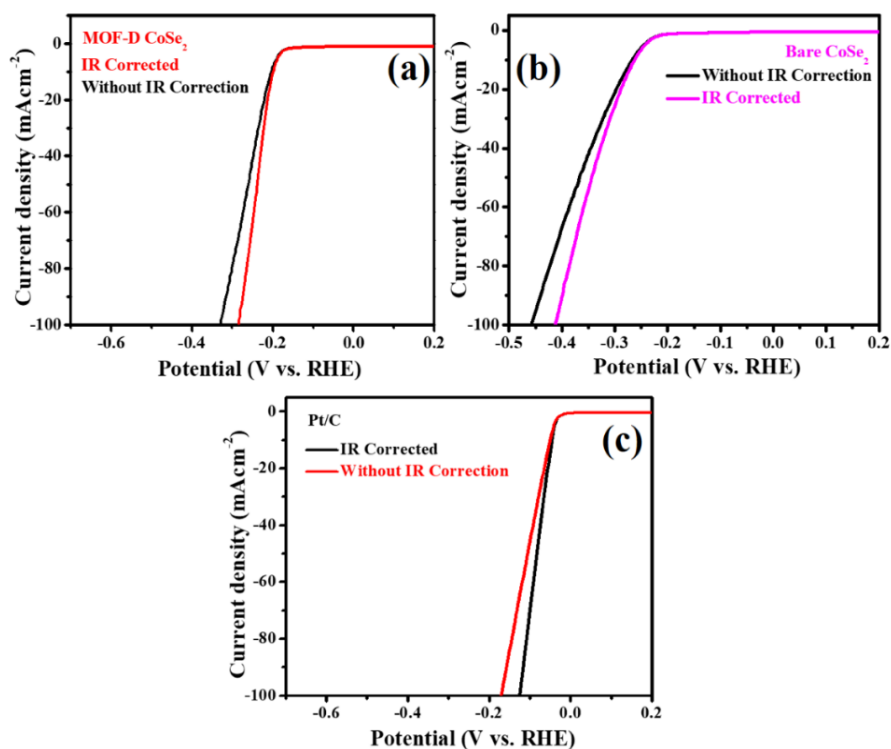


Figure 4.12: LSV plots of (a) MOF-D CoSe₂, (b) bare CoSe₂, (c) Pt/C for hydrogen evolution reaction before and after iR compensation.

Additionally, to investigate the electrochemical active surface area (ECSA) of the as-synthesized sample, we performed cyclic voltammetry (CV) in a precise potential window (0.06 V vs. RHE to 0.26 V vs. RHE) at different scan rates to estimate double-layer capacitance (C_{dl}), as shown in **Figure 4.11e**. The (C_{dl}) value of MOF-D CoSe₂ was found to be 3.74 mF cm⁻², corresponding to the high value of the electrochemical active surface area (**Figure 4.11f**). This high value accelerates the enhanced HER activity. Furthermore, the post stability analysis of the MOF-D CoSe₂ by powder diffraction showed that there is no change in phase purity (**Figure 4.13a**). The post stability FESEM picture showed a slight distortion of the flower-shaped surface morphology of the sample after 19 h of constant electrolysis in the acidic medium as displayed in **Figure 4.13b**.

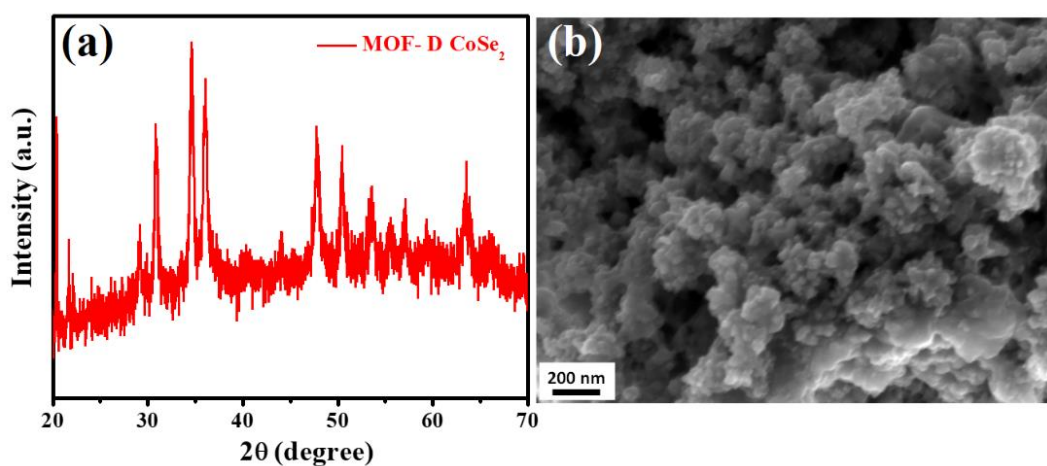


Figure 4.13: PXRD (a) and FESEM (b) of MOF-D CoSe₂ after HER durability test.

Based on the electrochemical performance of the electrocatalyst, we presume that the unique solvothermal selenylation of MOF-D CoSe₂ corresponds to the flower-like morphology, resulting in higher electrochemical active surface area and better catalytic activity for the OER and HER which could be used as a suitable electrocatalyst for future energy processes.

Table 4.1: OER Comparison table for MOF-D CoSe₂ with reported literature.

Sl No.	Sample	Overpotential @10mA/cm ²	Tafel slope	Electrolyte used	References
1	CoSe ₂ -160 microcubes	328 mV	73.0 mV/dec	1 M KOH	Inorg. Chem. 2020, 59, 12778–12787
2	CoSe ₂ @N/C-CNT	340 mV	103.0 mV/dec	1 M KOH	J. Colloid Interf. Sci. 2020, 566, 296-303
3	CoSe ₂ -450 microspheres	330 mV	79.0 mV/dec	1 M KOH	J. Mater. Chem. A, 2017, 5, 15310-15314
4	CoSe ₂ /CNTs	324 mV	76.0 mV/dec	1 M KOH	Electrochim. Acta 2020, 331, 135362
5	Ni _{0.88} Co _{1.22} Se ₄ hollow microparticles	320 mV	78.0 mV/dec	1 M KOH	Chem. Mater. 2017, 29, 7032-7041
6	hollow core-branch CoSe ₂	320 mV	107.0 mV/dec	1 M KOH	Small 2018, 14, 1700979
7	CoSe ₂ @NC nanorods	310 mV	95.0 mV/dec	1 M KOH	J. Alloy. Compound 2019, 778, 134-140
8	FeCoSe ₂ /Co _{0.85} Se	330 mV	50.8 mV/dec	1 M KOH	J. Alloy. Compd. 2020, 825, 154073
9	Fe-doped CoSe ₂ @N-CT	330 mV	74.0 mV/dec	1 M KOH	Electrochim. Acta 2018, 265, 577-585
10	Flower like MOF derived CoSe₂	320 mV	60 mV/dec	1M KOH	This Work

Table 4.2: HER comparison table for flower-shaped MOF-D CoSe₂ with reported data.

Sl. No.	Sample	Overpotential @10mA/cm ²	Tafel slope	Electrolyte used	References
1	CoSe ₂ -160 microcubes	156 mV	40.0 mV/dec	0.5 M H ₂ SO ₄	Inorg. Chem. 2020, 59, 12778–12787
2	CoSe ₂ /C nanocrystals	260 mV	45.7 mV/dec	0.5 M H ₂ SO ₄	Int. J. Hydrogen Energy 2020, 45, 1738-1747
3	CoSe ₂ NP	250 mV	42.0 mV/dec	0.5 M H ₂ SO ₄	Electrochim. Acta. 2017, 247, 258-264.
4	Ni _{0.75} Fe _{0.25} Se ₂	197 mV	107 mV/dec	0.5 M H ₂ SO ₄	Int. J. Hydrogen Energy, 2019, 44, 22796–22805
5	CoSe ₂ nanoparticle	196 mV	39.6 mV/dec	0.5 M H ₂ SO ₄	Nanoscale, 2015, 7, 14813–14816
6	CoSe ₂ nanosheet	247 mV	52.0 mV/dec	0.5 M H ₂ SO ₄	J. Am. Chem. Soc. 2016, 138, 15, 5087–5092
7	CoSe ₂ @N/C-CNT	185 mV	98.0 mV/dec	0.5 M H ₂ SO ₄	J. Colloid Interf. Sci. 2020, 566, 296-303
8	RGO/CoSe ₂ -180	172 mV	35.2 mV/dec	0.5 M H ₂ SO ₄	Int. J. Hydrogen Energy, 2020, 45, 1738-1747
9	CoSe ₂ spheres	167 mV	38.0 mV/dec	0.5 M H ₂ SO ₄	J. Colloid Interf. Sci. 2019, 539, 646-653
10	Flower like MOF derived CoSe ₂	195 mV	43 mV/dec	0.5 M H ₂ SO ₄	This Work

4.7 Conclusions

In this work, MOF-D CoSe₂ was successfully synthesized using a Co-MOF precursor ([Co₃(tiron-bpy)₂(bpy)(H₂O)₈].(H₂O)₂) followed by a selenylation technique in a simple solvothermal method. The unique flower-like morphology corresponds to the large surface area with sufficient active sites that made the as-synthesized MOF-D CoSe₂ a superior bifunctional electrocatalyst for water electrolysis. MOF-D CoSe₂ exhibits excellent electrocatalytic behaviour with a lower overpotential of 320 mV for the OER (1 M KOH) and 195 mV for the HER (0.5 M H₂SO₄) at a predefined current density of 10 mA cm⁻². However, the lower Tafel slope values of 60 mV dec⁻¹ and 43 mV dec⁻¹ for the OER and HER respectively shows the faster surface kinetics of the electrocatalyst. The MOF derived CoSe₂ possesses a high ECSA which reflected in its better electrocatalytic behaviour. In addition, the robustness of the MOF-D CoSe₂ electrode material depicts its practical applicability under both alkaline and acidic conditions. This facile method of making MOF-D CoSe₂ opens the door to the development of a water splitting electrocatalyst that is both cost-effective and bifunctional.

4.8 References

- 1 J. O. M. Bockris, *Int. J. Hydrogen Energy*, 2002, **27**, 731–740.
- 2 M. Zeng and Y. Li, *J. Mater. Chem. A*, 2015, **3**, 14942–14962.
- 3 J. Mohammed-Ibrahim and X. Sun, *J. Energy Chem.*, 2019, **34**, 111–160.
- 4 K. T. Møller, T. R. Jensen, E. Akiba and H. Li, *Prog. Nat. Sci. Mater. Int.*, 2017, **27**, 34–40.
- 5 J. K. Das, A. K. Samantara, A. K. Nayak, D. Pradhan and J. N. Behera, *Dalton*

-
- Trans.*, 2018, **47**, 13792–13799.
- 6 N. Cheng, S. Stambula, D. Wang, M. N. Banis, J. Liu, A. Riese, B. Xiao, R. Li, T.-K. Sham, L.-M. Liu, G. A. Botton and X. Sun, *Nat. Commun.*, 2016, **7**, 13638.
- 7 Y. Lee, J. Suntivich, K. J. May, E. E. Perry and Y. Shao-Horn, *J. Phys. Chem. Lett.*, 2012, **3**, 399–404.
- 8 G. Zhao, K. Rui, S. X. Dou and W. Sun, *Adv. Funct. Mater.*, 2018, **28**, 1803291.
- 9 J. H. Han, S. Lee and J. Cheon, *Chem. Soc. Rev.*, 2013, **42**, 2581–2591.
- 10 M. Chhowalla, H. S. Shin, G. Eda, L.-J. Li, K. P. Loh and H. Zhang, *Nat. Chem.*, 2013, **5**, 263–275.
- 11 N. T. Suen, S. F. Hung, Q. Quan, N. Zhang, Y. J. Xu and H. M. Chen, *Chem. Soc. Rev.*, 2017, **46**, 337–365.
- 12 P. Jiang, Q. Liu and X. Sun, *Nanoscale*, 2014, **6**, 13440–13445.
- 13 J. Theerthagiri, G. Durai, K. Karuppasamy, P. Arunachalam, V. Elakkiya, P. Kuppusami, T. Maiyalagan and H.-S. Kim, *J. Ind. Eng. Chem.*, 2018, **67**, 12–27.
- 14 X. Zhang, X. Yu, L. Zhang, F. Zhou, Y. Liang and R. Wang, *Adv. Funct. Mater.*, 2018, **28**, 1706523.
- 15 C. Du, L. Yang, F. Yang, G. Cheng and W. Luo, *ACS Catal.*, 2017, **7**, 4131–4137.
- 16 D. Yang, L. Cao, L. Feng, J. Huang, K. Kajiyoshi, Y. Feng, Q. Liu, W. Li, L. Feng and G. Hai, *Appl. Catal. B Environ.*, 2019, **257**, 117911.
- 17 Y.-Y. Zhang, X. Zhang, Z.-Y. Wu, B.-B. Zhang, Y. Zhang, W.-J. Jiang, Y.-G. Yang, Q.-H. Kong and J.-S. Hu, *J. Mater. Chem. A*, 2019, **7**, 5195–5200.

- 18 S. Wei, R. Zhou and G. Wang, *ACS Omega*, 2019, **4**, 15780–15788.
- 19 Y. Li, H. Wang, L. Xie, Y. Liang, G. Hong and H. Dai, *J. Am. Chem. Soc.*, 2011, **133**, 7296–7299.
- 20 H. Wang, Z. Li, G. Li, F. Peng and H. Yu, *Catal. Today*, 2015, **245**, 74–78.
- 21 Z. Wu, B. Fang, A. Bonakdarpour, A. Sun, D. P. Wilkinson and D. Wang, *Appl. Catal. B Environ.*, 2012, **125**, 59–66.
- 22 Y. Guo, C. Shang and E. Wang, *J. Mater. Chem. A*, 2017, **5**, 2504–2507.
- 23 J. Du, Z. Zou, C. Liu and C. Xu, *Nanoscale*, 2018, **10**, 5163–5170.
- 24 F. Ming, H. Liang, Y. Lei, W. Zhang and H. N. Alshareef, *Nano Energy*, 2018, **53**, 11–16.
- 25 M. Huynh, D. K. Bediako and D. G. Nocera, *J. Am. Chem. Soc.*, 2014, **136**, 6002–6010.
- 26 V. D. Silva, T. A. Simões, J. P. F. Grilo, E. S. Medeiros and D. A. Macedo, *J. Mater. Sci.*, 2020, **55**, 6648–6659.
- 27 Y. Gao, S. Chen, D. Cao, G. Wang and J. Yin, *J. Power Sources*, 2010, **195**, 1757–1760.
- 28 R. Zhang, Y.-C. Zhang, L. Pan, G.-Q. Shen, N. Mahmood, Y.-H. Ma, Y. Shi, W. Jia, L. Wang, X. Zhang, W. Xu and J.-J. Zou, *ACS Catal.*, 2018, **8**, 3803–3811.
- 29 G. Wang, L. Zhang and J. Zhang, *Chem. Soc. Rev.*, 2012, **41**, 797–828.
- 30 S. Anantharaj, S. R. Ede, K. Sakthikumar, K. Karthick, S. Mishra and S. Kundu, *ACS Catal.*, 2016, **6**, 8069–8097.
- 31 X. Huang, Z. Zeng and H. Zhang, *Chem. Soc. Rev.*, 2013, **42**, 1934.

- 32 M.-R. Gao, Y.-F. Xu, J. Jiang and S.-H. Yu, *Chem. Soc. Rev.*, 2013, **42**, 2986.
- 33 A. Zhao, G. Xu, Y. Li, J. Jiang, C. Wang, X. Zhang, S. Zhang and L. Zhang, *Inorg. Chem.*, 2020, **59**, 12778–12787.
- 34 H. Ding, G. Xu, L. Zhang, B. Wei, J. Hei and L. Chen, *J. Colloid Interface Sci.*, 2020, **566**, 296–303.
- 35 J. Wang, X. Yue, Y. Yang, S. Sirisomboonchai, P. Wang, X. Ma, A. Abudula and G. Guan, *J. Alloys Compd.*, 2020, **819**, 153346.
- 36 N. Xue, Z. Lin, P. Li, P. Diao and Q. Zhang, *ACS Appl. Mater. Interfaces*, 2020, **12**, 28288–28297.
- 37 Q. Dong, Q. Wang, Z. Dai, H. Qiu and X. Dong, *ACS Appl. Mater. Interfaces*, 2016, **8**, 26902–26907.
- 38 H. Lu, Y. Zhang, Y. Huang, C. Zhang and T. Liu, *ACS Appl. Mater. Interfaces*, 2019, **11**, 3372–3381.
- 39 S. L. James, *Chem. Soc. Rev.*, 2003, **32**, 276.
- 40 T. Chen, S. Li, J. Wen, P. Gui and G. Fang, *ACS Appl. Mater. Interfaces*, 2017, **9**, 35927–35935.
- 41 R. R. Salunkhe, Y. V. Kaneti and Y. Yamauchi, *ACS Nano*, 2017, **11**, 5293–5308.
- 42 M. Eddaoudi, J. Kim, N. Rosi, D. Vodak, J. Wachter, M. O’Keeffe and O. M. Yaghi, *Science*, 2002, **295**, 469–472.
- 43 M. K. Sahoo, A. K. Samantara and J. N. Behera, *Inorg. Chem.*, 2020, **59**, 12252–12262.

- 44 X. Liu, Y. Liu and L. Z. Fan, *J. Mater. Chem. A*, 2017, **5**, 15310–15314.
- 45 C.-P. Lee, W.-F. Chen, T. Billo, Y.-G. Lin, F.-Y. Fu, S. Samireddi, C.-H. Lee, J.-S. Hwang, K.-H. Chen and L.-C. Chen, *J. Mater. Chem. A*, 2016, **4**, 4553–4561.
- 46 R. K. Tiwari, I. Shruti and J. N. Behera, *RSC Adv.*, 2021, **11**, 10767–10776.
- 47 R. K. Tripathy, A. K. Samantara and J. N. Behera, *Dalton Trans.*, 2019, **48**, 10557–10564.
- 48 S. Anantharaj, P. N. Reddy and S. Kundu, *Inorg. Chem.*, 2017, **56**, 1742–1756.
- 49 X. Li, X. Hao, A. Abudula and G. Guan, *J. Mater. Chem. A*, 2016, **4**, 11973–12000.
- 50 D. Kong, H. Wang, Z. Lu and Y. Cui, *J. Am. Chem. Soc.*, 2014, **136**, 4897–4900.
- 51 Y. Liu, H. Cheng, M. Lyu, S. Fan, Q. Liu, W. Zhang, Y. Zhi, C. Wang, C. Xiao, S. Wei, B. Ye and Y. Xie, *J. Am. Chem. Soc.*, 2014, **136**, 15670–15675.
- 52 S.-K. Park, J. K. Kim and Y. Chan Kang, *J. Mater. Chem. A*, 2017, **5**, 18823–18830.
- 53 T. Chen, S. Li, P. Gui, J. Wen, X. Fu and G. Fang, *Nanotechnology*, 2018, **29**, 205401.
- 54 L. Quan, T. Liu, M. Yi, Q. Chen, D. Cai and H. Zhan, *Electrochim. Acta*, 2018, **281**, 109–116.
- 55 Y. Deng, C. Ye, G. Chen, B. Tao, H. Luo and N. Li, *J. Energy Chem.*, 2019, **28**, 95–100.
- 56 S.-K. Park, J. K. Kim and Y. C. Kang, *Chem. Eng. J.*, 2017, **328**, 546–555.

- 57 J. Guo, J. Wang, Z. Wu, W. Lei, J. Zhu, K. Xia and D. Wang, *J. Mater. Chem. A*, 2017, **5**, 4879–4885.
- 58 S. Jung, C. C. L. McCrory, I. M. Ferrer, J. C. Peters and T. F. Jaramillo, *J. Mater. Chem. A*, 2016, **4**, 3068–3076.
- 59 G. Li, L. Anderson, Y. Chen, M. Pan and P.-Y. Abel Chuang, *Sustain. Energy Fuels*, 2018, **2**, 237–251.
- 60 F. Song and X. Hu, *Nat. Commun.*, 2014, **5**, 4477.
- 61 X. Wang, F. Li, W. Li, W. Gao, Y. Tang and R. Li, *J. Mater. Chem. A*, 2017, **5**, 17982–17989.
- 62 L. Fang, W. Li, Y. Guan, Y. Feng, H. Zhang, S. Wang and Y. Wang, *Adv. Funct. Mater.*, 2017, **27**, 1701008.
- 63 Y. Zhou, H. Xiao, S. Zhang, Y. Li, S. Wang, Z. Wang, C. An and J. Zhang, *Electrochim. Acta*, 2017, **241**, 106–115.
- 64 W.-F. Chen, S. Iyer, S. Iyer, K. Sasaki, C.-H. Wang, Y. Zhu, J. T. Muckerman and E. Fujita, *Energy Environ. Sci.*, 2013, **6**, 1818.
- 65 P. Xiao, M. A. Sk, L. Thia, X. Ge, R. J. Lim, J.-Y. Wang, K. H. Lim and X. Wang, *Energy Environ. Sci.*, 2014, **7**, 2624–2629.

CHAPTER – 5

NiSe₂ nanoparticles encapsulated in N-doped carbon matrix derived from a one-dimensional Ni-MOF: an efficient and sustained electrocatalyst for hydrogen evolution reaction

5.1 Abstract

5.2 Introduction

5.3 Experimental section

5.3.1 Materials

5.3.2 Synthesis of 1D Ni-MOF

5.3.3 Synthesis of Ni nanoparticles (Ni-T@NC)

5.3.4 Synthesis of NiSe₂ nanoparticles (NiSe₂-T@NC)

5.4 Characterization

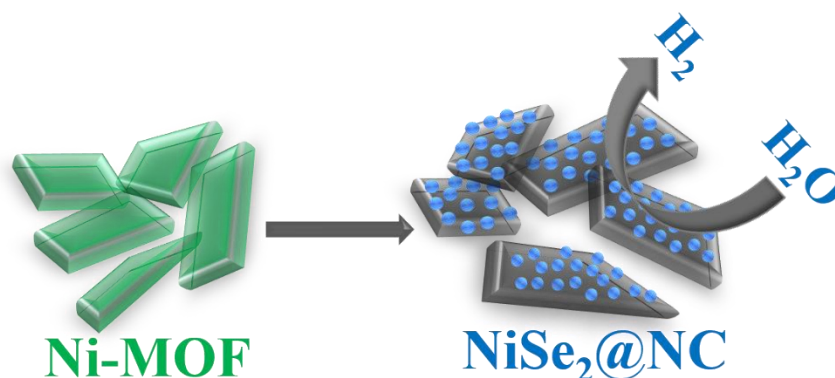
5.5 Electrochemical measurements

5.6 Results and discussion

5.7 Conclusions

5.8 References

5.1 Abstract



The spherical-type NiSe₂ nanoparticles encapsulated in a N-doped carbon (NC) matrix (NiSe₂-T@NC, temperature (T) = 400–800 °C) are derived from a 1D Ni-MOF precursor of the formula [Ni(BPY)(DDE)] [(BPY = 2,2'-bipyridyl), (DDE = 4,4'-dicarboxy diphenyl ether)] via a facile solvothermal technique followed by annealing at different temperatures and selenylation strategies. The combined effect of a NC matrix and the Ni nanoparticles has been optimized during varied annealing processes with subsequent selenylation, leading to the formation of the series NiSe₂-400@NC, NiSe₂-500@NC, NiSe₂-600@NC, NiSe₂-700@NC, and NiSe₂-800@NC, respectively. The variation of annealing temperature plays a vital role in optimizing the catalytic behavior of the NiSe₂-T@NCs. Among different high-temperature annealed products, NiSe₂-600@NC shows superior electrocatalytic performance because of the unique spherical-type morphology and higher specific surface area (57.95 m² g⁻¹) that provides a large number of electrochemical active sites. The synthesized material exhibits a lower overpotential of 196 mV to deliver 10 mA cm⁻² current density, a small Tafel slope of 45 mV dec⁻¹ for better surface kinetics, and outstanding durability in an acidic solution, respectively. Consequently, the post stability study of the used electrocatalyst gives insight into surface phase analysis. Therefore, we presume that the synthesized

1D MOF precursor derived NiSe₂ nanoparticles encapsulated in a NC matrix has excellent potential to replace the noble-metal-based electrocatalyst for enhanced hydrogen evolution through simple water electrolysis.

5.2 Introduction

Hydrogen energy has been considered a surrogate high-energy density fuel source compared to traditional fossil fuels (such as natural gas, coal, and oils) because of its recyclability and ecofriendly nature.¹⁻³ The production of hydrogen (>95%) is firmly dependent on coal gasification and steam forming. However, these belong to traditional fossil fuels, which generate an enormous amount of carbon as a byproduct.^{4,5} Electrochemical water splitting is the cleanest and sustainable method for high-purity expansive hydrogen production. The cathodic hydrogen evolution reaction (HER) and anodic oxygen evolution reaction (OER) are the durable process in the water electrolysis for the evolution of molecular hydrogen (H₂) and oxygen (O₂), corresponding to naught carbon emission.⁶⁻¹⁰ Besides these, the electrolysis process is a surface phenomenon and involves some energy barriers. The additional energy required to overcome the energy barrier associated with the hydrogen bond in a water molecule is known as overpotential.^{11,12} Mainly, the precious platinum-based electrocatalyst are most HER efficient to actuate proton reduction with lower overpotential value. However, its poor durability and expensive nature restrict its use on an industrial scale.¹³⁻¹⁶ To overcome these restrictions and develop a cost-effective, efficient, and earth-abundant HER electrocatalyst is highly challenging. Consequently, a spacious range of transition metal based HER electrocatalyst has been considered the most efficient and alternative nonprecious electrocatalyst compared to platinum-based precious ones.¹² In particular, for water splitting reactions, transition metal based

electrocatalysts such as metal chalcogenides (both sulfides and selenides),^{17–21} metal oxides,^{22–25} metal phosphides,^{26–30} metal carbides,^{31,32} and metal nitrides^{33,34} have drawn great attention because of their low cost, metallic nature, large surface area, and narrow band gap, corresponding to good electrocatalytic performances.^{35,36} However, the easy restacking due to the absence of any carbon-containing matrix and poor conductivity still does not give satisfactory results to compete with the electrocatalytic performances of precious ones.^{37,38}

Therefore, the researchers have driven their research toward metal-organic frameworks (MOFs). The use of MOFs as a precursor benefits a carbon-containing network without further addition of carbonaceous material. The carbon matrix obtained from the organic framework can act as a highly conductive network, promoting fast electron transfer.³⁹ The various heteroatoms (such as N, O, S, and P) contained in the organic ligands can be directly doped into the carbon framework, which provides more active sites and creates a favorable environment for the growth of metal nanoparticles.^{40–45} In particular, a 1D MOF precursor have uniform and monodisperse morphology, and their derived carbonaceous materials can afford a high surface area that corresponds to better electrocatalytic performances.⁴⁶ Furthermore, selenylation of the MOFs precursor by following various synthetic routes (such as chemical vapor deposition (CVD), solvothermal technique) are widely accepted to synthesize a highly efficient MOFs precursor-derived N-doped carbon (NC)-embedded metal selenides electrocatalyst for the electrochemical HER.^{3,47,48} The good electrical conductivity and large surface area of the MOF precursor-derived NC-embedded metal selenides, implying more catalytic active sites and better durability under harsh acidic conditions, dominates over non-MOF-derived pristine transition metal based electrocatalysts for water electrolysis to generate carbon-free energy carriers.^{37,49} Particularly, the highly active HER

electrocatalyst is more favorable in the acidic electrolytic medium.⁴⁸ In contrast to the 3d transition metal series, nickel-based selenides display better HER activity than other transition metal dichalcogenides (TMDCs) due to their intrinsic conductivity. However, the poor corrosion resistance, easy aggregation in bulk phase, and instability issue in strongly acidic conditions still urge the development of a new synthetic method with controlled morphological structures, increasing the number of active sites to enhance HER activity of NiSe₂ based electrocatalyst.^{48,50} Therefore, various Ni-based MOFs precursor selenylation techniques are employed to explore HER efficient NiSe₂. Ma et al. designed a 3D MoSe₂/NiSe₂ composite nanowires on carbon fiber paper following a two-step hydrothermal approach. It required only 193 mV overpotential to reach a current density of 10 mA cm⁻², and a Tafel slope of 46.9 mV dec⁻¹ in an electrolytic medium of 0.5 M H₂SO₄.⁵¹ Nowadays, free-standing HER electrocatalysts without having any substrate have gathered much attention. In view to preparing free-standing HER catalyst, Yang et al. synthesized MoS₂-NiSe nanohybrids with vertical heterostructure interfaces. The MoS₂-NiSe nanohybrids need an overpotential of 210 mV to deliver the current density of 10 mA cm⁻² with a lower Tafel value of 56 mV dec⁻¹ in an acidic medium.⁵² Besides these, some groups focus on MOFs-precursor-derived NC-embedded nickel selenides. Sun group fabricated an MOF-derived NiSe@NC nanohybrid through the selenylation process and showed excellent HER performances at different pH values.³⁷ Similarly, Chen et al. synthesized N-doped graphene encapsulated NiSe₂ derived from a Ni-based MOF precursor, corresponding to good HER activity in acidic and alkaline media.⁴⁸ Thus, improving the efficacy of the material to act as a suitable electrocatalyst is important. Investigating an efficient

nickel-based selenide electrocatalyst encapsulated in an NC matrix from a Ni-MOF precursor with divergent ligands and the metal ion is still challenging.

Herein, we have successfully synthesized a 1D Ni-MOF precursor [Ni(BPY)(DDE)], through a facile solvothermal process by using 2,2'-bipyridyl and 4,4'-dicarboxy diphenyl ether as the ligands. The pyrolysis treatment under an inert atmosphere increases the specific surface area and exposes the active sites due to the carbonization of the Ni-MOF precursor. Therefore, by varying different annealing temperatures ($T = 400\text{--}800\text{ }^{\circ}\text{C}$), we synthesized an intermediate product of NC-embedded nickel nanoparticles (Ni-T@NCs). Furthermore, subsequent pyrolysis with selenium powder gives rise to a free-standing NiSe₂ embedded in an NC matrix (named NiSe₂-T@ NC; $T = 400\text{--}800\text{ }^{\circ}\text{C}$). The Ni-MOF with nitrogen atoms in its ligand, which acts as a suitable sacrificial template for synthesizing an NC-encapsulated nickel selenide hybrid material.⁵³ The synergistic effect of the inner NiSe₂ nanoparticles and the outer NC layer enhances the conductivity and long-term durability of the as-synthesized electrocatalyst leading to better electrochemical performance in acidic conditions. Out of these various annealing products, NiSe₂-600@NC shows better HER performance among all the NiSe₂- T@NCs. The controlled spherical-type morphological structure of NiSe₂-600@NC results in a higher catalytic active surface area, corresponding to a lower overpotential of 196 mV required to reach the current density of 10 mA cm^{-2} . Additionally, the surface kinetics (in terms of Tafel slope) of 45 mV dec^{-1} reveals the actual HER mechanism process. The obtained value is lower than the other as-synthesized annealed products and displays excellent surface kinetics. Moreover, NiSe₂-600@NC exhibits 24 h of long-term stability with negligible change in potential in the acidic medium. However, these above superior HER results of NiSe₂-600@NC

are attributed to higher specific surface area ($57.95 \text{ m}^2 \text{ g}^{-1}$) and controlled spherical-type morphology, correlated to higher electrochemical active surface sites.

5.3 Experimental section

5.3.1 Materials

Analytical-grade chemicals were received and used without further processing. Nickel nitrate hexahydrate; $\text{Ni}(\text{NO}_3)_2 \cdot 6\text{H}_2\text{O}$, 2,2'-bipyridyl (BPY), 4,4'-dicarboxy diphenyl ether (DDE), N,N'-dimethylformamide (DMF), selenium powder, and Nafion solution were purchased from Sigma-Aldrich, TCI, and Himedia Chemicals. The preparation of the electrolyte solutions and washing of the synthesized materials were done with deionized water.

5.3.2 Synthesis of 1D Ni-MOF, [Ni(BPY)(DDE)]

A 1D Ni-MOF precursor was synthesized by taking 2,2'-bipyridyl and 4,4'-dicarboxy diphenyl ether as the ligands in an improved solvothermal synthesis method.⁵⁴ First, 0.129 g of 4,4'-dicarboxy diphenyl ether and 0.078 g of 2,2'-bipyridyl were added into 12 mL of DMF, and stirring was continued for 15 min. After that, 0.145 g of $\text{Ni}(\text{NO}_3)_2 \cdot 6\text{H}_2\text{O}$ was dissolved in the mixture precursor and left to be stirred for 1 h. The resultant green color solution was transferred into a 23 mL Teflon-lined autoclave and heated in a hot air oven at $140 \text{ }^\circ\text{C}$ for 72 h. After cooling to room temperature, green plate-shaped crystals were collected by filtration following centrifugation. The crystals were washed with ethanol.

5.3.3 Synthesis of Ni nanoparticles (Ni-T@NC)

The as-prepared Ni-MOF was taken in a porcelain alumina boat and annealed at different temperatures ($T = 400\text{--}800 \text{ }^\circ\text{C}$) in an argon atmosphere for 2 h to get Ni

nanoparticles embedded in NC layers, denoted as Ni-T@NC where T represents the varied annealing temperature.

5.3.4 Synthesis of NiSe₂ nanoparticles (NiSe₂-T@NC)

In a typical method, the obtained Ni-T@NC and selenium powder were mixed (in 1:2 mass ratio) homogeneously using mortar and pestle and then transferred into a porcelain boat. The porcelain boat containing the homogeneous mixture was placed inside an MTI tube furnace and heated at 300 °C for 3 h in an argon atmosphere to get NiSe₂-T@NC (T = 400–800 °C).

5.4 Characterization

The crystal lattice system and the phase purity of samples have been identified using the Bruker D8 Advance diffractometer system (XRD) with Cu K α radiation of wavelength ($\lambda = 1.5418 \text{ \AA}$). A Raman microscope (Horiba Scientific) with laser excitation at a wavelength of 532 nm was used to verify the graphitic phase of the materials. The surface morphological architecture has been characterized by field-emission scanning electron microscopy (FESEM, Zeiss Pvt. Ltd., Germany) and transmission electron microscopy (TEM, equipped with HRTEM, JEOL 2100F, at 200 kV). Moreover, the chemical state and elemental composition were verified with the high-resolution X-ray photoelectron spectroscopy (XPS, PHI Versa Probe III). Furthermore, the surface area of the as-synthesized samples was determined by the Brunauer-Emmett-Teller (BET) analysis via Quantachrome Autosorb instrument.

5.5 Electrochemical measurements

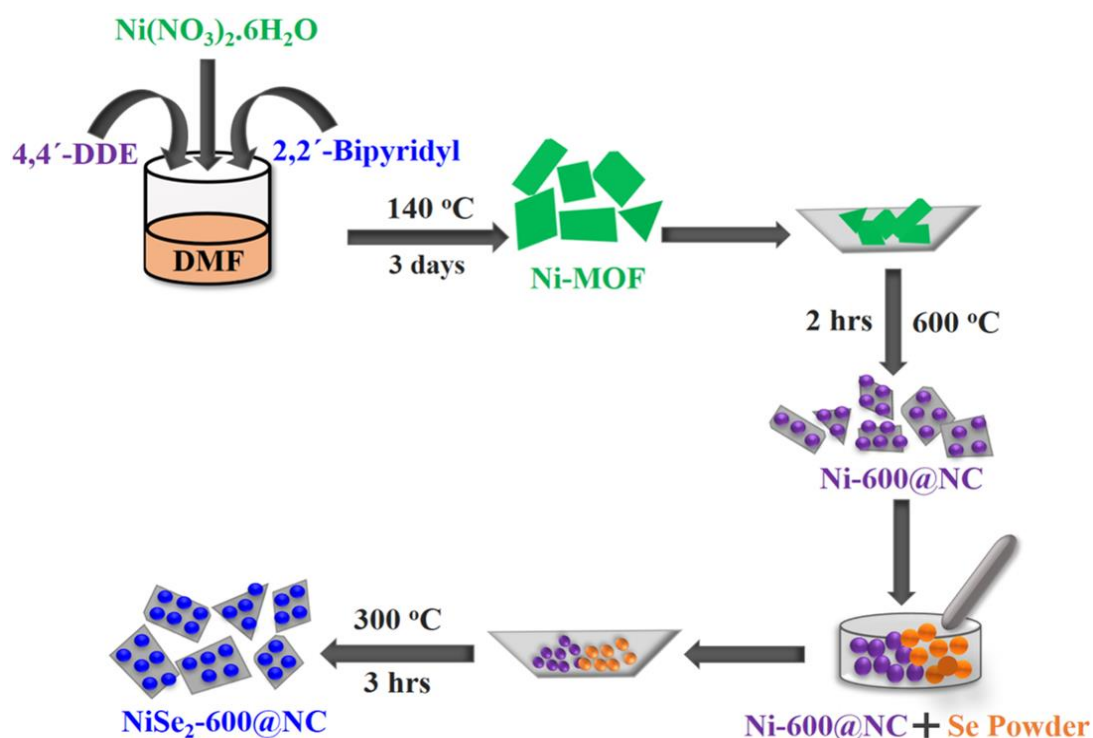
The HER performances have been carried out in a three-electrode measurement setup (Autolab PGSTAT100N) in 0.5 M H₂SO₄ as a supporting electrolyte. The sample

modified glassy carbon electrode (GCE: mass loading 0.25 mg cm⁻²) acts as a working electrode. The aqueous Ag/AgCl and a graphite rod are the reference and auxiliary electrodes, respectively. Linear sweep voltammograms (LSVs) for all samples were carried out at a sweep rate of 5 mV s⁻¹. The obtained current density from the LSV curves has been normalized to the geometrical surface area of the used electrode. All the measured potential (vs. Ag/AgCl) were *iR* corrected and calibrated to reversible hydrogen electrode (RHE) scale as per the Nernst equation: $E_{\text{RHE}} = E_{\text{Ag/AgCl}} + 0.0591(\text{pH}) + 0.21 \text{ V}$. The Tafel slope values were determined by plotting overpotential versus logarithm of obtained current density via fitting the linear region of the Tafel plot. The equation used for calculation is as follows: $\eta = a + b \log J$ (where η is the overpotential and a , b , and J are the Tafel constant, Tafel slope, and current density, respectively). Electrochemical impedance spectroscopy (EIS) was carried out at a potentiostatic mode of -0.19 V (vs. RHE) under an AC amplitude of 5 mV within a frequency scale of 1 MHz to 0.1 Hz in 0.5 M H₂SO₄. In order to verify the electrochemical double-layer capacitance (C_{dl}) of the catalyst, a cyclic voltammetry technique has been used in a non-Faradaic region of 0.11–0.31 V (vs. RHE) at various scan rates (20–200 mV s⁻¹). The electrochemical active surface area (ECSA) is linearly correlated with the C_{dl} value of the synthesized electrocatalyst. The long-term durability test of the as-synthesized electrocatalyst was carried out by a chronopotentiometry (CP) technique.

5.6 Results and discussion

The NC-embedded NiSe₂ has been derived from a 1D Ni-MOF precursor [Ni(BPY)(DDE)] [(BPY = 2,2'-bipyridyl), (DDE = 4,4'-dicarboxy diphenyl ether)]. The stepwise synthesis procedure of 1D Ni-MOF precursor and procured temperature

5.1. The overall reaction step includes a facile solvothermal method followed by high-temperature annealing and subsequent selenylation.



Scheme 5.1: Reaction scheme for the stepwise synthesis of NiSe₂-600@NC.

First, the Ni-MOF precursor has been synthesized by taking $\text{Ni}(\text{NO}_3)_2 \cdot 6\text{H}_2\text{O}$, 2,2'-bipyridyl, and 4,4'-dicarboxy diphenyl ether in DMF solution at 140 °C for 72 h in a solvothermal approach. **Figures 5.1a-d** represents the crystal structures of the Ni-MOF. The phase purity of the as-obtained Ni-MOF was examined by PXRD analysis. The simulated data matches well with the experimental data indicating the successful synthesis of the Ni-MOF as shown in **Figure 5.1e**.

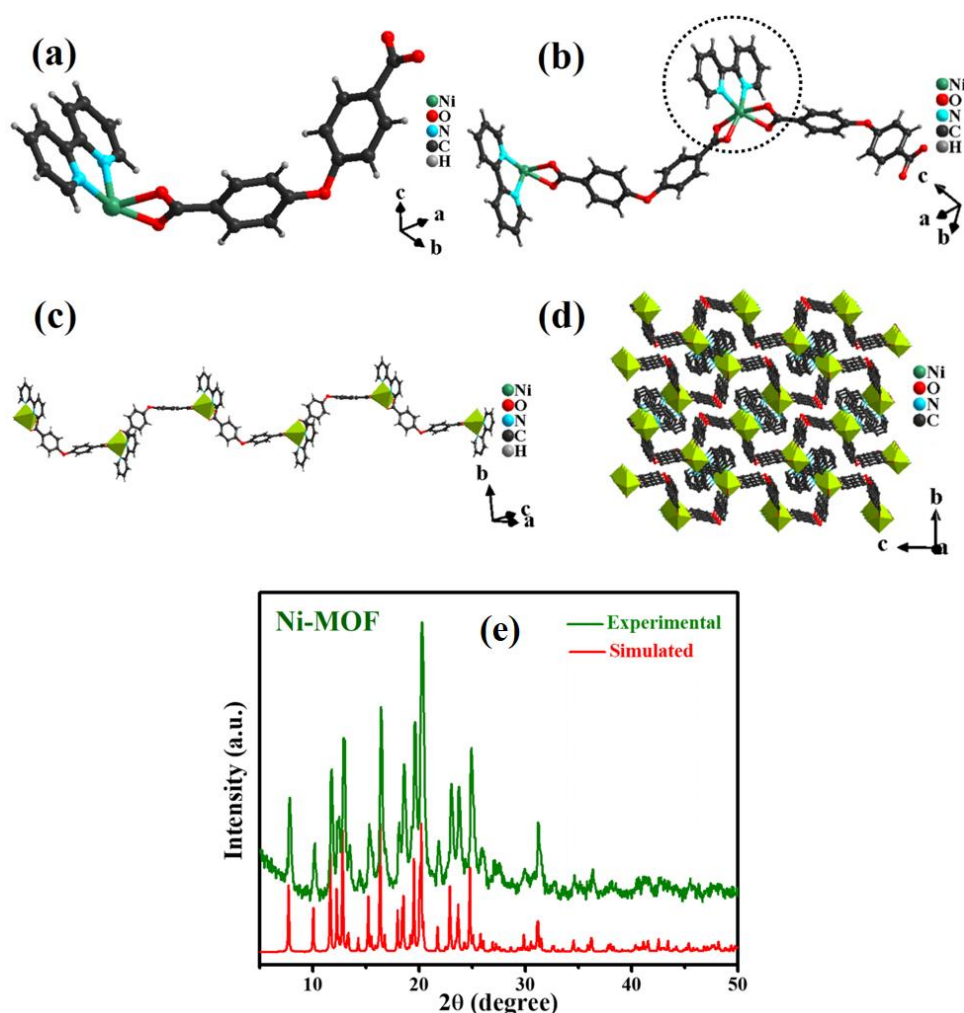


Figure 5.1: Asymmetric unit of Ni-MOF (a), growing 1D chain structure of Ni-MOF (b and c), 3D packed structure of Ni-MOF (d), PXRD of Ni-MOF (e).

Furthermore, the high-temperature annealing process of the Ni-MOF was carried out to convert it to the NC layer encapsulated nickel nanoparticles (represented as Ni-600@NC). The formation of Ni-600@NC is due to the reduction of Ni-MOF cation into nickel nanoparticles and the organic ligand moiety into NC layers. Additionally, the grinding of Ni-600@NC with selenium powder was done to obtain a homogeneous mixture, followed by high-temperature selenylation at 300 °C for 3 h to get the optimized NiSe₂-600@NC as HER efficient electrocatalyst as compared to other annealed products. After successfully synthesizing Ni-600@NC and NiSe₂-600@NC

starting from a Ni-MOF precursor, the phase purity was verified by using powder X-ray diffraction (PXRD). The crystallinity of Ni-600@NC depicts the diffraction peaks at 44.6, 52.2, and 76.6° can be assigned to the (111), (200), and (220) planes of the Ni nanoparticles (Powder Diffraction File (PDF) no. 01-070-0989, Joint Committee on Powder Diffraction Standards (JCPDS)) as shown in **Figure 5.2a**.⁴⁸ **Figure 5.2b** shows the diffraction line at 2θ of 30.1, 33.6, 36.9, 42.9, 50.8, 55.6, 57.9, and 62.3° correspond to the (200), (210), (211), (220), (311), (230), (321), and (400) planes of the cubic NiSe₂-600@NC (PDF no. 00-011-0552, JCPDS), indicating the high crystallinity of the as-synthesized NiSe₂ obtained from the selenylation of Ni-600@NC. The presence of carbon content in the as-synthesized Ni-600@NC and NiSe₂-600@NC were verified by Raman analysis, as shown in **Figures 5.3a and b**. The D and G bands correspond to the disorderliness and graphitic nature of the samples indicating the presence of carbon composite.¹⁰ In **Figure 5.3a**, two Raman peaks around 1329 and 1589 cm⁻¹ correspond to the D and G bands of Ni-600@NC, whereas the characteristic D and G bands appear around 1323 and 1581 cm⁻¹ for NiSe₂-600@NC as presented in **Figure 5.3b**. The *I_D*/*I_G* intensity ratio is about 1.23 of Ni-600@NC, compared to 1.87 of NiSe₂-600@NC, which shows the increase in intensity ratio indicating the availability of significant structural defects.^{10,55,56}

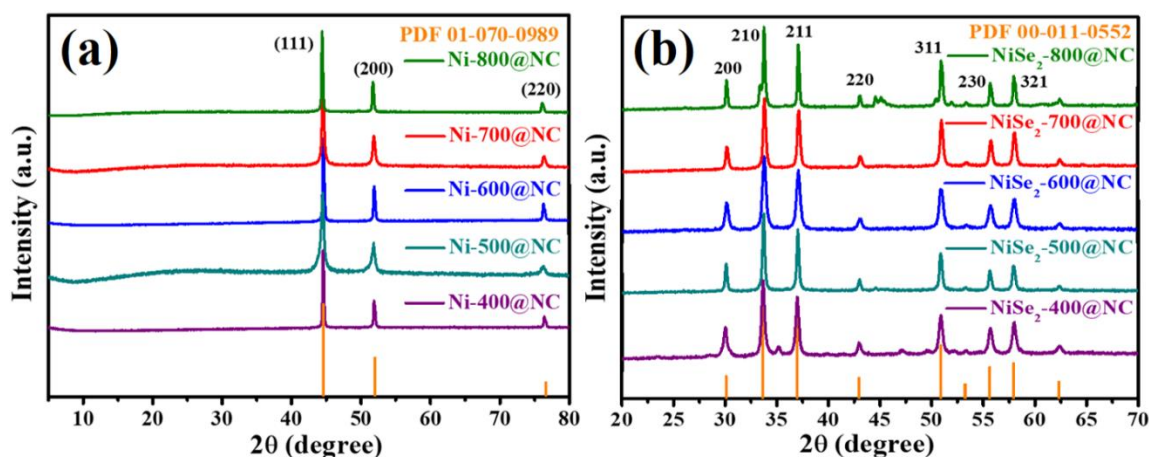


Figure 5.2: PXRD data of Ni-T@NCs (a), and NiSe₂-T@NCs (b).

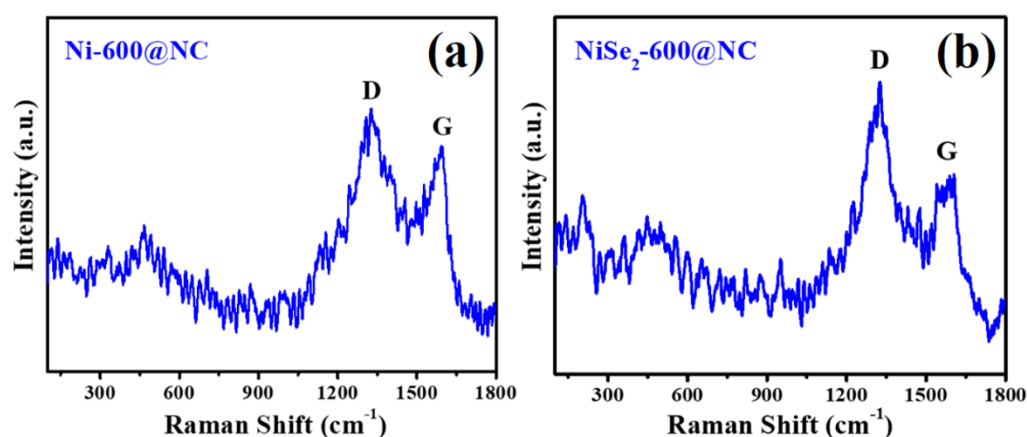


Figure 5.3: Raman spectra of Ni-600@NC (a), and NiSe₂-600@NC (b).

The scanning electron microscopy (SEM) and transmission electron microscopy (TEM) analysis were carried out for the morphological characterization of the materials. **Figures 5.4a and b** shows the aggregated thick plate-like morphology of the 1D Ni-MOF at different magnifications before the high-temperature annealing process. After the high-temperature annealing, the thick plate-like morphology of Ni-MOF precursor was carbonized and converted into Ni nanoparticles having spherical morphology distributed uniformly over the porous plate structures as illustrated in **Figures 5.4c and d**. Furthermore, selenylation of Ni-600@NC arouse more porous plate with spherical NiSe₂ nanoparticles, as shown in **Figures 5.4e and f**. Besides these, the SEM images of the other high-temperatures annealed products (such as NiSe₂-T@NCs, T = 400, 500, 700, and 800 °C) are shown in **Figure 5.5**. However, the variation of temperatures from lower to higher of the annealing process gives rise to quasi-spherical type morphology to diminished aggregated spherical-type morphology of as-prepared samples. Likewise, SEM analysis, the in-depth morphological analysis of the NiSe₂-600@NC, was carried out by high-resolution TEM analysis. The TEM images of NiSe₂-600@NC at different magnifications of 1 μm and 100 nm confirms that these spherical-type NiSe₂ nanostructures are embraced with NC layers (**Figures 5.6a and b**). The HRTEM

pictures indicate the interplanar d-spacing value of 0.24 nm, corresponding to the (211) crystal plane of NiSe₂ phases as shown in **Figures 5.6c and d**. The inset in **Figure 5.6c** shows the selected-area electron diffraction (SAED) pattern of the NiSe₂-600@NC, representing the high crystallinity of the sample.

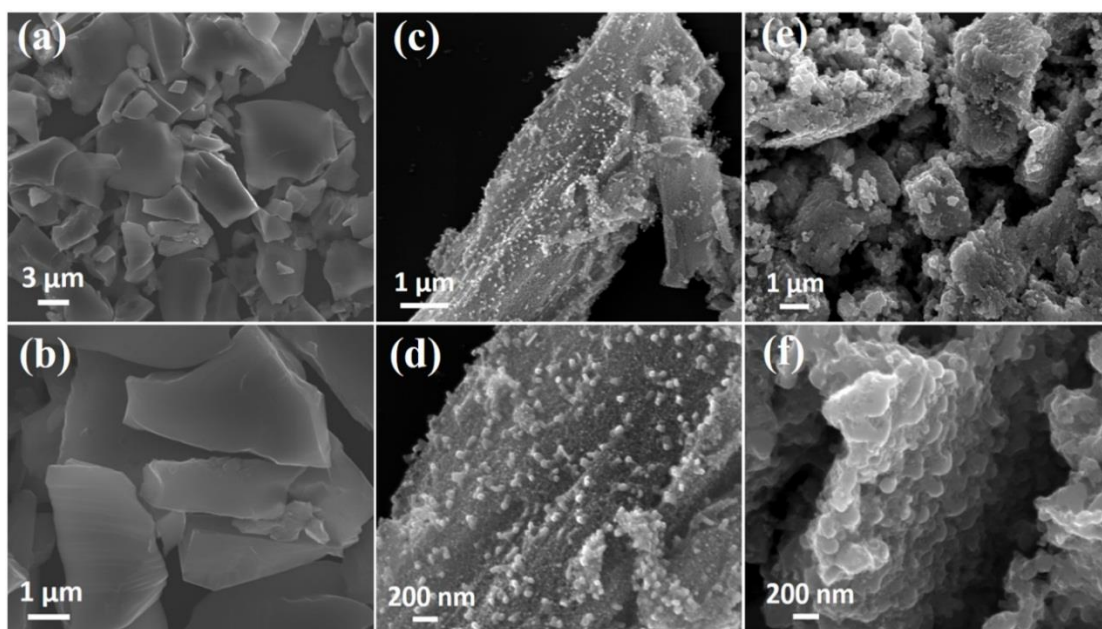


Figure 5.4: SEM images of Ni-MOF (a, b), Ni-600@NC (c, d), NiSe₂-600@NC (e, f).

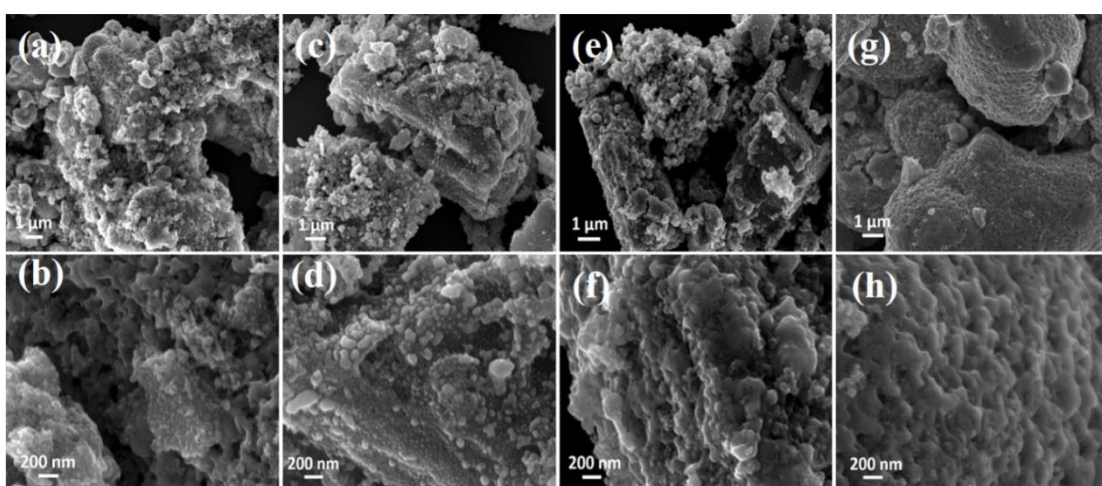


Figure 5.5: SEM images of NiSe₂-400@NC (a, b), NiSe₂-500@NC (c, d), NiSe₂-700@NC (e, f), NiSe₂-800@NC (g, h).

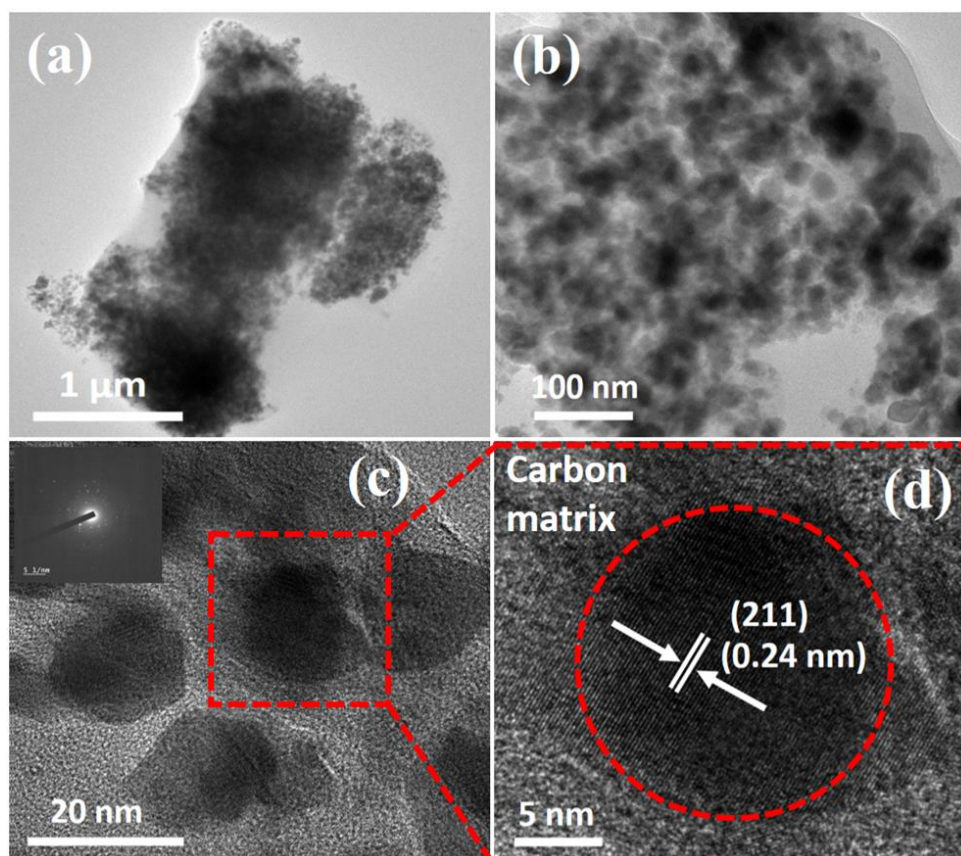


Figure 5.6: TEM pictures of NiSe₂-600@NC at different magnifications (a, b). High-resolution TEM images of NiSe₂-600@NC (c, d); the inset in (c) is the selected-area electron diffraction (SAED) pattern.

The elemental composition and chemical state of NiSe₂-600@NC was carried out with the help of X-ray photoelectron spectroscopy (XPS). **Figure 5.7a** shows the full scan XPS survey of NiSe₂-600@NC, which exhibits the presence of Se, C, N, O, and Ni. The presence of oxygen owing to the unavoidable oxygen species or surface oxidation of NiSe₂-600@NC sample on exposure to air.^{53,57} The XPS spectra of Ni 2p_{3/2} and Ni 2p_{1/2} are presented in **Figure 5.7b**. The positions of the peaks are at the observed binding energies of 853.4 and 870.8 eV, which are the characteristics peaks of Ni²⁺ ions. However, the peaks located at 855.5 and 873.4 eV are attributed to the presence of Ni³⁺ ions because of the surface oxidized phase. In addition, the peaks at the binding energies of 860.2 and 878.9 eV assigned to the satellite peaks of Ni 2p_{3/2} and Ni 2p_{1/2}.^{3,48,51,58,59}

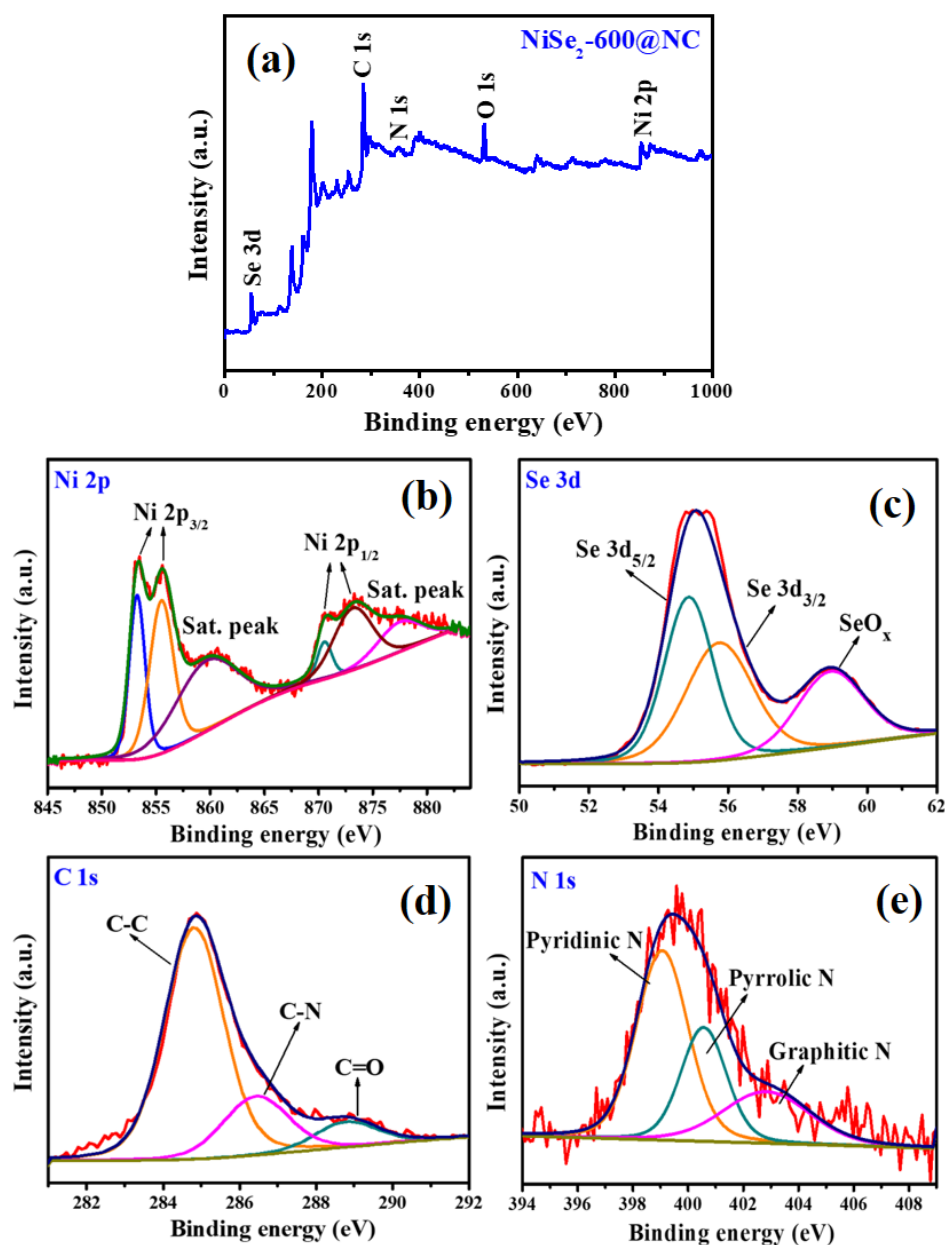


Figure 5.7: Full scan XPS spectra of NiSe₂-600@NC (a), deconvoluted XPS spectra of Ni 2p (b), Se 3d (c), C 1s (d), N 1s (e).

Figure 5.7c represents the existence of Se 3d, where the prominent peak positions at the binding energies of 55.6 and 54.8 eV are indexed to Se 3d_{5/2} and Se 3d_{3/2} of Ni–Se bonds. Furthermore, the peak at 59.1 eV shows the presence of surface oxidation of Se atoms.^{9,48,56} The high-resolution C 1s peak (**Figure 5.7d**) is deconvoluted into three peaks centered at 284.6, 285.8, and 288.8 eV, which can be assigned to the C–C, C–N,

and C=O bonds, respectively.^{48,60–62} Deconvolution of N 1s is fitted into three peaks centered around 398.8, 400.2, and 402.6 eV, corresponding to pyridinic N, pyrrolic N, and graphitic N, respectively (**Figure 5.7e**).^{3,55,60} The Brunauer-Emmett-Teller (BET) analysis has been used to verify the specific surface area of the Ni-MOF precursor and different high-temperature pyrolyzed NiSe₂-T@NC products. In **Figure 5.8**, compared to Ni-MOF precursor and other high-temperature-annealed NiSe₂-T@NCs (T = 400–800 °C), NiSe₂-600@NC has the highest specific surface area of 57.95 m² g⁻¹. It has been observed that the annealing temperature (at 600 °C) of the Ni-MOF precursor plays a crucial role in optimizing the surface area and porous nature corresponding to better electrocatalytic performance of NiSe₂-600@NC toward an enhanced HER.

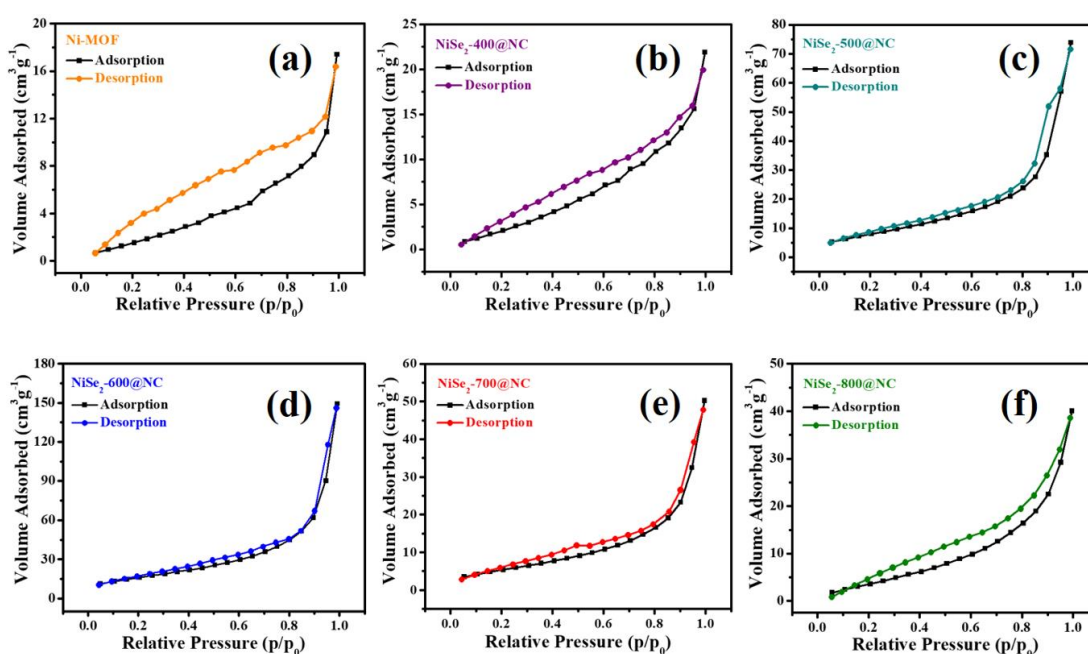


Figure 5.8: BET surface area analysis of Ni-MOF (a) and NiSe₂-T@NCs (b-f).

The effect of varying high-temperature annealing of Ni-MOF precursor with subsequent selenylation to form NiSe₂-T@NC products for electrochemical HER have been carried out in a three-electrode measurement setup using nitrogen saturated 0.5 M

Chapter 5 *NiSe₂ nanoparticles encapsulated in N-doped carbon matrix derived from a one-dimensional Ni-MOF: an efficient and sustained electrocatalyst for hydrogen evolution reaction*
 H₂SO₄ as the supporting electrolyte. All the linear sweep voltammetry (LSVs) data have been recorded at a sweep rate of 5 mV s⁻¹ and are *iR*-corrected on a reversible hydrogen electrode (RHE) scale (**Figure 5.9**).

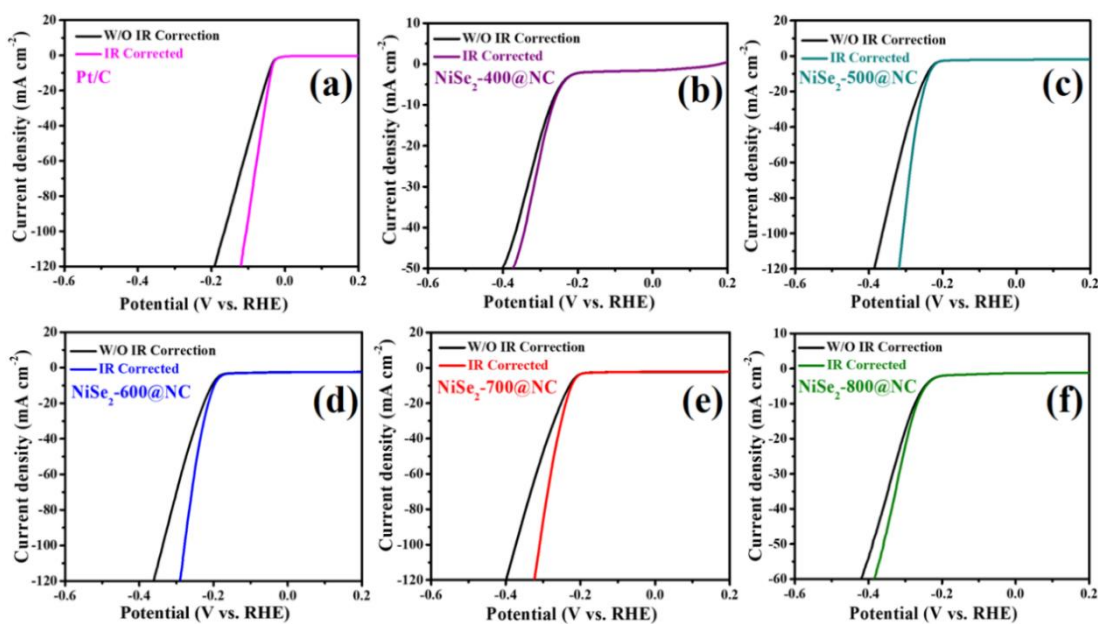


Figure 5.9: LSV plots representing before and after *iR* compensation (a-f).

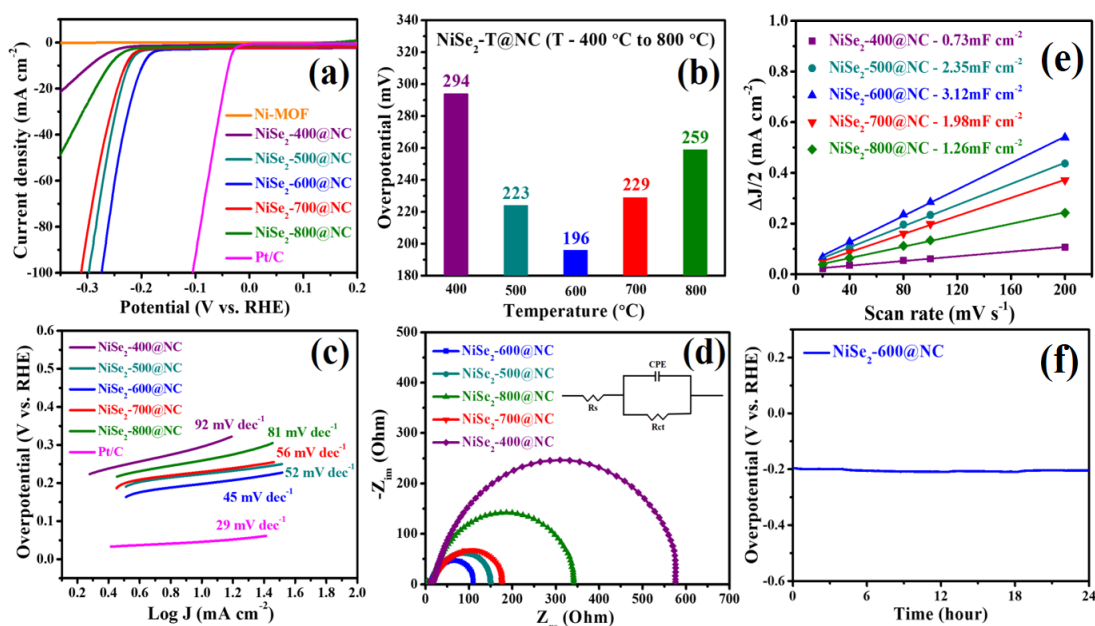


Figure 5.10: LSVs of Pt/C, Ni-MOF and NiSe₂-T@NCs (a), overpotential comparison of NiSe₂-T@NCs (b), corresponding Tafel slopes (c), EIS (d), C_{dl} of NiSe₂-T@NCs (e), stability plot of NiSe₂-600@NC (f).

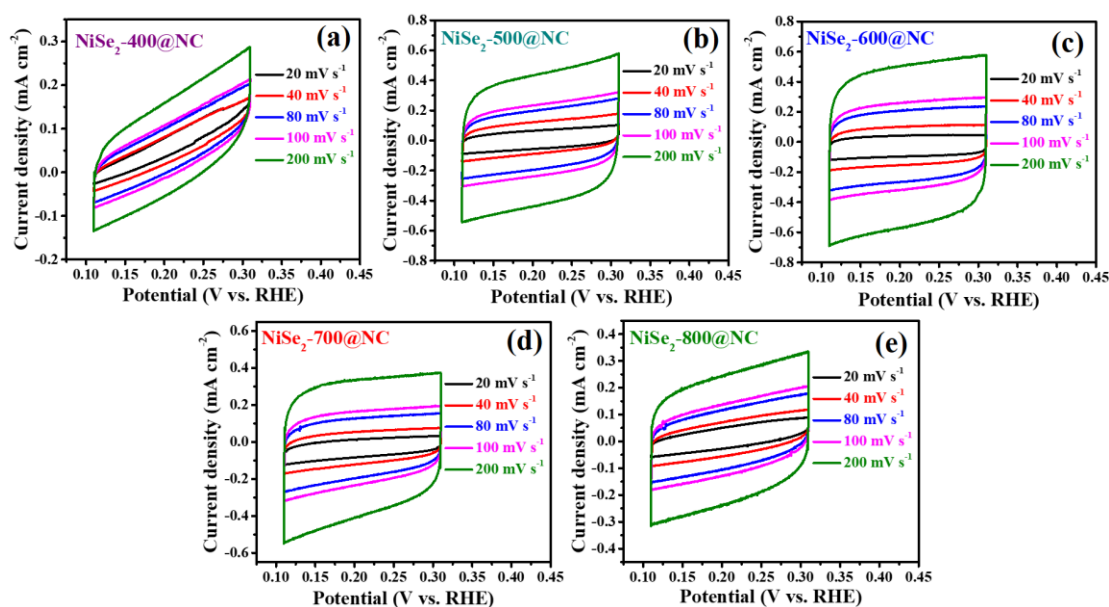


Figure 5.11: CV curves of NiSe₂-400@NC (a), NiSe₂-500@NC (b), NiSe₂-600@NC (c), NiSe₂-700@NC (d), NiSe₂-800@NC (e) in the potential window of 0.11 V vs. RHE to 0.31 V vs. RHE at different scan rates (20 mV s⁻¹ to 200 mV s⁻¹).

Figure 5.10a shows the LSV plot of NiSe₂-600@NC with better HER activity than Ni-MOF, NiSe₂-400@NC, NiSe₂-500@NC, NiSe₂-700@NC, and NiSe₂-800@NC. It has been observed that the Ni-MOF precursor is inactive toward HER and shows negligible cathodic current density. However, NiSe₂-600@NC required an overpotential of 196 mV (vs. RHE) to reach the predefined current density of 10 mA cm⁻², which is much less as compared to other annealed NiSe₂-T@NCs (T = 400, 500, 700, and 800 °C) products and some of the recently reported HER electrocatalysts (**Table 5.1**). The variation in overpotential values of the electrocatalysts with different annealing temperatures is shown in **Figure 5.10b**. The insights into surface kinetics and the rate-determining step of the as-prepared HER electrocatalyst are verified by Tafel slope (plotted via overpotential vs log J). The obtained Tafel slope of 45 mV dec⁻¹ for NiSe₂-600@NC is lower than the other annealed products such as NiSe₂-400@NC (92 mV dec⁻¹), NiSe₂-500@NC (52 mV dec⁻¹), NiSe₂-700@NC (56 mV dec⁻¹), and NiSe₂-

800@NC (81 mV dec⁻¹), respectively. It has been observed that the lower Tafel slope value of NiSe₂-600@NC (45 mV dec⁻¹) follows the Volmer-Heyrovsky reaction path with faster HER kinetics,^{5,9} corresponding to good HER behavior than other annealed products. Besides these, the noble Pt/C shows a lower Tafel value (29 mV dec⁻¹) and is used as the standard electrocatalyst compared to as-prepared noble metal-free HER electrocatalysts,⁵ shown in **Figure 5.10c**. The above Tafel results indicate that the NiSe₂-600@NC has better electrocatalytic activity in an acidic medium among all NiSe₂-T@NCs. Electrochemical impedance spectroscopy (EIS) or Nyquist plot reveals the charge transfer process and catalytic response between the electrolyte and electrode surface interface.⁶³ **Figure 5.10d** shows the Nyquist plots of the different NiSe₂-T@NC products. The smaller diameter of obtained semicircle in the EIS diagram corresponds to the lower value of charge transfer resistance (R_{CT}), leading to a faster electron transfer process.¹⁰ NiSe₂-600@NC has a solution resistance (R_S) of 9 Ω and a charge transfer resistance (R_{CT}) of 100 Ω , which is lower than the other annealed products such as NiSe₂-500@NC (141 Ω), NiSe₂-700@NC (166 Ω), NiSe₂-800@NC (332 Ω), and NiSe₂-400@NC (567 Ω), respectively. The smaller R_{CT} value obtained from the EIS data represents the good electrochemical responses and faster electron transfer of NiSe₂-600@NC, reflecting its better HER performance in the acidic medium. The inset in **Figure 5.10d** is the fitted equivalent circuit diagram as obtained from EIS data.

The cyclic voltammetry (CV) technique with different scan rates (20, 40, 80, 100, and 200 mV s⁻¹) in a non-Faradaic potential window (0.11 V vs. RHE to 0.31 V vs. RHE) was used to estimate the double-layer capacitance (C_{dl}) (**Figure 5.11**). The electrochemical active surface area (ECSA) has a linear relationship with the double layer capacitance (C_{dl}) and is used to calculate the number of electrochemical active sites.^{3,9} The C_{dl} value was measured by plotting the graph between different scan rates

versus the obtained current density. **Figure 5.10e** displays the C_{dl} values of the NiSe₂-T@NC products and were calculated from half of the difference of anodic and cathodic current density ($\Delta J = J_a - J_c$) at 0.21 V (vs. RHE). The C_{dl} values correspond to the linear slopes of the plotted data. The obtained C_{dl} value of NiSe₂-600@NC was found to be 3.12 mF cm⁻², which is a C_{dl} higher value than that of the other annealed NiSe₂-T@NCs. The higher C_{dl} value of NiSe₂-600@ NC results in better electrochemical accessible surface area (ECSA), which contributes toward better HER performance.^{43,59} Furthermore, the long-term stability test has been used to investigate the material's practical applicability in an acidic medium. **Figure 5.10f** represents the chronopotentiometry (CP) analysis (at a constant current density of 10 mA cm⁻²) of NiSe₂-600@NC. Interestingly, the electrocatalyst shows significantly stable potential even after 24 h of continuous electrolysis under an acidic environment. The robustness of the electrocatalyst after 24 h of stability test was also verified through the preliminary characterization technique of PXRD and FESEM. **Figure 5.12a** shows the powder X-ray diffraction pattern of the electrocatalyst after the long-term electrolysis process, which signifies no such change in the phase purity of the NiSe₂-600@NC sample. Like post stability PXRD, the post stability FESEM analysis also verified the changes of morphological structures as shown in **Figure 5.12b**. It has been observed that 24 h of continuous electrolysis process affects some portion of the morphological structures with little distortion in the acidic condition.

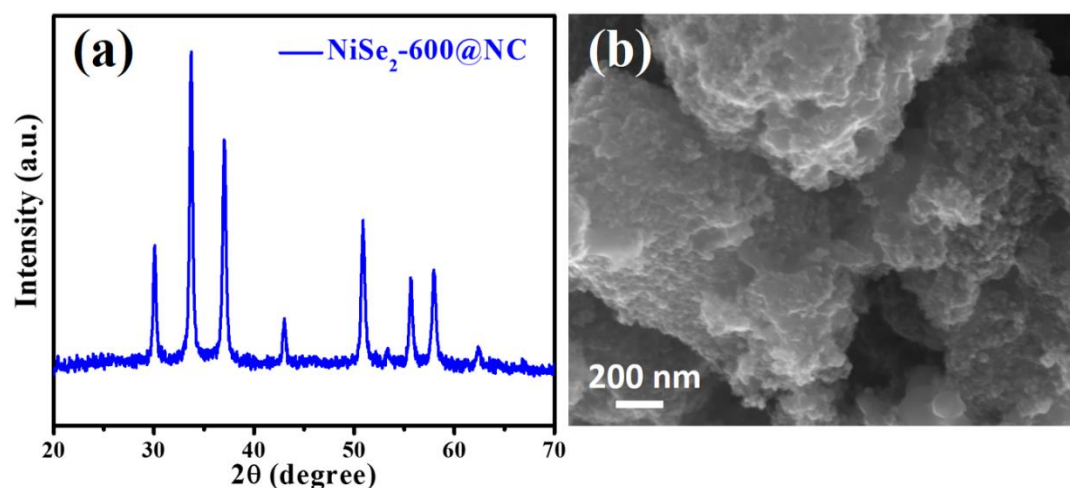


Figure 5.12: PXRD (a) and FESEM (b) of NiSe₂-600@NC after the stability test.

On the basis of the above systematic characterization results and the electrochemical performances, the enhanced HER activity of NiSe₂-600@NC can be attributed to its unique spherical-type surface morphology organized by the embedment of NC matrix, which not only increases the conductivity and electrochemical active surface area to accelerate the catalytic activity but also provides robustness to the structure which reflects in its long-term durability test. Second, the NC matrix might also modulate the electronic structural environment of the NiSe₂-600@NC sample toward improved HER performance.

Table 5.1 HER activity comparison of NiSe₂-600@NC with previously reported literature.

Electrocatalyst used	Overpotential at 10 mA cm ⁻² (mV)	Tafel slope (mV dec ⁻¹)	Electrolyte	References
NiSe ₂ @NG-140	201	36.1	0.5 M H ₂ SO ₄	ACS Sustainable Chem. Eng. 2019, 7, 4351–4359
NiSe ₂ nanosheets	156	54	0.5 M H ₂ SO ₄	Nanoscale 2017, 9, 5538-5544
NiSe ₂ NCs	190	44	0.5 M H ₂ SO ₄	ACS Appl. Mater. Interfaces 2016, 8, 5327-5334
MoSe ₂ -NiSe	210	56	0.5 M H ₂ SO ₄	Chem. Mater. 2016, 28, 1838-1846
MoSe ₂ /NiSe ₂ NWs	193	46.9	0.5 M H ₂ SO ₄	J. Mater. Chem. A 2017, 5, 19752- 19759
NiSe nanofibers	270	64	0.5 M H ₂ SO ₄	J. Mater. Chem., 2012, 22, 13662-13668
CoSe ₂ /C nanocrystals	260	45.7	0.5 M H ₂ SO ₄	Int. J. Hydrogen Energy 2019, 44, 22787-22795
MoSe ₂ -CoSe ₂ nanotubes	206	45	0.5 M H ₂ SO ₄	J. Mater. Chem. A, 2018, 6, 7842–7850
Ni _{0.5} Mo _{0.5} Se	197	107	0.5 M H ₂ SO ₄	Int. J. Hydrogen Energy 2019, 44, 22796-22805
NiSe₂-600@NC	196	45	0.5 M H₂SO₄	This Work

5.7 Conclusions

In summary, we started with the facile solvothermal synthesis of a 1D Ni-MOF [Ni(BPY)(DDE)] [(BPY = 2,2'-bipyridyl), (DDE = 4,4'-dicarboxy diphenyl ether)] followed by subsequent annealing with varied temperature and in situ selenylation strategies have successfully fabricated NiSe₂ nanoparticles encapsulated in an NC matrix (NiSe₂-T@NC, T = 400–800 °C). The tuning of the annealing temperature of Ni-MOF precursor and the selenylation approach to the formation of NiSe₂-T@NCs plays a crucial role in optimizing the electrochemical activity toward hydrogen evolution. In comparison to other NiSe₂-T@NCs annealed products, NiSe₂-600@NC shows a better porous structure with spherical morphology and excellent electrocatalytic performance in terms of lower value of overpotential (196 mV) to reach a predefined current density of 10 mA cm⁻², with a small Tafel slope (45 mV dec⁻¹) and robust stability under acidic condition. Besides these, the high specific surface area (57.95 m² g⁻¹) of NiSe₂-600@NC corresponds to a higher electrochemical active surface area (ECSA) which makes it the frontline electrocatalyst among all the synthesized products of NiSe₂-T@NCs. Furthermore, the electrocatalyst's post stability characterization analysis (PXRD, FESEM) showed its practical applicability in an acidic medium. Consequently, the facile cost-effective synthesis strategy and the synergistic effect of the NC layers with NiSe₂ nanoparticles, corresponding to unique spherical-type morphology, higher ECSA value, showed excellent HER activity and robust durability that makes the NiSe₂-600@NC as an alternative electrocatalyst compared to noble metal-based electrocatalyst for water splitting reaction.

5.8 References

- 1 K. T. Møller, T. R. Jensen, E. Akiba and H. Li, *Prog. Nat. Sci. Mater. Int.*, 2017, **27**, 34–40.
- 2 X. Zou and Y. Zhang, *Chem. Soc. Rev.*, 2015, **44**, 5148–5180.
- 3 Z. Huang, J. Liu, Z. Xiao, H. Fu, W. Fan, B. Xu, B. Dong, D. Liu, F. Dai and D. Sun, *Nanoscale*, 2018, **10**, 22758–22765.
- 4 F. Alcaide, P.-L. Cabot and E. Brillas, *J. Power Sources*, 2006, **153**, 47–60.
- 5 J. K. Das, A. K. Samantara, A. K. Nayak, D. Pradhan and J. N. Behera, *Dalt. Trans.*, 2018, **47**, 13792–13799.
- 6 J. Wang, X. Yue, Y. Yang, S. Sirisomboonchai, P. Wang, X. Ma, A. Abudula and G. Guan, *J. Alloys Compd.*, 2020, **819**, 153346.
- 7 X. Li, X. Hao, A. Abudula and G. Guan, *J. Mater. Chem. A*, 2016, **4**, 11973–12000.
- 8 M. Zeng and Y. Li, *J. Mater. Chem. A*, 2015, **3**, 14942–14962.
- 9 N. Sahu, J. K. Das and J. N. Behera, *Sustain. Energy Fuels*, 2021, **5**, 4992–5000.
- 10 A. K. Samantara, J. K. Das, S. Ratha, N. K. Jena, B. Chakraborty and J. N. Behera, *ACS Appl. Mater. Interfaces*, 2021, **13**, 35828–35836.
- 11 X. Liu, Y. Liu and L. Z. Fan, *J. Mater. Chem. A*, 2017, **5**, 15310–15314.
- 12 S. Anantharaj, S. R. Ede, K. Sakthikumar, K. Karthick, S. Mishra and S. Kundu, *ACS Catal.*, 2016, **6**, 8069–8097.
- 13 N. Cheng, S. Stambula, D. Wang, M. N. Banis, J. Liu, A. Riese, B. Xiao, R. Li,

- T.-K. Sham, L.-M. Liu, G. A. Botton and X. Sun, *Nat. Commun.*, 2016, **7**, 13638.
- 14 J. Mohammed-Ibrahim and X. Sun, *J. Energy Chem.*, 2019, **34**, 111–160.
- 15 X. Wang, Y. Orikasa and Y. Uchimoto, *ACS Catal.*, 2016, **6**, 4195–4198.
- 16 L. Tian, X. Yan and X. Chen, *ACS Catal.*, 2016, **6**, 5441–5448.
- 17 Y. Li, H. Wang, L. Xie, Y. Liang, G. Hong and H. Dai, *J. Am. Chem. Soc.*, 2011, **133**, 7296–7299.
- 18 J. Jian, L. Yuan, H. Qi, X. Sun, L. Zhang, H. Li, H. Yuan and S. Feng, *ACS Appl. Mater. Interfaces*, 2018, **10**, 40568–40576.
- 19 Z. Wu, B. Fang, A. Bonakdarpour, A. Sun, D. P. Wilkinson and D. Wang, *Appl. Catal. B Environ.*, 2012, **125**, 59–66.
- 20 I. H. Kwak, H. S. Im, D. M. Jang, Y. W. Kim, K. Park, Y. R. Lim, E. H. Cha and J. Park, *ACS Appl. Mater. Interfaces*, 2016, **8**, 5327–5334.
- 21 Y. Huang, H. Lu, H. Gu, J. Fu, S. Mo, C. Wei, Y.-E. Miao and T. Liu, *Nanoscale*, 2015, **7**, 18595–18602.
- 22 L. Zhang, Q. Fan, K. Li, S. Zhang and X. Ma, *Sustain. Energy Fuels*, 2020, **4**, 5417–5432.
- 23 V. D. Silva, T. A. Simões, J. P. F. Grilo, E. S. Medeiros and D. A. Macedo, *J. Mater. Sci.*, 2020, **55**, 6648–6659.
- 24 J. Yang, G. Zhu, Y. Liu, J. Xia, Z. Ji, X. Shen and S. Wu, *Adv. Funct. Mater.*, 2016, **26**, 4712–4721.
- 25 Y. Wang, T. Zhou, K. Jiang, P. Da, Z. Peng, J. Tang, B. Kong, W.-B. Cai, Z. Yang and G. Zheng, *Adv. Energy Mater.*, 2014, **4**, 1400696.

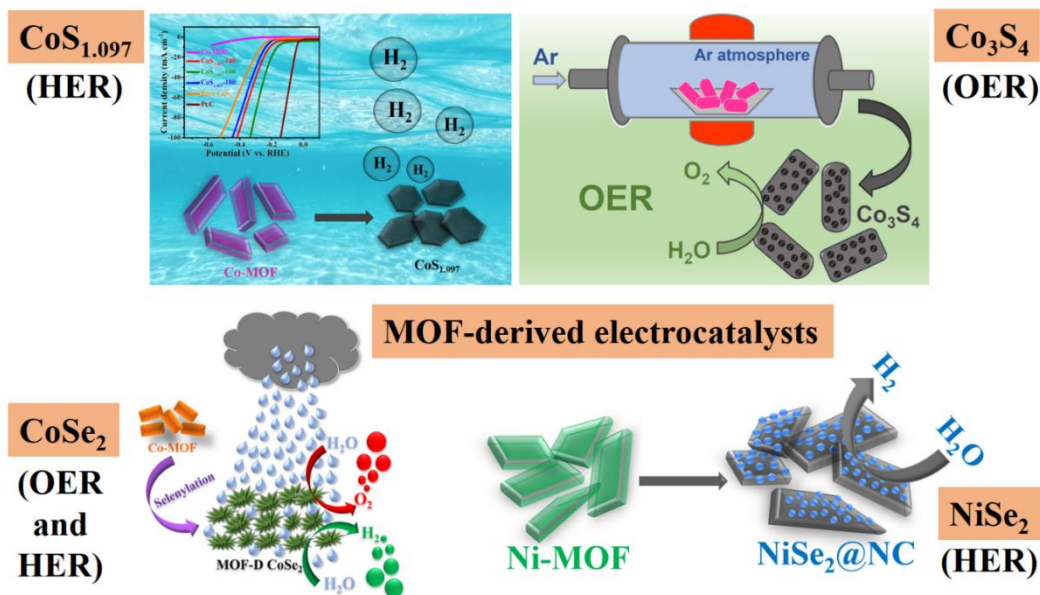
- 26 J. K. Das, A. K. Samantara, S. Satyarthi, C. S. Rout and J. N. Behera, *RSC Adv.*, 2020, **10**, 4650–4656.
- 27 M. Pi, T. Wu, D. Zhang, S. Chen and S. Wang, *Nanoscale*, 2016, **8**, 19779–19786.
- 28 C. Du, L. Yang, F. Yang, G. Cheng and W. Luo, *ACS Catal.*, 2017, **7**, 4131–4137.
- 29 P. Jiang, Q. Liu and X. Sun, *Nanoscale*, 2014, **6**, 13440–13445.
- 30 J. Masud, S. Umapathi, N. Ashokaan and M. Nath, *J. Mater. Chem. A*, 2016, **4**, 9750–9754.
- 31 J. Theerthagiri, G. Durai, K. Karuppasamy, P. Arunachalam, V. Elakkiya, P. Kuppusami, T. Maiyalagan and H.-S. Kim, *J. Ind. Eng. Chem.*, 2018, **67**, 12–27.
- 32 A. T. Garcia-Esparza, D. Cha, Y. Ou, J. Kubota, K. Domen and K. Takanebe, *ChemSusChem*, 2013, **6**, 168–181.
- 33 X. Peng, C. Pi, X. Zhang, S. Li, K. Huo and P. K. Chu, *Sustain. Energy Fuels*, 2019, **3**, 366–381.
- 34 N. Han, P. Liu, J. Jiang, L. Ai, Z. Shao and S. Liu, *J. Mater. Chem. A*, 2018, **6**, 19912–19933.
- 35 C. C. L. McCrory, S. Jung, J. C. Peters and T. F. Jaramillo, *J. Am. Chem. Soc.*, 2013, **135**, 16977–16987.
- 36 N. Dubouis and A. Grimaud, *Chem. Sci.*, 2019, **10**, 9165–9181.
- 37 Z. Huang, S. Yuan, T. Zhang, B. Cai, B. Xu, X. Lu, L. Fan, F. Dai and D. Sun, *Appl. Catal. B Environ.*, 2020, **272**, 118976.

- 38 X. Rui, H. Tan and Q. Yan, *Nanoscale*, 2014, **6**, 9889–9924.
- 39 J. Liu, D. Zhu, C. Guo, A. Vasileff and S. Qiao, *Adv. Energy Mater.*, 2017, **7**, 1700518.
- 40 T. Chen, S. Li, J. Wen, P. Gui and G. Fang, *ACS Appl. Mater. Interfaces*, 2017, **9**, 35927–35935.
- 41 T. Y. Ma, S. Dai, M. Jaroniec and S. Z. Qiao, *J. Am. Chem. Soc.*, 2014, **136**, 13925–13931.
- 42 Y.-W. Li, Q. Wu, R.-C. Ma, X.-Q. Sun, D.-D. Li, H.-M. Du, H.-Y. Ma, D.-C. Li, S.-N. Wang and J.-M. Dou, *RSC Adv.*, 2021, **11**, 5947–5957.
- 43 A. Zhao, G. Xu, Y. Li, J. Jiang, C. Wang, X. Zhang, S. Zhang and L. Zhang, *Inorg. Chem.*, 2020, **59**, 12778–12787.
- 44 G. R. Bhadu, B. Parmar, P. Patel, A. Paul, J. C. Chaudhari, D. N. Srivastava and E. Suresh, *Appl. Surf. Sci.*, 2020, **529**, 147081.
- 45 M. K. Sahoo, A. K. Samantara and J. N. Behera, *Inorg. Chem.*, 2022, **61**, 62–72.
- 46 T. Qiu, Z. Liang, W. Guo, H. Tabassum, S. Gao and R. Zou, *ACS Energy Lett.*, 2020, **5**, 520–532.
- 47 T. Wang, Q. Zhou, X. Wang, J. Zheng and X. Li, *J. Mater. Chem. A*, 2015, **3**, 16435–16439.
- 48 W. Li, B. Yu, Y. Hu, X. Wang, D. Yang and Y. Chen, *ACS Sustain. Chem. Eng.*, 2019, **7**, 4351–4359.
- 49 M.-R. Gao, X. Cao, Q. Gao, Y.-F. Xu, Y.-R. Zheng, J. Jiang and S.-H. Yu, *ACS Nano*, 2014, **8**, 3970–3978.

- 50 B. Wang, X. Wang, B. Zheng, B. Yu, F. Qi, W. Zhang, Y. Li and Y. Chen, *Electrochem. commun.*, 2017, **83**, 51–55.
- 51 L. Zhang, T. Wang, L. Sun, Y. Sun, T. Hu, K. Xu and F. Ma, *J. Mater. Chem. A*, 2017, **5**, 19752–19759.
- 52 X. Zhou, Y. Liu, H. Ju, B. Pan, J. Zhu, T. Ding, C. Wang and Q. Yang, *Chem. Mater.*, 2016, **28**, 1838–1846.
- 53 Z. Huang, B. Xu, Z. Li, J. Ren, H. Mei, Z. Liu, D. Xie, H. Zhang, F. Dai, R. Wang and D. Sun, *Small*, 2020, **16**, 2004231.
- 54 H.-P. Xiao, Y.-Q. Cheng and X.-H. Li, *Acta Crystallogr. Sect. E Struct. Reports Online*, 2005, **61**, m469–m470.
- 55 J. Lin, J. He, Y. Chen, Q. Li, B. Yu, C. Xu and W. Zhang, *Electrochim. Acta*, 2016, **215**, 667–673.
- 56 B. Wang, Z. Wang, X. Wang, B. Zheng, W. Zhang and Y. Chen, *J. Mater. Chem. A*, 2018, **6**, 12701–12707.
- 57 J. Yang, Z. Sun, J. Wang, J. Zhang, Y. Qin, J. You and L. Xu, *CrystEngComm*, 2019, **21**, 994–1000.
- 58 A. P. Grosvenor, M. C. Biesinger, R. S. C. Smart and N. S. McIntyre, *Surf. Sci.*, 2006, **600**, 1771–1779.
- 59 J. Liang, Y. Yang, J. Zhang, J. Wu, P. Dong, J. Yuan, G. Zhang and J. Lou, *Nanoscale*, 2015, **7**, 14813–14816.
- 60 Y. Xu, W. Tu, B. Zhang, S. Yin, Y. Huang, M. Kraft and R. Xu, *Adv. Mater.*, 2017, **29**, 1–8.

- 61 X. Wu, Y. Niu, B. Feng, Y. Yu, X. Huang, C. Zhong, W. Hu and C. M. Li, *ACS Appl. Mater. Interfaces*, 2018, **10**, 20440–20447.
- 62 W. Hou, B. Zheng, F. Qi, J. He, W. Zhang and Y. Chen, *Electrochim. Acta*, 2018, **283**, 1146–1153.
- 63 K. Ao, J. Dong, C. Fan, D. Wang, Y. Cai, D. Li, F. Huang and Q. Wei, *ACS Sustain. Chem. Eng.*, 2018, **6**, 10952–10959.

SUMMARY AND FUTURE SCOPE



To summarize, the thesis entitled “MOF-derived metal chalcogenide nanostructured materials as electrocatalysts for water splitting in electrochemical energy conversion” emphasizes the noteworthy possibilities of metal chalcogenides in promoting energy conversion methods. The thesis shows that these materials have exceptional electrochemical properties toward hydrogen and oxygen evolution reactions, including lower overpotential values, faster kinetics, good conductivity, and longer durability under demanding electrolytic conditions. These properties are demonstrated through thorough investigation and analysis.

The findings show that MOF-derived metal chalcogenide materials have a number of benefits, including high abundance, low cost, and a variety of morphologies, which makes them desirable options for materials used in next-generation energy conversion

electrodes. Their exceptional performance in electrochemical reactions involving the evolution of oxygen and hydrogen opens the door for the development of effective and long-lasting energy conversion technologies, which will help meet the growing need for renewable energy sources. The study also emphasizes how crucial temperature and reaction time variation are to achieve the best catalytic performance possible for the products derived from MOFs.

Taking everything into account, this thesis offers insightful information on the topic of electrochemical energy conversion utilizing a variety of electroactive materials, laying a strong foundation for future successes in the development and utilization of cutting-edge energy technology. The research's conclusions have the power to completely alter the energy sector and lead the way for a more sustainable, effective, and clean future.